

MAGNETOHYDRODYNAMIC TURBULENCE AND
ANGULAR MOMENTUM TRANSPORT IN ACCRETION DISKS

by

Martín Elías Pessah

A Dissertation Submitted to the Faculty of the
DEPARTMENT OF ASTRONOMY
In Partial Fulfillment of the Requirements
For the Degree of
DOCTOR OF PHILOSOPHY
In the Graduate College
THE UNIVERSITY OF ARIZONA

2007

THE UNIVERSITY OF ARIZONA
GRADUATE COLLEGE

As members of the Dissertation Committee, we certify that we have read the dissertation prepared by Martín Elías Pessah entitled “Magnetohydrodynamic Turbulence and Angular Momentum Transport in Accretion Disks” and recommend that it be accepted as fulfilling the dissertation requirement for the Degree of Doctor of Philosophy.

_____ Date: April 3rd, 2007
Dimitrios Psaltis

_____ Date: April 3rd, 2007
Romeel Davé

_____ Date: April 3rd, 2007
Daniel Eisenstein

_____ Date: April 3rd, 2007
Xiaohui Fan

_____ Date: April 3rd, 2007
Drew Milsom

Final approval and acceptance of this dissertation is contingent upon the candidate's submission of the final copies of the dissertation to the Graduate College.

I hereby certify that I have read this dissertation prepared under my direction and recommend that it be accepted as fulfilling the dissertation requirement.

_____ Date: April 3rd, 2007
Dissertation Director: Dimitrios Psaltis

STATEMENT BY AUTHOR

This dissertation has been submitted in partial fulfillment of requirements for an advanced degree at The University of Arizona and is deposited in the University Library to be made available to borrowers under rules of the Library.

Brief quotations from this dissertation are allowable without special permission, provided that accurate acknowledgment of source is made. Requests for permission for extended quotation from or reproduction of this manuscript in whole or in part may be granted by the head of the major department or the Dean of the Graduate College when in his or her judgment the proposed use of the material is in the interests of scholarship. In all other instances, however, permission must be obtained from the author.

SIGNED: Martín Elías Pessah

ACKNOWLEDGMENTS

During my incursion in MHD turbulence and accretion disk theory, I have benefited from fruitful discussions with several people. I thank Eric Blackman for sharing with us his ideas and points of view on different aspects of dynamo theory and stress modeling. I am grateful to Gordon Ogilvie for interesting discussions and for his detailed comments and constructive criticism on early versions of the last two chapters of this study. I thank Jim Stone for useful discussions and for helping us with the necessary modifications to the ZEUS code that was used in the last chapter of this work. I am also grateful to Omer Blaes, Andrew Cumming, Wolfgang Duschl, Charles Gammie, Peter Goldreich, Fred Lamb, Eliot Quataert, and Ethan Vishniac, for useful discussions during the last few years.

I thank the Faculty of the Astronomy Department, specially to those who have left an impression on me. To Adam Burrows, for putting the physics in his Theoretical Astrophysics course. If I ever teach a course, I will be lucky if I have half of his enthusiasm. To Daniel Eisenstein, whose door was always open. I will always wonder how it would have been to become a cosmologist under his advice. To Rob Kennicutt, who told me a lot with only a few words. To George Rieke, for not giving up in trying to make a theorist understand how an instrument works.

I am indebted to my advisor, Dimitrios Psaltis, for encouraging me to address important questions, for being open, and for always allowing me to choose. He provided me with the support that helped me to feel confident and the freedom that taught me to be responsible. I take with me his greatest advice: “*To get more done you have to work less*”. I have not figured out how this is supposed to work . . .

I have the privilege of shearing the office, for *many* hours, with Chi-kwan Chan, my friend and collaborator. A lot of the work in this dissertation would not have been the same without him and the many week-long discussions we had. I am sure we hold the pair-staring-at-a-white-board-full-of-equations record (someone should keep track of these things!). I wish I had learned more from him.

Thanks to Erin Carlson, Michelle Cournoyer, Catalina Diaz-Silva, Joy Facio, Chris Impey, Ann Zabludoff, and Peter Strittmatter for making my life as a graduate student *much* easier. I also thank the people in charge of computer support; to Mike Eklund, Jeff Fookson, Phil Goisman, and Neal Lauver, for helping me out even when they had to fix things that I should not have broken.

I thank Andy Marble, John Moustakas, Jeremiah Murphy, Nick Siegler, and Amy Stutz who became my friends in between coffee, courses, exams, IDL, and discussing how we would run things if we were in charge. Our time will come!

I thank Ana, Gaspar, and Luis, who I definitely regret not meeting sooner, for making me feel at home away from home. I thank the people that I have seen so little during the last several years, my family and friends, for making me feel loved in spite of the distance. Finally, and most importantly, I thank Paula, my wife, for her unconditional support and for believing in me more than she should.

DEDICATION

A Paula. Por tu amor, tu paciencia y tu comprensión sin límites ...

TABLE OF CONTENTS

LIST OF FIGURES	8
ABSTRACT	9
CHAPTER 1 INTRODUCTION	11
1.1 Basic Disk Structure	13
1.2 The Angular Momentum Problem	15
1.3 The Standard Accretion Disk Model	16
1.4 The Magnetorotational Instability and MHD Turbulence	18
1.5 This Dissertation in Context	23
CHAPTER 2 THE STABILITY OF MAGNETIZED ROTATING PLASMAS WITH SUPERHERMAL FIELDS	29
2.1 Introduction	30
2.2 MHD Equations for Perturbations and the Dispersion Relation . . .	34
2.2.1 Equations for the Perturbations	35
2.2.2 Dispersion Relation	43
2.2.3 Previous Treatments	45
2.3 Numerical Solutions	50
2.4 The Onset of Instabilities	55
2.4.1 Unstable Modes	55
2.4.2 Analytic Approximations	57
2.5 Discussion	66
2.5.1 Importance of Curvature Terms	66
2.5.2 Magnetorotational Instabilities with Superthermal Fields . .	69
2.5.3 Comparison to Previous Analytical Studies	73
2.5.4 Implications for Shearing Box Simulations	80
2.6 Summary and Conclusions	83
CHAPTER 3 THE SIGNATURE OF THE MAGNETOROTATIONAL INSTABILITY IN THE REYNOLDS AND MAXWELL STRESS TENSORS IN ACCRETION DISKS	85
3.1 Introduction	85
3.2 Assumptions	88
3.3 The Eigenvalue Problem for the MRI: A Formal Solution	91
3.3.1 Eigenvectors	92
3.3.2 Properties of the Eigenvectors	94
3.3.3 Temporal Evolution	97
3.4 Net Angular Momentum Transport by the MRI	98
3.4.1 Definitions and Mean Values of Correlation Functions . . .	98
3.4.2 Properties of the MRI-Driven Stresses	101

TABLE OF CONTENTS — <i>Continued</i>	
3.5	Energetics of MRI-driven Fluctuations 105
3.6	Discussion 106
CHAPTER 4 A MODEL FOR ANGULAR MOMENTUM TRANSPORT IN ACCRE-	
	TION DISKS DRIVEN BY THE MAGNETOROTATIONAL INSTABILITY 112
4.1	Introduction 112
4.2	A Model for MHD Turbulent Pumping by the MRI 114
4.3	A Model for the Saturation of MRI-driven Turbulence 118
4.4	Discussion 122
CHAPTER 5 THE FUNDAMENTAL DIFFERENCE BETWEEN ALPHA-VISCOSITY	
	AND TURBULENT MAGNETOROTATIONAL STRESSES 124
5.1	Introduction 124
5.2	Alpha Viscosity vs. MHD Stresses 126
5.3	Predictions from Stress Modeling 129
5.3.1	Kato & Yoshizawa 1995 130
5.3.2	Ogilvie 2003 133
5.3.3	Pessah, Chan, & Psaltis 2006 137
5.4	Results from Numerical Simulations 140
5.4.1	The Shearing Box Approximation 141
5.4.2	Numerical Set Up 142
5.4.3	Results 143
5.5	Discussion 145
CHAPTER 6 SUMMARY AND OUTLOOK: TOWARDS MAGNETOROTATIONAL	
	ACCRETION DISK MODELS 147
6.1	Summary 147
6.2	Beyond the Standard Accretion Disk Model 150
6.3	A New Era in Accretion Disk Modeling 152
APPENDIX A MRI MODES WITH FINITE k_r/k_z RATIOS 156	
APPENDIX B MRI MODES WITH VANISHING FREQUENCY 159	
REFERENCES 161	

LIST OF FIGURES

1.1	Schematics of the magnetorotational instability (MRI)	21
1.2	Mode structure for the MRI	22
1.3	Timescales and lengthscales in accretion disks	25
2.1	Eigenfrequencies of dispersion relation (2.25) – real parts	51
2.2	Eigenfrequencies of dispersion relation (2.25) – imaginary parts	52
2.3	MRIs with strong toroidal magnetic fields - numerical solutions	56
2.4	Eigenfrequencies of simplified versions of dispersion relation (2.25)	61
2.5	MRIs with strong toroidal magnetic fields - analytical approximation	63
2.6	Importance of curvature terms	67
2.7	MRIs with strong magnetic fields as a function of the local shear	71
2.8	MRIs with strong magnetic fields as a function of the sound speed	72
2.9	Stabilization of the MRI for strong toroidal fields - Growth rates	75
2.10	Stabilization of the MRI for strong toroidal fields - Mode structure	76
2.11	Implications for shearing box simulations with strong toroidal fields	81
3.1	Components of unstable MRI eigenvectors	95
3.2	<i>per-k</i> contributions of the linear MHD stresses and energies	102
3.3	Correlation between Maxwell and Reynolds stresses	109
3.4	Ratio between Maxwell and Reynolds stresses vs. local shear	110
4.1	Model stress-to-magnetic energy correlations in MRI-turbulence	121
4.2	Model energy-density saturator predictor in MRI-turbulence	123
5.1	Fundamental difference between MRI-stresses and alpha-viscosity	134
A.1	Eigenfrequencies of dispersion relation (2.25) for finite ratios k_r/k_z	158

ABSTRACT

It is currently believed that angular momentum transport in accretion disks is mediated by magnetohydrodynamic (MHD) turbulence driven by the magnetorotational instability (MRI). More than 15 years after its discovery, an accretion disk model that incorporates the MRI as the mechanism driving the MHD turbulence is still lacking. This dissertation constitutes the first in a series of steps towards establishing the formalism and methodology needed to move beyond the standard accretion disk model and incorporating the MRI as the mechanism enabling the accretion process. I begin by presenting a local linear stability analysis of a compressible, differentially rotating flow and addressing the evolution of the MRI beyond the weak-field limit when magnetic tension forces due to strong toroidal fields are considered. Then, I derive the first formal analytical proof showing that, during the exponential growth of the instability, the mean total stress produced by correlated MHD fluctuations is positive and leads to a net outward flux of angular momentum. I also show that some characteristics of the MHD stresses that are determined during this initial phase are roughly preserved in the turbulent saturated state observed in local numerical simulations. Motivated by these results, I present the first mean-field MHD model for angular momentum transport driven by the MRI that is able to account for a number of correlations among stresses found in local numerical simulations. I point out the relevance of a new type of correlation that couples the dynamical evolution of the Reynolds and Maxwell stresses and plays a key role in developing and sustaining the MHD turbulence. Finally, I address how the turbulent transport of angular momentum depends on the magnitude of the local shear. I show that turbulent MHD stresses in accretion disks cannot be described in terms of shear-viscosity.

I imagine that right now you are feeling a bit like Alice... Stumbling down the rabbit hole? Hmm? [...] This is your last chance. After this, there is no turning back. You take the blue pill, the story ends, you wake up in your bed and believe whatever you want to believe. You take the red pill, you stay in Wonderland and I show you how deep the rabbit hole goes...

— Morpheus, The Matrix.

CHAPTER 1

INTRODUCTION

A large number of celestial objects exchange mass and angular momentum with their environments by means of accretion disks during crucial evolutionary stages. Understanding the processes that determine the rate at which matter accretes and energy is radiated from these disks is vital for unveiling the mysteries surrounding the formation and evolution of a wide variety of objects in the Universe. The physical roles played by accretion disks, as well as their observable implications, are as diverse as the nature of the astrophysical bodies that they surround:

- Although it is still unknown what exactly determines the initial mass function of protostars for a fixed molecular cloud mass or even the masses of planets around a given star, there is little doubt that the accretion process plays a central role in both cases (Bonnell, Clarke, Bate, & Pringle, 2001). Accretion via protoplanetary disks is also thought to be intimately related to the bipolar molecular outflows and brightness variations observed in newly-born protostars.
- Disk accretion onto white dwarfs is believed to be responsible for the violent behavior observed in cataclysmic variable systems, including novae, dwarf-novae, recurrent novae, and novae-like variables (Wheeler, 1993; Warner, 1995). The presence of accretion disks in these systems is supported by the observed blue continua, double-peaked emission lines, and even the brightness distribution of the disk in some cases (Horne, 1985; Marsh & Horne, 1988).
- The interaction of the accretion flow with the proto-neutron star resulting from a core-collapse supernovae might not only determine the final mass of the neutron star but also its initial spin (Thompson, Quataert, & Burrows, 2005).

- It is currently believed that an important fraction of the plethora of variability phenomena observed from the ultra-violet to X-rays in binary systems containing white dwarfs, neutron stars, and stellar mass black holes originates in the inner regions of the accretion flow (Mauche, 2002; van der Klis, 2005).

- The torques exerted by the accretion disk on old neutron stars in binary systems seems to be responsible for their spin up, bringing them to life again in the form of millisecond pulsars (Bhattacharya & van den Heuvel, 1991).

- Accretion disks seem to play a crucial role for the successful launch of relativistic jets giving rise to the associated gamma-ray burst in collapsar models of black-hole formation (MacFadyen, Woosley, & Heger, 2001). Although the details are yet to be understood, there is a growing consensus on the fundamental connection between disk inflows and jet outflows in a variety of accretion scenarios.

- Disk accretion onto supermassive black holes is the most likely mechanism accounting for the various phenomena observed in Active Galactic Nuclei across the electromagnetic spectrum (Rees, 1984). The characteristic UV spectral feature known as the big blue bump is usually interpreted as the spectra of an optically thick disk. Further spectroscopic evidence of disks is offered by asymmetric double-peaked hydrogen (Chen, Halpern, & Filippenko, 1989; Eracleous, & Halpern, 1994) and iron line profiles (Tanaka et al., 1995). In the last decade, HST resolved several gaseous disks in AGN (e.g., M87, NGC4261, NGC4258) providing a kinematic mean to estimate the masses of the central engines (see, e.g., Ford et al. 1994; Jaffe et al. 1993; Miyoshi et al. 1995).

Because of their ubiquity, and their fundamental roles in a broad range of astrophysical phenomena, accretion disks have been a main focus of attention in theoretical astrophysics for decades. Despite significant efforts, however, some of the most basic questions on accretion disk physics still await definitive answers.

1.1 Basic Disk Structure

Under a set of simplifying, but a priori reasonable, assumptions we can derive a set of equations to describe the basic structure of an accretion disk around a gravitating body (see, e.g., Shakura & Sunyaev, 1973; Kato, Fukue, & Mineshige, 1998; Frank, King, & Raine, 2002). If we assume that

- The gravitational field is determined by the central object,
- The disk is axisymmetric,
- The disk is geometrically thin and optically thick,
- Hydrostatic balance holds in the vertical direction,
- There are no disk winds or external torques,

then the basic equations for the disk structure are:

Continuity equation

$$\frac{\partial \Sigma}{\partial t} + \frac{1}{r} \frac{\partial}{\partial r} (r \Sigma \bar{v}_r) = 0, \quad (1.1)$$

where Σ is the vertically integrated gas density and \bar{v}_r is the mean radial flow velocity. The radial integration of this equation, with the appropriate boundary value, leads to the expression for the accretion rate $\dot{M} = -2\pi r \bar{v}_r \Sigma$.

Momentum conservation in the radial direction

$$\frac{\partial \bar{v}_r}{\partial t} + \bar{v}_r \frac{\partial \bar{v}_r}{\partial r} - \frac{\bar{l}^2}{r^3} = -\frac{GM}{r^2} - \frac{1}{\Sigma} \frac{\partial P}{\partial r}, \quad (1.2)$$

where $\bar{l} = r \Sigma \bar{v}_\phi$ stands for the vertically integrated angular momentum density, M is the mass of the central object, and P is the vertically integrated gas pressure.

Angular momentum conservation

$$\frac{\partial \bar{l}}{\partial t} + \frac{1}{r} \frac{\partial}{\partial r} (r \bar{l} \bar{v}_r) = -\frac{1}{r} \frac{\partial}{\partial r} (r^2 \bar{T}_{r\phi}), \quad (1.3)$$

where $\bar{T}_{r\phi}$ represents the stress acting on a fluid element, i.e., the flux density of ϕ -momentum in the radial direction.

Hydrostatic balance in the vertical direction

$$H = \frac{c_s}{\Omega_K}, \quad (1.4)$$

where H is the disk scaleheight, c_s stands for the sound speed, $c_s \equiv \sqrt{k_B T_c / \mu m_H}$, with k_B the Boltzmann constant, T_c the midplane temperature, μ the mean molecular weight, m_H the mass of the hydrogen atom, and Ω_K stands for the Keplerian angular frequency $\Omega_K \equiv \sqrt{GM/r^3}$.

Equation of state

$$P = c_s^2 \Sigma + 2H \frac{a}{3} T_c^4, \quad (1.5)$$

where a is the radiation constant, $a = 4\sigma/c$, with σ the Stefan-Boltzmann constant and c is the speed of light in vacuum.

Energy balance

$$2\sigma T_{\text{eff}}^4 = \left(-\frac{\partial \ln \Omega}{\partial \ln r} \right) \Omega \bar{T}_{r\phi}, \quad (1.6)$$

where it is assumed that (locally) the rate at which the gas is viscously heated equals the rate at which energy is radiated from the disk (i.e., $Q_{\text{vis}}^+ = Q_{\text{rad}}^-$). Here, the effective temperature is related to the disk midplane temperature by $T_{\text{eff}}^4 = T_c^4 / 3\tau$ and the optical depth, $\tau = \bar{\kappa} \Sigma / 2$, depends on the opacity law, $\bar{\kappa} = \bar{\kappa}(\Sigma, T_c)$.

In order for a parcel of gas to spiral down towards smaller radii, ultimately converting its gravitational potential energy into the emitted radiation, it must lose part of its angular momentum. If we know the rate at which angular momentum is lost from the disk, i.e., if we understand how the stress $\bar{T}_{r\phi}$ depends on the other variables in this set of equations, then for a given mass M and accretion rate \dot{M} , these equations provide $\Sigma, \bar{v}_r, \bar{l}$ (equivalently \bar{v}_ϕ or Ω), $P, H, c_s, T_{\text{eff}}, T_c, \tau, \bar{\kappa}$, as a function of radius.

In summary, under our current set of assumptions, a model for the stress, $\bar{T}_{r\phi}$, leads to a model for the entire structure of the accretion disk. The main unsolved problem in accretion disk physics is the precise nature of the mechanism that allows angular momentum to be removed from the disk, i.e., an *ab initio* theory to calculate the stress $\bar{T}_{r\phi}$.

1.2 The Angular Momentum Problem

Given that a disk of gas orbiting in a central potential is expected to exhibit differential rotation, one might first attempt to model the stress between adjacent disk annuli as a viscous shear stress. To lowest order, it is natural to assume that the local stresses between adjacent disk annuli are proportional to the local rate of strain,

$$\bar{T}_{r\phi} = -r\Sigma\nu_{\text{mol}}\frac{d\Omega}{dr}, \quad (1.7)$$

where $\nu_{\text{mol}} = \lambda_{\text{mol}}c_s$ stands for the coefficient of molecular viscosity. Here (Padmanabhan, 2001)

$$\lambda_{\text{mol}} \sim 6.4 \times 10^4 \left(\frac{T^2}{n} \right) \text{cm}, \quad (1.8)$$

and

$$c_s \sim 10^4 T^{1/2} \text{cm s}^{-1}, \quad (1.9)$$

stand for the mean free path for the particles, with number density n and temperature T , in the laminar disk and the sound speed (both in cgs units), respectively. However, since the early days of accretion disk theory, it has been recognized that molecular viscosity is too small to account for a number of observational properties of accreting objects. For example, if microscopic gas viscosity were the only physical process enabling angular momentum transport in an accretion

disks surrounding a cataclysmic variable, the timescales characterizing a global disk event would be of the order of

$$t_{\text{mol}} \sim \frac{R^2}{\nu_{\text{mol}}} \sim 10^{20} (6.4 \times 10^{-8} n T^{-5/2}) \text{ s} \sim 10^6 \text{ yr}, \quad (1.10)$$

where we have taken $n \sim 10^{15} \text{ cm}^{-3}$, $R \sim 10^{10} \text{ cm}$, and $T \sim 10^4 \text{ K}$ as representative values for the number density, the disk radius, and its temperature. This estimate contrasts sharply with observations of cataclysmic variables in which outbursts last only for a few days and thus suggest that the viscous torques acting on the disk are close to ten orders of magnitude larger than molecular viscous torques, i.e.,

$$\frac{\nu_{\text{obs}}}{\nu_{\text{mol}}} \sim \frac{t_{\text{mol}}}{t_{\text{obs}}} \sim 10^{10}. \quad (1.11)$$

The elucidation of viable physical mechanisms that could account for the required enhanced transport has been the focus of intensive work over the last three decades (see, e.g., Kato, Fukue, & Mineshige, 1998; Frank, King, & Raine, 2002).

1.3 The Standard Accretion Disk Model

The initiation of modern accretion disk theory was marked by the postulation of Shakura & Sunyaev (1973) of a source of “anomalous viscosity” thought to be operating in the disks. They offered an appealing solution to this problem by assuming a source of enhanced disk viscosity due to turbulence and magnetic fields. In essence, the transfer of angular momentum in the standard disk model rests on two distinct assumptions.

First, it is postulated that the total (vertically integrated) stress exerted on a fluid element can be modeled as a turbulent shear stress, i.e., that, in cylindrical coordinates,

$$\bar{T}_{r\phi} = -r \Sigma \nu_{\text{turb}} \frac{d\Omega}{dr}. \quad (1.12)$$

This is a turbulent version of the shear stress given by equation (1.7) usually employed to model shear viscosity in a differentially rotating laminar flow (Landau & Lifshitz, 1959), but with the coefficient of molecular kinematic viscosity, ν_{mol} , replaced by a turbulent counterpart, $\nu_{\text{turb}} = \lambda_{\text{turb}} v_{\text{turb}}$. This parameterization dictates the direction of angular momentum transport. It is always opposite to the angular velocity gradient.

Second, on dimensional grounds, Shakura and Sunyaev argued that turbulent motions in the disk would likely be restricted by the conditions $\lambda_{\text{turb}} \lesssim H$ and $v_{\text{turb}} \lesssim c_s$ and proposed to parametrize the turbulent viscosity as

$$\nu_{\text{turb}} \equiv \alpha c_s H, \quad (1.13)$$

with α a constant of the order of, but smaller than, unity. Thus, the physical mechanism that allows angular momentum transport (or more precisely diffusion) throughout different disk radii is envisioned as the viscous interaction of turbulent eddies of typical size H , on a turnover time of the order of H/c_s . In this way, the enhanced viscous coefficient, ν_{turb} , dictates the magnitude of the rate at which angular momentum is transferred. Note that, if $\alpha \sim 1$, this enhanced viscosity “solves” the angular momentum problem discussed in §1.2. Indeed, in this case, considering $H/R \sim 0.01$ leads to $\nu_{\text{turb}} \sim 10^{10} \nu_{\text{mol}}$.

The idea that turbulent angular momentum transfer in accretion disks can be described in terms of an enhanced version of the molecular transport operating in laminar differentially rotating media has been at the core of the majority of studies in accretion disk theory and phenomenology for over three decades. Since its conception, the standard accretion disk model has been extensively used to study the accretion flows surrounding young stellar objects, white dwarfs, neutron stars, and black holes on all mass scales. Much of its success lies on the fact that some disk observables are determined mostly by energy balance and depend

weakly on the adopted prescription (Balbus & Papaloizou, 1999).

However, the standard disk model is known to suffer from important shortcomings. The source of viscosity is assumed to be local; this conjecture has been challenged by numerical simulations where the turbulence has a magnetohydrodynamic, rather than hydrodynamic, origin (Armitage, 1998). The standard accretion solutions allow information to propagate across sonic points (where the flow speed equals the local sound speed), artificially connecting the inner (supersonically falling) regions of the accretion flow with the outer (nearly Keplerian) disk. Most importantly, because of its own nature, the standard accretion disk model is not self-consistent. The α -parameterization leaves unanswered fundamental questions on the origin of the assumed turbulent transport and its detailed characteristics.

1.4 The Magnetorotational Instability and MHD Turbulence

The origin of the turbulence that leads to enhanced angular momentum transport in accretion disks has been a matter of debate since the work of Shakura & Sunyaev (1973). To date, the development and sustainment of turbulence in differentially rotating media remains one of the least understood processes in modern astrophysics. In particular, the issue of whether hydrodynamic turbulence can be generated and sustained in astrophysical disks, because of the large Reynolds numbers involved, is currently a matter of renewed interest (Afshordi, Mukhopadhyay, & Narayan, 2005; Mukhopadhyay, Afshordi, & Narayan, 2005). However, this idea has long been challenged by analytical (Ryu & Goodman, 1992; Balbus & Hawley, 2006), numerical (Stone & Balbus, 1996; Balbus, Hawley, & Stone, 1996; Balbus & Hawley, 1997; Hawley, Balbus, & Winters, 1999), and, more recently, experimental work (Ji, Burin, Schartman, & Goodman, 2006).

During the last decade, it has become evident that the interplay between turbulence and magnetic fields in accretion disks is at a more fundamental level than originally conceived. There is now strong theoretical and numerical evidence suggesting that the process driving the turbulence is related to a magnetic instability, now called the magnetorotational instability (MRI), that operates in the presence of a radially decreasing angular velocity profile. The existence of this magnetic instability in differentially rotating flows was first appreciated by Velikhov (1959) and later by Chandrasekhar (1960), but its relevance to accretion disks was not fully appreciated until the work by Balbus & Hawley (1991).

The essence of the MRI can be understood by examining the equations describing the local dynamics of small amplitude perturbations in a disk threaded by a weak magnetic field. For simplicity, consider perturbations of the form $\delta \mathbf{v} = [\delta v_r(t, z), \delta v_\phi(t, z), 0]$ and $\delta \mathbf{B} = [\delta B_r(t, z), \delta B_\phi(t, z), 0]$ in an incompressible, cylindrical, differentially rotating flow, threaded by a mean vertical magnetic field, B_z (see Figure 1.1). The equations for the dynamical evolution of these fluctuations are given by¹

$$\frac{\partial}{\partial t} \delta v_r = 2\Omega \delta v_\phi + \frac{B_z}{4\pi\rho} \frac{\partial}{\partial z} \delta B_r, \quad (1.14)$$

$$\frac{\partial}{\partial t} \delta v_\phi = -\left(2 + \frac{d \ln \Omega}{d \ln r}\right) \Omega \delta v_r + \frac{B_z}{4\pi\rho} \frac{\partial}{\partial z} \delta B_\phi, \quad (1.15)$$

$$\frac{\partial}{\partial t} \delta B_r = B_z \frac{\partial}{\partial z} \delta v_r, \quad (1.16)$$

$$\frac{\partial}{\partial t} \delta B_\phi = \frac{d \ln \Omega}{d \ln r} \Omega \delta B_r + B_z \frac{\partial}{\partial z} \delta v_\phi. \quad (1.17)$$

Taking the Fourier transform of these equations with respect to time, t , and the

¹A more general and thorough derivation of this set of equations is provided in chapter 2.

vertical coordinate, z , and conveniently combining them we can write

$$-\omega^2 \delta B_r + 2i\omega\Omega \delta B_\phi = - \left[2\Omega^2 \frac{d \ln \Omega}{d \ln r} + (k_z v_{Az})^2 \right] \delta B_r, \quad (1.18)$$

$$-\omega^2 \delta B_\phi - 2i\omega\Omega \delta B_r = -(k_z v_{Az})^2 \delta B_\phi, \quad (1.19)$$

where ω stands for the frequency corresponding to the mode with vertical wavenumber k_z , and $v_{Az} \equiv B_z / \sqrt{4\pi\rho}$ stands for the Alfvén speed associated with the vertical magnetic field. The solution of this homogeneous linear system will be non-trivial only when its determinant vanishes, i.e., when the frequency ω corresponding to the mode with wavenumber k_z satisfies

$$\omega^4 - (2k_z^2 v_{Az}^2 + \kappa^2) \omega^2 + k_z^2 v_{Az}^2 \left(k_z^2 v_{Az}^2 + 2\Omega^2 \frac{d \ln \Omega}{d \ln r} \right) = 0. \quad (1.20)$$

A typical solution of this dispersion relation is shown in Figure 1.2. All the perturbations with vertical wavenumber smaller than the critical wavenumber k_{BH} are unstable (open circles), with

$$k_{BH}^2 v_{Az}^2 \equiv -2\Omega^2 \frac{d \ln \Omega}{d \ln r}. \quad (1.21)$$

As long as the magnetic field is not too strong (in order for the instability to work efficiently, some unstable modes should have vertical wavelengths smaller than the disk scaleheight) the growth rate of the instability is considerably large. For a Keplerian disk, the e -folding time for perturbations to grow is simply $3\Omega_K/4$ (right panel in Figure 1.2). This is rather fast and indeed comparable to the natural dynamical timescale at any given disk radius. The ultimate success of the MRI is that it provides a mechanism to initiate the development of turbulence in flows with Keplerian angular velocity profiles, which are believed to be very stable in the absence of magnetic fields. Indeed, unmagnetized flows with radially increasing angular momentum profiles satisfy the Rayleigh criterion for hydrodynamic stability.

The Magnetorotational Instability

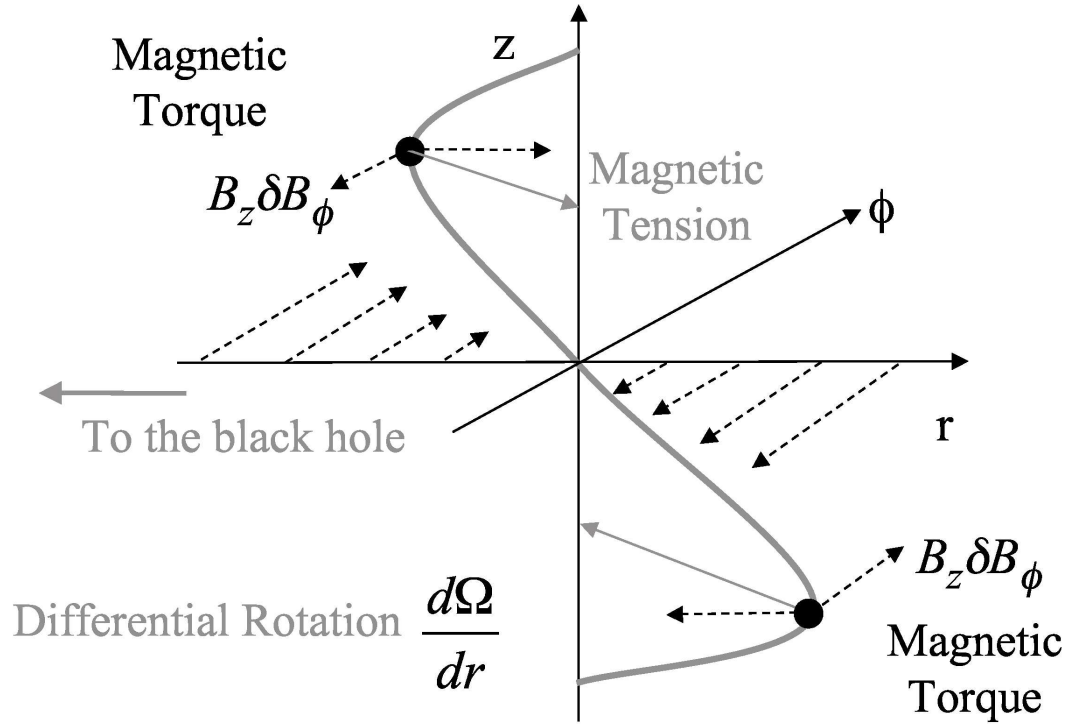


Figure 1.1 Schematics of the shearing of vertical magnetic field lines in a differentially rotating flow that leads to the runaway process known as the magnetorotational instability (MRI). The coordinate system is assumed to be in corotation with the disk at some fiducial radius. The dashed arrows in the azimuthal direction represent the background velocity field as seen from the corotating system. The azimuthal component of the restoring force due to magnetic field tension of the perturbed field line exerts a torque on the displaced fluid elements. The torque acting on the fluid element displaced towards the central object causes it to lose angular momentum. The fluid element then migrates to a lower orbit dragging with it the magnetic field line and increasing the magnetic tension responsible for the torque. A similar situation takes place with a fluid element initially displaced outwards. In this case, the angular momentum of such a fluid element increases and it migrates outwards. For a given magnetic field strength, all the perturbations with wavenumbers $k_z \leq k_{\text{BH}}$ are unstable (eq. [1.21]).

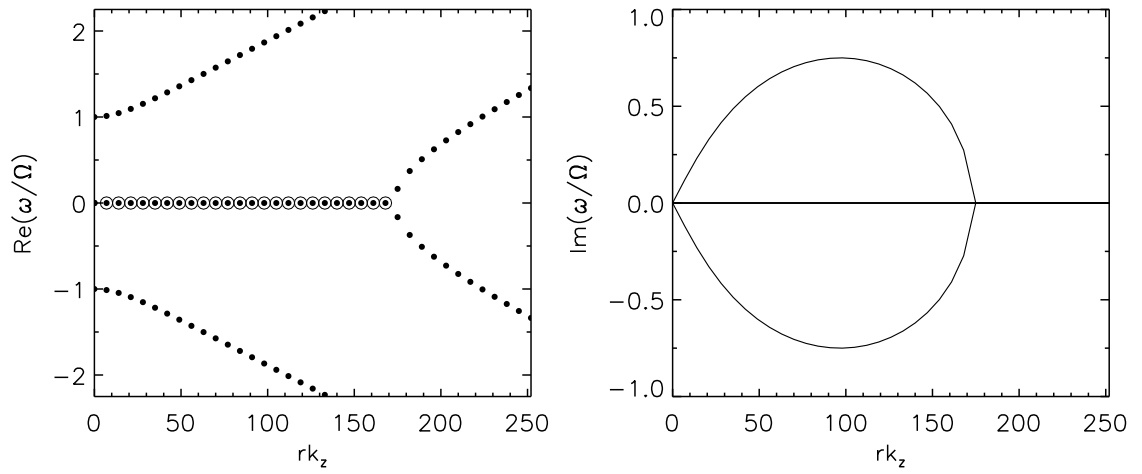


Figure 1.2 The real (left) and imaginary (right) parts of the solutions to the dispersion relation (1.20) corresponding to an incompressible Keplerian disk with $v_{Az} = 0.01\Omega r$. Open circles indicate unstable modes (i.e., those with positive imaginary part). The rightmost open circle in the left panel denotes the wavenumber corresponding to the largest unstable wavenumber, k_{BH} (eq. [1.21]).

Since the appreciation of the relevance of the MRI to accretion physics, a variety of local (Hawley, Gammie, & Balbus, 1995, 1996; Stone, Hawley, Gammie, & Balbus, 1996; Brandenburg, Nordlund, Stein, & Torkelsson, 1995; Brandenburg, 2001; Sano, Inutsuka, Turner, & Stone, 2004) and global (Armitage, 1998; Hawley, 2000, 2001; Hawley & Krolik, 2001; Stone & Pringle, 2001) numerical simulations have revealed that its long-term evolution gives rise to a turbulent state, providing a natural avenue for vigorous angular momentum transport.

Despite the fact that the MRI is currently considered the most promising mechanism to enable efficient angular momentum transport in accretion disks there is no theory available that incorporates the MRI as the input source of MHD turbulence and describes, at least qualitatively, the saturated turbulent state of magnetohydrodynamic disks found in numerical simulations. What is much needed is a dynamical model for MHD stresses in turbulent, anisotropic, differentially rotating flows. This dissertation presents an effort towards this end.

1.5 This Dissertation in Context

Since the (re)discovery of the MRI, many analytical studies have been devoted to understanding its linear evolution in a broad variety of astrophysical situations (see the reviews by Balbus & Hawley 1998 and Balbus 2003). The vast majority of these works have addressed the conditions under which the MRI can be triggered and the rate at which the instability can disrupt the background (laminar) flow in weakly magnetized disks. These studies are important for at least two reasons. First, they offer valuable insight into complicated physical processes by allowing us to concentrate on a specific aspect of a problem usually involving a large range of timescales and lengthscales. Second, they provide results against which the initial evolution of numerical simulations can be checked.

In chapter 2, I present a local stability analysis of a compressible, strongly magnetized, differentially rotating plasma taking fully into account, for the first time in a study of this type, the forces induced by the finite curvature of the toroidal magnetic field lines. The generality of this study allows me to provide a common ground to understand apparently contradictory results reached by previous works. I show that when the general dispersion relation is obtained, then all the previous results in the literature associated with this problem can be obtained by taking appropriate limits. I find that strongly magnetized differentially rotating flows are subject to three different types of magnetorotational instabilities (Pessah & Psaltis, 2005). I show that the presence of a strong toroidal field component can alter significantly the stability of the magnetized flow not only by modifying how fast the instabilities grow, but also by determining which length-scales are unstable. In particular, I demonstrate that the MRI can be completely stabilized at large scales by strong toroidal fields. However, I also find that, for a broad range of magnetic field strengths and geometries, two additional new instabilities are present. These results have important implications for the stability of strongly magnetized flows in the inner regions of accretion disks and for magnetically dominated winds in young stars. The relevance of this study lies in that it shows that differentially rotating flows are unstable to different “magnetorotational instabilities” regardless of the strength and geometry of the magnetic field. This argues in favor of the development of MHD turbulence across the entire disk or wind.

The last decade has witnessed major advances in numerical simulations of turbulent magnetized accretion disks. The increase of computational power and the development of sophisticated algorithms has allowed us to follow the development of MHD turbulence for many (several) dynamical times in local (global)

Timescales and Lengthscales in Accretion Disks

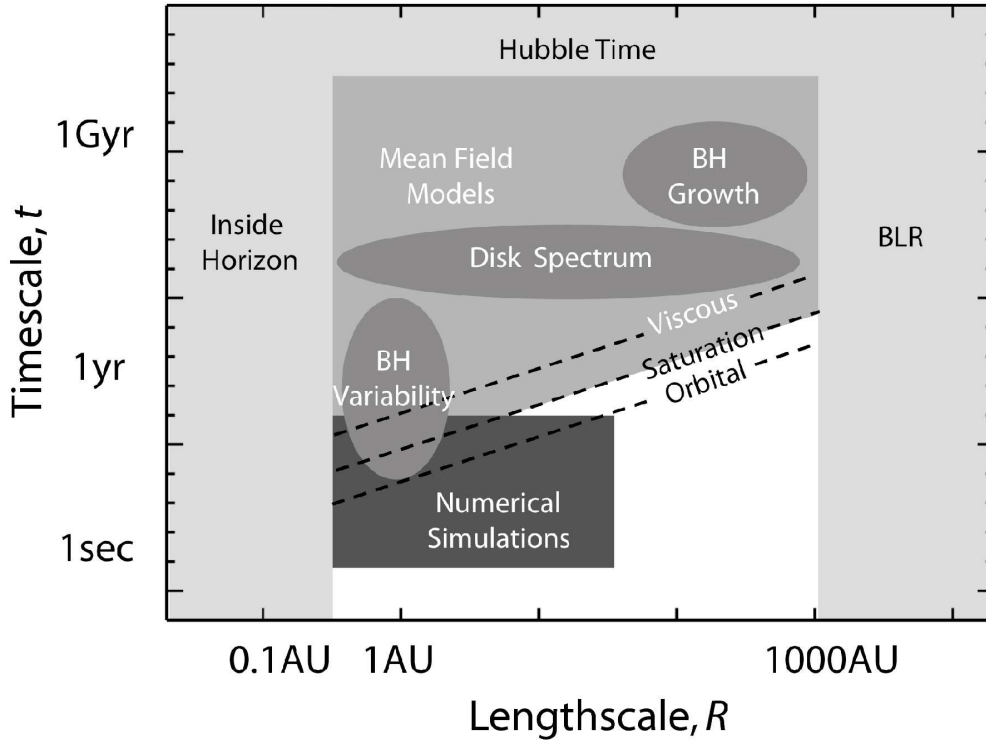


Figure 1.3 Diagram containing the various relevant timescales and lengthscales characterizing disk accretion onto a massive black hole (a mass of $M = 10^7 M_\odot$ is considered for the sake of this example). The orbital timescale is simply $t_{\text{orb}} = \sqrt{R^3/GM}$. The saturation timescale, t_{sat} , is the time that numerical simulations must be evolved in order to obtain statistically reliable estimates of turbulent flow quantities, roughly $t_{\text{sat}} \sim 100t_{\text{orb}}$. The viscous time, t_{vis} is the time that it takes for the disk to globally react to a change in the accretion rate, roughly $t_{\text{vis}} \sim (R/H)^2(t_{\text{orb}}/\alpha) \sim 10^4 t_{\text{orb}}$, for $R/H \sim 100$ and $\alpha \sim 1$. BLR stands for 'broad line region', the size of which has been taken as representative of the outer disk radius. The phenomena of interest, e.g., disk spectra, black hole growth and variability, span a huge dynamical range in both spatial and temporal scales. This makes it extremely challenging for addressing the long-term global disk phenomena with direct numerical simulations and argues in favor of complementary approaches to model the accretion flows.

numerical simulations. There is no doubt that numerical simulations will continue to be irreplaceable tools in the quest towards understanding how accretion disks work. However, because of the large temporal and spatial dynamical ranges involved (Figure 1.3), the study of the long-term evolution of the accretion flows and of the accreting objects will remain beyond reach in the near future.

Current state-of-the-art numerical codes can evolve non-radiative, thick, black hole accretion disks that span at most one hundred gravitational radii for at most a few hundred orbits. Realistic time-explicit numerical simulations to address the long-term evolution (millions of orbits) of an entire turbulent magnetized radiatively efficient, thin, disk (spanning thousands of gravitational radii) will remain beyond the horizon of computational astrophysics for quite some time to come. Order-of-magnitude estimates carried out by Ogilvie (2003) suggest that in order to evolve a realistic thin disk over many viscous timescales is at least a factor of 10^{10} more demanding than the efforts involved in local numerical simulations spanning a few dynamical timescales². It is then evident that, in order to address some of the long-standing problems in accretion physics including the global structure, stability, long-term evolution, and observational signatures of turbulent magnetized disks, it is necessary for us to follow a complementary approach.

In order to bridge the existing gap between local stress dynamics, which are amenable to study with current computational resources, and long-term global disk dynamics, it is essential to develop more realistic models for the physical processes that take place on fast (dynamical) timescales. The first obvious, and arguably most important, candidate to model is the turbulent transport of angular momentum.

²This estimate assumes that one would like to obtain the same level of detail in both types of simulations.

Turbulent MHD stresses play a crucial role in determining the global disk structure and its dynamical evolution by removing angular momentum from the disk. Therefore, understanding their physical properties is crucial for developing reliable theoretical disk models. However, the complexity characterizing MHD turbulence has hampered this endeavor for several decades. Because of this, analytical insight into this problem is highly valuable.

All previous stability analyses addressing the relevance of the MRI to the angular momentum transport problem have calculated the eigenfrequencies (growth rates) associated with the unstable modes under different circumstances (but see Goodman & Xu 1994). In chapter 3, I calculate, for the first time, in collaboration with C.K. Chan (Pessah, Chan, & Psaltis, 2006a), the eigenvectors corresponding to the problem defined by the MRI. This allows me to follow the temporal evolution of the Fourier amplitudes of the fluctuations in the velocity and magnetic fields. Moreover, I present the formalism to calculate the mean value of MRI-driven stresses that result from the correlations among exponentially growing fluctuations. I show that some characteristics of the stresses observed in the fully developed turbulent state observed in 3-dimensional numerical simulations are determined during the onset of the magnetic instability (MRI) driving and sustaining the MHD turbulence. This possibility has been suspected for many years, but this is the first time that a quantitative assessment is provided. These result suggests that the mechanism leading to the saturation of the instability, whose details are not yet understood, must work in a very particular way.

Guided by the results of chapter 3, I present in chapter 4 a dynamical model for angular momentum transport in MRI-driven accretion disks (Pessah, Chan, & Psaltis, 2006b). This is the first model that can describe (with only two parameters) the most relevant aspects of angular momentum transfer as revealed by

local 3-dimensional numerical simulations (Hawley, Gammie, & Balbus, 1995). Moreover, I uncover the importance of a new quantity that plays a key role in the accretion process in turbulent magnetized disks. I show that considering the dynamical effects of this new quantity is the only possible way to account for the exponential growth of the stresses observed during the initial stages of numerical simulations. This is a fundamentally new result in the context of both dynamo theory and MRI-driven turbulence.

With the help of the model for angular momentum transport derived in chapter 5, and by performing a series of numerical studies with the `ZEUS` code (Stone & Norman, 1992a,b; Stone, Mihalas, & Norman, 1992), in collaboration with C.K. Chan, I show that MHD turbulent stresses are not proportional to the local shear (Pessah, Chan, & Psaltis, 2007). This finding challenges one of the central assumptions in the standard α -model and calls for a reassessment of the theoretical foundations of turbulent magnetized accretion disks. If MHD turbulence driven by the MRI is indeed the relevant mechanism for angular momentum transfer, then these results may have important implications for the global structure of the accretion disks and thus for their observational properties.

Finally, in chapter 6, I present a summary and comment on some future lines of work aimed at improving our fundamental understanding on how accretion disks work.

CHAPTER 2

THE STABILITY OF MAGNETIZED ROTATING PLASMAS WITH SUPERTHERMAL FIELDS

During the last decade it has become evident that the magnetorotational instability is at the heart of the enhanced angular momentum transport in weakly magnetized accretion disks around neutron stars and black holes.

In this chapter, we investigate the local linear stability of differentially rotating, magnetized flows and the evolution of the magnetorotational instability beyond the weak-field limit. We show that, when superthermal toroidal fields are considered, the effects of both compressibility and magnetic tension forces, which are related to the curvature of toroidal field lines, should be taken fully into account. We demonstrate that the presence of a strong toroidal component in the magnetic field plays a non-trivial role. When strong fields are considered, the strength of the toroidal magnetic field not only modifies the growth rates of the unstable modes but also determines which modes are subject to instabilities. We find that, for rotating configurations with Keplerian laws, the magnetorotational instability is stabilized at low wavenumbers for toroidal Alfvén speeds exceeding the geometric mean of the sound speed and the rotational speed. For a broad range of magnetic field strengths, we also find that two additional distinct instabilities are present; they both appear as the result of coupling between the modes that become the Alfvén and the slow modes in the limit of no rotation.

We discuss the significance of our findings for the stability of cold, magnetically dominated, rotating fluids and show that, for these systems, the curvature of toroidal field lines cannot be neglected even when short wavelength perturbations are considered. We also comment on the implications of our results for the

validity of shearing box simulations in which strong toroidal fields are generated.

2.1 Introduction

Linear mode analyses provide a useful tool in gaining important insight into the relevant physical processes determining the stability of magnetized accretion flows. Studies of local linear modes of accretion disks threaded by weak magnetic fields have offered important clues on viable mechanisms for angular momentum transport and the subsequent accretion of matter onto the central objects (Balbus & Hawley, 1991, 1998, 2002; Sano & Miyama, 1999; Balbus, 2003). They have also provided simplified physical models and analogies over which more complex physics can, in principle, be added (Balbus & Hawley, 1992, 1998; Quataert, Dorland, & Hammett, 2002). These treatments were carried out in the magnetohydrodynamic (MHD) limit (but see Quataert, Dorland & Hammett 2002 who studied the kinetic limit) and invoked a number of approximations appropriate to the study of the evolution of short-wavelength perturbations, when weak fields are considered. In this context, the strength of the magnetic field, B , is inferred by comparing the thermal pressure, P , to the magnetic pressure and is characterized by a plasma parameter, $\beta \equiv 8\pi P/B^2 > 1$.

It is not hard to find situations of astrophysical interest, however, in which the condition of weak magnetic fields is not satisfied. A common example of such a situation is the innermost region of an accretion disk around a magnetic neutron star. It is widely accepted that X-ray pulsars are powered by accretion of matter onto the polar caps of magnetic neutron stars. For this to occur, matter in the nearly Keplerian accretion disk has to be funneled along the field lines. This suggests that, at some radius, centrifugal forces and thermal pressure have to be overcome by magnetic stresses, leading naturally to regions where $\beta \lesssim 1$.

In the context of accretion disks, the presence of superthermal fields in rarefied coronae also seems hard to avoid, if coronal heating is a direct consequence of the internal dynamics of the disk itself rather than being produced by external irradiation from the central object. Three-dimensional MHD simulations by Miller & Stone (2000) showed that magnetic turbulence can effectively couple with buoyancy to transport the magnetic energy produced by the magnetorotational instability (MRI) in weakly magnetized disks and create a strongly magnetized corona within a few scale heights from the disk plane. On long time scales, the average vertical disk structure consists of a weakly magnetized ($\beta \simeq 50$) turbulent core below two scale heights and a strongly magnetized ($\beta \lesssim 0.1$) non-turbulent corona above it. The late stages of evolution in these models show that the disks themselves become magnetically dominated. Machida, Hayashi, & Matsumoto (2000) also found that the average plasma β in disk coronae is $\simeq 0.1 - 1$ and the volume filling factor for regions with $\beta \lesssim 0.3$ is up to 0.1. Even in the absence of an initial toroidal component, simulations carried out by Kudoh, Matsumoto, & Shibata (2002) showed that low- β regions develop near the equator of the disk because of a strong toroidal component of the magnetic field generated by shear. On more theoretical grounds, strong toroidal magnetic fields produced by strong shear in the boundary layer region have been suggested as responsible for the observed bipolar outflows in young stellar objects (Pringle, 1989). More recently, Pariev, Blackman, & Boldyrev (2003) found self-consistent solutions for thin magnetically-supported accretion disks and pointed out the necessity of assessing the stability properties of such configurations.

Another case in which magnetic fields seem to play an important dynamical role in rotating fluid configurations is that of magnetically supported molecular clouds. Observations of both large Zeeman line-splitting and of broad molecular

lines support the presence of superthermal fields (see Myers & Goodman 1988 for further references and Bourke & Goodman 2003 for a review on the current understanding on the role of magnetic fields in molecular clouds). Values of the plasma β of the order of $0.1 - 0.01$ have also been used in numerical studies of the structural properties of giant molecular clouds (Ostriker, Stone, & Gammie, 2001).

As a last example of astrophysical interest, we mention magnetocentrifugally driven winds, such as those observed in protostars. These outflows seem to play an important role in the evolution of young stellar objects and in the dynamics of the parent clouds by providing a source of turbulent energy. Magnetocentrifugal jets typically involve internal Alfvén speeds comparable to the flow speeds. These structures are supported mainly by magnetic pressure due to strong toroidal fields. The ratio of magnetic pressure in the jet to the gas pressure of the ambient medium can be of the order of 10^6 (for an extensive study of MHD driven instabilities in these systems see Kim & Ostriker 2000 and §2.5.3).

In this chapter, we investigate the local linear stability of differentially rotating flows without imposing any *a priori* restrictions on the strength of the magnetic field. We do, however, restrict our attention to rotationally supported flows (we loosely use this term to refer to flows with internal Alfvén speeds smaller than the rotational speed). Our intent is to demonstrate that the effects of the finite curvature of the toroidal field lines on the stability of small-wavelength vertical perturbations (i.e., on the most unstable modes present in the weak-field MRI) cannot be neglected when superthermal toroidal fields are present. In order to achieve this task, we relax the Boussinesq approximation (see also Papaloizou & Szuszkiewicz 1992 and Blaes & Balbus 1994), which is valid only when the toroidal component of the field is subthermal (Balbus & Hawley, 1991). We thus

consider the MHD fluid to be fully compressible. Moreover, even though we perform a local analysis, we do consider curvature terms when evaluating magnetic forces, for they become important in the strong-field regime (see also Knobloch 1992 and Kim & Ostriker 2000).

In most early studies addressing the MRI, it was found that the only role played by a toroidal component in the magnetic field is to quench the growth rates of the modes that are already unstable when only weak vertical fields are considered (Balbus & Hawley 1991; Blaes & Balbus 1994; see Quataert, Dorland, & Hammett 2002 for the kinetic limit; see also Kim & Ostriker 2000 for the cold MHD limit). Here, we show that, when strong fields are considered and the approximations usually invoked in the study of the weak-field MRI are relaxed, the presence of a toroidal component of the magnetic field plays a crucial role not only in the growth rates of the unstable modes but also in determining which modes are subject to instabilities¹. As expected, the presence of a toroidal component breaks the symmetry of the problem, also giving rise to traveling modes. Moreover, for a broad range of magnetic field strengths, we find that two different instabilities are present. They both appear as the result of coupling between the modes that become the Alfvén and the slow mode in the limit of no rotation.

This chapter is organized as follows. In §2.2, we describe the physical setup to be studied, present the dispersion relation to be solved, and discuss the importance of curvature terms in the limit of superthermal fields. In §2.3, we solve numerically the dispersion relation in some interesting regimes. In §2.4, we study the onset of instabilities as a function of magnetic field strengths and present some useful approximate criteria that enable us to study analytically some as-

¹We will comment later in more detail on the paper by Curry & Pudritz (1995) who outlined the effects of a dynamically important toroidal field (in the case of an incompressible MHD flow) and address the similitudes and differences with our findings.

pects of the full problem. In §2.5, we compare our results to previous investigations and discuss some of the implications of this study. Finally, in §2.6, we present a brief summary and our conclusions.

2.2 MHD Equations for Perturbations and the Dispersion Relation

We start with the set of equations that govern the behavior of a polytropic fluid in the MHD approximation,

$$\frac{\partial \rho}{\partial t} + \nabla \cdot (\rho \mathbf{v}) = 0, \quad (2.1)$$

$$\rho \frac{\partial \mathbf{v}}{\partial t} + (\rho \mathbf{v} \cdot \nabla) \mathbf{v} = -\rho \nabla \Phi - \nabla \left(P + \frac{B^2}{8\pi} \right) + \left(\frac{\mathbf{B}}{4\pi} \cdot \nabla \right) \mathbf{B}, \quad (2.2)$$

$$\frac{\partial \mathbf{B}}{\partial t} + (\nabla \cdot \mathbf{v}) \mathbf{B} - (\mathbf{B} \cdot \nabla) \mathbf{v} + (\mathbf{v} \cdot \nabla) \mathbf{B} = 0, \quad (2.3)$$

and

$$P = P_0 \left(\frac{\rho}{\rho_0} \right)^\Gamma. \quad (2.4)$$

In these equations, ρ is the mass density, \mathbf{v} the velocity, P the gas pressure, and Γ the polytropic index; \mathbf{B} is the magnetic field and Φ the gravitational potential. For convenience we adopt a cylindrical set of coordinates (r, ϕ, z) with origin in the central object (i.e., the neutron star or black hole). We assume a steady axisymmetric background flow characterized by a velocity field of the form $\mathbf{v} = v_\phi(r, z)\hat{\phi}$ and threaded by a background magnetic field. For consistency, our analysis is restricted to background fields of the form $\mathbf{B} = B_\phi \hat{\phi} + B_z \hat{z}$ since the effect of including a radial component in the field is to generate a linear growth in time of the toroidal component (Balbus & Hawley, 1991). Under these circumstances, all the background quantities depend on the radial and vertical coordinates only. In the present treatment, we neglect the self gravity of the fluid. In fact, Pariev, Blackman, & Boldyrev (2003) showed that magnetically dominated accretion disks

have lower surface and volume densities for a fixed accretion rate. This suggests that these systems are lighter than standard disks and thus are not subject to self-gravity instabilities.

2.2.1 Equations for the Perturbations

In order to perform the local linear mode analysis, we perturb the set of equations (2.1)-(2.4) by substituting every physical variable f by $f + \delta f$ and retain only linear orders in δf . In the following, we focus our analysis on the study of axisymmetric perturbations in an axisymmetric background.

We first consider, in some detail, the radial component of the momentum equation (2.2), which becomes

$$\begin{aligned}
 \frac{\partial \delta v_r}{\partial t} &= 2\Omega \delta v_\phi + \frac{1}{\rho} \left[\frac{\partial \delta P}{\partial r} + \frac{1}{4\pi} \left(\frac{\partial B_\phi}{\partial r} \delta B_\phi + B_\phi \frac{\partial \delta B_\phi}{\partial r} + \frac{\partial B_z}{\partial r} \delta B_z + B_z \frac{\partial \delta B_z}{\partial r} \right) \right] \\
 &- \frac{\partial P}{\partial r} \frac{\delta \rho}{\rho^2} - \frac{1}{4\pi \rho} \left(B_\phi \frac{\partial B_\phi}{\partial r} + B_z \frac{\partial B_z}{\partial r} \right) \frac{\delta \rho}{\rho} - \frac{1}{4\pi \rho} \left[B_z \frac{\partial \delta B_r}{\partial z} - 2 \frac{B_\phi}{r} \delta B_\phi \right] \\
 &- \frac{1}{4\pi \rho} \frac{B_\phi^2}{r} \frac{\delta \rho}{\rho} = 0.
 \end{aligned} \tag{2.5}$$

The coefficients in this linear equation for the perturbed variables depend in general on r and z , [e.g., the angular velocity Ω is in general $\Omega(r, z)$]. Therefore, at this point, the decomposition of perturbed quantities into Fourier modes – e.g., symbolically $\delta f = \sum \delta f_k e^{i(k_r r + k_z z - \omega t)}$ – would not result in any particular simplification of the problem. This can be seen by taking the Fourier transform of equation (2.5) which results in a sum of convolutions of the Fourier transforms of background and perturbed quantities. Further progress can be made if we restrict the wavelengths of the perturbations for which our stability analysis is valid. To this end, we choose a fiducial point, $\mathbf{r}_0 = (r_0, \phi_0, z_0)$, around which we perform the local stability analysis. The choice of the particular value of ϕ_0 is, of course, irrelevant in the axisymmetric case under study.

We expand all the background quantities in equation (2.5) in Taylor series around \mathbf{r}_0 and retain only the zeroth order in terms of the local coordinates $\xi_r = r - r_0$ and $\xi_z = z - z_0$ to obtain

$$\begin{aligned}
\frac{\partial \delta v_r}{\partial t} &= 2\Omega_0 \delta v_\phi \\
&+ \frac{1}{\rho_0} \left[\frac{\partial \delta P}{\partial \xi_r} + \frac{1}{4\pi} \left(\left. \frac{\partial B_\phi}{\partial r} \right|_0 \delta B_\phi + B_\phi^0 \frac{\partial \delta B_\phi}{\partial \xi_r} + \left. \frac{\partial B_z}{\partial r} \right|_0 \delta B_z + B_z^0 \frac{\partial \delta B_z}{\partial \xi_r} \right) \right] \\
&- \left. \frac{\partial P}{\partial r} \right|_0 \frac{\delta \rho}{\rho_0^2} - \frac{1}{4\pi \rho_0} \left(B_\phi^0 \left. \frac{\partial B_\phi}{\partial r} \right|_0 + B_z^0 \left. \frac{\partial B_z}{\partial r} \right|_0 \right) \frac{\delta \rho}{\rho_0} \\
&- \frac{1}{4\pi \rho_0} \left(B_z^0 \frac{\partial \delta B_r}{\partial \xi_z} - 2 \frac{B_\phi^0}{r_0} \delta B_\phi \right) - \frac{1}{4\pi \rho_0} \frac{(B_\phi^0)^2}{r_0} \frac{\delta \rho}{\rho_0} = 0 .
\end{aligned} \tag{2.6}$$

Here, Ω_0 , ρ_0 , B_ϕ^0 , and B_z^0 stand for the angular velocity, background density, and magnetic field components at the fiducial point \mathbf{r}_0 and the subscript “0” in the derivatives with respect to the radial coordinate r indicates that they are evaluated at \mathbf{r}_0 . Equation (2.6) is a linear partial-differential equation in the local variables for the perturbed quantities but with constant coefficients. This is a good approximation as long as the departures (ξ_r, ξ_z) are small compared to the length scales over which there are significant variations in the background quantities, i.e, $\xi_r \ll L_r$ and $\xi_z \ll L_z$, where L_r and L_z are the characteristic length scales in the radial and vertical directions, respectively.

It is only now that it is useful to expand the perturbed quantities in equation (2.6) into Fourier modes. We can thus write each one of the perturbed quantities as

$$\delta f = \delta f(k_r, k_z, \omega) e^{i(k_r \xi_r + k_z \xi_z - \omega t)} , \tag{2.7}$$

and write the radial momentum equation for each mode as

$$\begin{aligned}
-i\omega\delta v_r &= 2\Omega_0\delta v_\phi - ik_z \frac{B_z^0\delta B_r}{4\pi\rho_0} + \left(ik_r + \frac{2}{r_0} + \frac{\partial \ln B_\phi}{\partial r} \Big|_0 \right) \frac{B_\phi^0\delta B_\phi}{4\pi\rho_0} \\
&+ \left(ik_r + \frac{\partial \ln B_z}{\partial r} \Big|_0 \right) \frac{B_z^0\delta B_z}{4\pi\rho_0} + \left(ik_r - \frac{\partial \ln \rho}{\partial r} \Big|_0 \right) (c_s^0)^2 \frac{\delta\rho}{\rho_0} \\
&- \left[\left(\frac{1}{r_0} + \frac{\partial \ln B_\phi}{\partial r} \Big|_0 \right) (v_{A\phi}^0)^2 \frac{\partial \ln B_z}{\partial r} \Big|_0 (v_{Az}^0)^2 \right] \frac{\delta\rho}{\rho_0} = 0. \quad (2.8)
\end{aligned}$$

Here, we have introduced the quantities c_s^0 , $v_{A\phi}^0$ and v_{Az}^0 that stand for the local sound speed and local Alfvén speeds associated with the toroidal and vertical components of the local magnetic field and are defined by

$$c_s^0 \equiv \sqrt{\Gamma \frac{P_0}{\rho_0}}, \quad v_{A\phi}^0 \equiv \frac{B_\phi^0}{\sqrt{4\pi\rho_0}}, \quad \text{and} \quad v_{Az}^0 \equiv \frac{B_z^0}{\sqrt{4\pi\rho_0}}. \quad (2.9)$$

Note that, for brevity, we have omitted the dependences (k_r, k_z, ω) in the Fourier amplitudes. For consistency, the validity of the analysis is now restricted to modes with wavenumbers satisfying $k_r L_r \gg 1$ and $k_z L_z \gg 1$. Without loss of generality, we assume that the fiducial point is inside the disk so we can write the local conditions on the wavenumbers as $k_r r_0 \gg 1$ and $k_z z_0 \gg 1$. Moreover, for fiducial points such that $r_0 \geq z_0$ the latter condition also implies $k_z r_0 \gg 1$.

At this point, it is also convenient to define a new set of independent variables $(\delta v_{Ar}, \delta v_{A\phi}, \delta v_{Az})$ defined in terms of $(\delta B_r, \delta B_\phi, \delta B_z)$ in such a way that $\delta \mathbf{v}_A \equiv \delta \mathbf{B} / \sqrt{4\pi\rho_0}$. In this case, equation (2.8) reads

$$\begin{aligned}
&- i\omega\delta v_r - 2\Omega_0\delta v_\phi - ik_z v_{Az}^0 \delta v_{Ar} \\
&+ \left\{ \left(ik_r - \frac{\partial \ln \rho}{\partial r} \Big|_0 \right) (c_s^0)^2 - \left[\left(\frac{1}{r_0} + \frac{\partial \ln B_\phi}{\partial r} \Big|_0 \right) (v_{A\phi}^0)^2 + \frac{\partial \ln B_z}{\partial r} \Big|_0 (v_{Az}^0)^2 \right] \right\} \frac{\delta\rho}{\rho_0} \\
&+ \left(ik_r + \frac{2}{r_0} + \frac{\partial \ln B_\phi}{\partial r} \Big|_0 \right) v_{A\phi}^0 \delta v_{A\phi} + \left(ik_r + \frac{\partial \ln B_z}{\partial r} \Big|_0 \right) v_{Az}^0 \delta v_{Az} = 0. \quad (2.10)
\end{aligned}$$

As a last step, it is useful to work with dimensionless quantities. To this end, we define dimensionless variables by scaling all the frequencies with the local rotational frequency Ω_0 and all speeds with the local circular velocity $\Omega_0 r_0$. It is also

convenient to define dimensionless wavenumbers by multiplying the physical wavenumber by the radial coordinate r_0 . In summary, we define

$$\tilde{\omega} = \omega/\Omega_0, \quad \tilde{k}_r = k_r r_0, \quad \tilde{k}_z = k_z r_0, \quad (2.11)$$

$$\tilde{c}_s^0 = c_s^0/\Omega_0 r_0, \quad \tilde{v}_{A\phi}^0 = v_{A\phi}^0/\Omega_0 r_0, \quad \tilde{v}_{Az}^0 = v_{Az}^0/\Omega_0 r_0, \quad (2.12)$$

$$\delta\tilde{\rho} = \delta\rho/\rho_0, \quad \delta\tilde{\mathbf{v}} = \delta\mathbf{v}/\Omega_0 r_0, \quad \delta\tilde{\mathbf{v}}_A = \delta\mathbf{v}_A/\Omega_0 r_0. \quad (2.13)$$

For completeness, we introduce here the epicyclic frequency κ and its local dimensionless counterpart

$$\kappa = 2\Omega \left[1 + \frac{1}{2} \frac{d \ln \Omega}{d \ln r} \right]^{1/2} \quad \text{and} \quad \tilde{\kappa}_0 = \frac{\kappa_0}{\Omega_0} = 2 \left[1 + \frac{1}{2} \frac{d \ln \Omega}{d \ln r} \Big|_0 \right]^{1/2}. \quad (2.14)$$

This quantity appears naturally in stability analyses of differentially rotating configurations and it is the frequency at which all the flow variables oscillate around their background values in the absence of magnetic fields. For a rotational profile given by a power law, the epicyclic frequency is proportional to the angular frequency at all radii.

Finally, the dimensionless version of equation (2.10) reads,

$$\begin{aligned} & -i\tilde{\omega}\delta\tilde{v}_r - 2\delta\tilde{v}_\phi - i\tilde{k}_z\tilde{v}_{Az}^0\delta\tilde{v}_{Ar} \\ & + \left\{ \left(i\tilde{k}_r - \frac{\partial \ln \rho}{\partial \ln r} \Big|_0 \right) (\tilde{c}_s^0)^2 - \left[\left(1 + \frac{\partial \ln B_\phi}{\partial \ln r} \Big|_0 \right) (\tilde{v}_{A\phi}^0)^2 + \frac{\partial \ln B_z}{\partial \ln r} \Big|_0 (\tilde{v}_{Az}^0)^2 \right] \right\} \delta\tilde{\rho} \\ & + \left(i\tilde{k}_r + 2 + \frac{\partial \ln B_\phi}{\partial \ln r} \Big|_0 \right) \tilde{v}_{A\phi}^0 \delta\tilde{v}_{A\phi} + \left(i\tilde{k}_r + \frac{\partial \ln B_z}{\partial \ln r} \Big|_0 \right) \tilde{v}_{Az}^0 \delta\tilde{v}_{Az} = 0. \end{aligned} \quad (2.15)$$

Following a similar procedure with the remaining equations in the system (2.1)-(2.4), we arrive to the linear set of equations needed to perform the local stability analysis. For brevity, we now drop the hat in all the dimensionless variables and the superscript in \tilde{c}_s^0 , $\tilde{v}_{A\phi}^0$ and \tilde{v}_{Az}^0 . We then write

$$-i\omega\delta\rho + \left(ik_r + \epsilon_4 + \frac{\partial \ln \rho}{\partial \ln r} \Big|_0 \right) \delta v_r + \left(ik_z + \frac{r_0}{z_0} \frac{\partial \ln \rho}{\partial \ln z} \Big|_0 \right) \delta v_z = 0, \quad (2.16)$$

$$\begin{aligned}
& - i\omega\delta v_r - 2\delta v_\phi - ik_z v_{Az}\delta v_{Ar} \\
& + \left(ik_r + 2\epsilon_1 + \frac{\partial \ln B_\phi}{\partial \ln r} \Big|_0 \right) v_{A\phi}\delta v_{A\phi} + \left(ik_r + \frac{\partial \ln B_z}{\partial \ln r} \Big|_0 \right) v_{Az}\delta v_{Az} \\
& + \left\{ \left(ik_r - \frac{\partial \ln \rho}{\partial \ln r} \Big|_0 \right) c_s^2 - \left[\left(\epsilon_2 + \frac{\partial \ln B_\phi}{\partial \ln r} \Big|_0 \right) v_{A\phi}^2 + \frac{\partial \ln B_z}{\partial \ln r} \Big|_0 v_{Az}^2 \right] \right\} \delta \rho = 0 ,
\end{aligned} \tag{2.17}$$

$$\begin{aligned}
-i\omega\delta v_\phi + \frac{\kappa^2}{2}\delta v_r + \frac{r_0}{z_0} \frac{\partial \ln \Omega}{\partial \ln z} \Big|_0 \delta v_z & - \left(\epsilon_3 + \frac{\partial \ln B_\phi}{\partial \ln r} \Big|_0 \right) v_{A\phi}\delta v_{Ar} \\
& - ik_z v_{Az}\delta v_{A\phi} - \frac{r_0}{z_0} \frac{\partial \ln B_\phi}{\partial \ln z} \Big|_0 v_{A\phi}\delta v_{Az} = 0 ,
\end{aligned} \tag{2.18}$$

$$\begin{aligned}
-i\omega\delta v_z & - \frac{\partial \ln B_z}{\partial \ln r} \Big|_0 v_{Az}\delta v_{Ar} + \left(ik_z + \frac{r_0}{z_0} \frac{\partial \ln B_\phi}{\partial \ln z} \Big|_0 \right) v_{A\phi}\delta v_{A\phi} \\
& + \left[\left(ik_z - \frac{r_0}{z_0} \frac{\partial \ln \rho}{\partial \ln z} \Big|_0 \right) c_s^2 - \frac{r_0}{z_0} \left(\frac{\partial \ln B_\phi}{\partial \ln z} \Big|_0 v_{A\phi}^2 + \frac{\partial \ln B_z}{\partial \ln z} \Big|_0 v_{Az}^2 \right) \right] \delta \rho = 0 ,
\end{aligned} \tag{2.19}$$

$$i\omega\delta v_{Ar} + ik_z v_{Az}\delta v_r = 0 , \tag{2.20}$$

$$\begin{aligned}
-i\omega\delta v_{A\phi} & - \frac{d \ln \Omega}{d \ln r} \Big|_0 \delta v_{Ar} - \frac{r_0}{z_0} \frac{d \ln \Omega}{d \ln z} \Big|_0 \delta v_{Az} - ik_z v_{Az}\delta v_\phi \\
& + \left(ik_r + \frac{\partial \ln B_\phi}{\partial \ln r} \Big|_0 \right) v_{A\phi}\delta v_r + \left(ik_z + \frac{r_0}{z_0} \frac{\partial \ln B_\phi}{\partial \ln z} \Big|_0 \right) v_{A\phi}\delta v_z = 0 ,
\end{aligned} \tag{2.21}$$

and

$$-i\omega\delta v_{Az} + \left(ik_r + \epsilon_4 + \frac{\partial \ln B_z}{\partial \ln r} \Big|_0 \right) v_{Az}\delta v_r = 0 , \tag{2.22}$$

where we have used equation (2.4) to recast the pressure perturbations in terms of density perturbations. The local conditions over the wavenumbers now read $k_r \gg 1$ and $k_z \gg 1$.

The factors ϵ_i , with $i = 1, 2, 3, 4$, are just convenient dummy variables that we introduce in order to help us keep track of the terms that account for the finite curvature of the background and are usually neglected in local studies of the weak-field MRI. Their numerical values are to be regarded as unity, unless otherwise mentioned. The terms proportional to ϵ_1 and ϵ_2 in equation (2.17) and the term proportional to ϵ_3 in equation (2.18) are due to the effects of magnetic tension and they appear naturally when a cylindrical coordinate system is adopted. The terms proportional to ϵ_4 in equations (2.16) and (2.22) are related to flux conservation in cylindrical coordinates. Although the three terms labeled by ϵ_1 , ϵ_2 , and ϵ_3 share the same physical origin (i.e., magnetic tension introduced by the curvature of toroidal field lines), it is useful to be able to distinguish among them because the one labeled with ϵ_2 vanishes in the limit of an incompressible flow. Note that equations (2.20) and (2.22) ensure a divergence-free perturbed magnetic field, i.e., $\nabla \cdot \delta \mathbf{B} = 0$, only when the finite curvature of the background is accounted for (i.e., $\epsilon_4 = 1$).

Up to this point, our intention has been to keep the discussion as general as possible in order to clearly state all the assumptions that we have made to obtain the set of equations for the perturbations to perform a local linear mode analysis. For the sake of simplicity, and to avoid the parametric study from being too extensive, we further invoke the following assumptions. We choose the fiducial point \mathbf{r}_0 to lie in the disk mid-plane and assume that, locally, the vertical gradients in all background quantities are negligible and set them to zero. This will be a good approximation as long as we consider equilibrium configurations such that

$$\left| \frac{d \ln \rho}{d \ln z} \right|_0 \ll 1, \quad \left| \frac{d \ln B_\phi}{d \ln z} \right|_0 \ll 1, \quad \text{and} \quad \left| \frac{d \ln \Omega}{d \ln z} \right|_0 \ll 1. \quad (2.23)$$

Note that the solenoidal character of the magnetic field ensures that, for $\mathbf{B} =$

$B_\phi(r, z)\hat{\phi} + B_z(r, z)\hat{z}$, the condition $\partial B_z/\partial z = 0$ holds for arbitrary z .

In general, the forces induced by the curvature terms (e.g., the one proportional to ϵ_2 in eq. [2.17]) and those induced by background (logarithmic) gradients in the radial direction, (e.g., the term proportional to $d \ln B_\phi / d \ln r|_0$ in the same equation) will not cancel each other. As a single exception, for the case in which $B_\phi \propto r^{-1}$, the most important effects due to the finite curvature of toroidal field lines are canceled out by the gradients in the toroidal field. This particular case, however, might not be completely relevant to realistic rotating flows since, in order to ensure force balance when the thermal pressure can be neglected against magnetic stresses, the magnetic field strength must decline more slowly than r^{-1} (see, e.g., Kim & Ostriker 2000). For simplicity, we further focus our attention on the study of differentially rotating, axisymmetric MHD flows with locally negligible radial gradients in the background density and magnetic field, i.e.,

$$\left| \frac{d \ln \rho}{d \ln r} \right|_0 \ll 1, \quad \left| \frac{d \ln B_\phi}{d \ln r} \right|_0 \ll 1, \quad \text{and} \quad \left| \frac{d \ln B_z}{d \ln r} \right|_0 \ll 1. \quad (2.24)$$

In the rest of the chapter, we consider that the only background flow variable with a non-negligible local radial gradient is the angular velocity $\Omega \propto r^{-q}$ and set all other radial gradients to zero. Note that this assumption is widely invoked in many investigations of the weak-field MRI (e.g., Blaes & Balbus 1994; Balbus & Hawley 1998; Blaes & Socrates 2001; Quataert, Dorland, & Hammett 2002; Balbus 2003). This assumption is also generally a part of the initial set of conditions used in many numerical analyses of the MRI in the shearing box approximation (e.g., Hawley, Gammie, & Balbus 1994, 1995, 1996; Miller & Stone 2000).

In spite of being linear in the perturbed quantities, the terms proportional to ϵ_i have been neglected in previous local studies of the MRI under the assumption that $k_r \gg 1$ and $k_z \gg 1$ (but see also Knobloch 1992 and Kim & Ostriker 2000). Although comparing an imaginary term against a real one in a stability

analysis might seem particularly risky, this might not be a bad argument in order to neglect the terms proportional to ϵ_1 in equation (2.17) or ϵ_4 in equations (2.16) and (2.22) against ik_r (but see the discussion in Appendix A). The same could be said about the terms proportional to ϵ_2 in equation (2.17) or ϵ_3 in equation (2.18) in the limit of a very weak toroidal component in the magnetic field, given that both of them are proportional to $v_{A\phi}$. It is not evident, however, that we can neglect the terms proportional to either ϵ_2 in equation (2.17) or ϵ_3 in equation (2.18) if we are to explore the regime of strong toroidal fields. There are two different reasons for this. In order to neglect the term proportional to ϵ_2 against the one proportional to k_r in equation (2.17) we should be able to ensure that the condition $(\epsilon_2/k_r)(v_{A\phi}^2/c_s^2) \ll 1$ is always satisfied, since both terms are proportional to $\delta\rho$. In this particular case, neglecting the forces induced by the bending of toroidal field lines becomes a progressively worse approximation the colder the disk is and is not well justified in the limit $c_s \rightarrow 0$. The case presented in equation (2.18) is even harder to justify a priori since now we would need to guarantee that the condition $(\epsilon_3/k_z)(v_{A\phi}/v_{Az})(\delta v_{Ar}/\delta v_{A\phi}) \ll 1$ is always satisfied. However, this ratio is not only proportional to $v_{A\phi}/v_{Az}$, which might not be negligible in many astrophysical contexts but, through the ratio $\delta v_{Ar}/\delta v_{A\phi}$, is also a function of k_r, k_z , and $\omega(k_r, k_z)$; the magnitude of this term is therefore unknown until we solve the problem fully. A similar situation to this one is encountered if we aim to compare the term $\epsilon_2 v_{A\phi}^2 \delta\rho$ with the term proportional to $k_z v_{Az} \delta v_{Ar}$ in equation (2.17) (see §2.5.1 for further discussion).

For the sake of consistency and in order not to impose a constraint on the magnitude of the toroidal Alfvén speed with respect to the sound speed we keep all the terms proportional to the parameters ϵ_i . We will later show that the term proportional to ϵ_1 is negligible when superthermal toroidal fields are considered.

We will also discuss under which conditions the terms proportional to ϵ_4 can be neglected and why the terms proportional to ϵ_2 and ϵ_3 are particularly important.

2.2.2 Dispersion Relation

In order to seek for non-trivial solutions of the homogeneous system of linear equations (2.16)-(2.22) we set its determinant to zero. The resulting characteristic polynomial is

$$\omega^6 + a_4\omega^4 + a_3\omega^3 + a_2\omega^2 + a_1\omega + a_0 = 0 \quad (2.25)$$

with

$$\begin{aligned} a_4 = & -\{(k_z^2 + k_r^2)(c_s^2 + v_{A\phi}^2 + v_{Az}^2) - ik_r[(2\epsilon_1 - \epsilon_2)v_{A\phi}^2 + \epsilon_4(c_s^2 + v_{Az}^2)] \\ & + k_z^2 v_{Az}^2 + \kappa^2 + \epsilon_2 \epsilon_4 v_{A\phi}^2\}, \end{aligned} \quad (2.26)$$

$$a_3 = -(2\epsilon_1 + \epsilon_3) 2k_z v_{A\phi} v_{Az}, \quad (2.27)$$

$$\begin{aligned} a_2 = & k_z^2 v_{Az}^2 [(k_z^2 + k_r^2 - \epsilon_4 ik_r)(2c_s^2 + v_{A\phi}^2 + v_{Az}^2) + ik_r(\epsilon_2 - \epsilon_3)v_{A\phi}^2] \\ & + k_z^2 \left[\kappa^2(c_s^2 + v_{A\phi}^2) + 2\epsilon_1 \epsilon_4 c_s^2 v_{A\phi}^2 + \epsilon_2 \epsilon_4 v_{A\phi}^4 + 2\frac{d \ln \Omega}{d \ln r} v_{Az}^2 + (\epsilon_2 \epsilon_4 - 2\epsilon_1 \epsilon_3) v_{A\phi}^2 v_{Az}^2 \right], \end{aligned} \quad (2.28)$$

$$a_1 = 2k_z^3 v_{A\phi} v_{Az} [(2\epsilon_1 + \epsilon_3 + \epsilon_4)c_s^2 + (\epsilon_2 + \epsilon_3)v_{A\phi}^2], \quad (2.29)$$

$$a_0 = -k_z^4 v_{Az}^2 \left[(k_z^2 + k_r^2 - \epsilon_4 ik_r) c_s^2 v_{Az}^2 + 2\frac{d \ln \Omega}{d \ln r} c_s^2 - 2\epsilon_1 \epsilon_3 c_s^2 v_{A\phi}^2 - \epsilon_2 \epsilon_3 v_{A\phi}^4 \right], \quad (2.30)$$

where we have dropped the subscript “0” in the radial logarithmic derivative of the angular frequency. This is the most general dispersion relation under our current set of assumptions. When all the parameters ϵ_i are set equal to zero, we

recover the results of previous analyses where the curvature of the toroidal field lines was not considered (e.g., Blaes & Balbus 1994; Balbus & Hawley 1998), while when they are set equal to unity we obtain our full dispersion relation.

Although the original linear system (2.16)-(2.22) related seven variables (recall that we had eliminated δP in terms of $\delta\rho$ using eq. [2.4] which is time - independent), the characteristic polynomial is only of 6th degree. This is easily understood by noting that equations (2.20) and (2.22) can be combined into one single equation expressing the solenoidal character of the perturbations in the magnetic field, $\nabla \cdot \delta \mathbf{B} = 0$. This implies a relationship between δB_r and δB_z (or equivalently between δv_{Ar} and δv_{Az}) that must be satisfied at all times and is, therefore, independent of ω . The fact that the dispersion relation (2.25) is of 6th and not of 4th degree is because we are taking into account the effects of finite compressibility. This can be seen immediately by taking the limit $c_s \rightarrow \infty$.

Once all the dimensionless variables have been properly defined, it is not evident that the magnetic-tension terms, proportional to ϵ_1 , ϵ_2 , and ϵ_3 , will play a negligible role in determining the eigenfrequencies ω . This is because the non-vanishing toroidal component of the magnetic field introduces odd powers in the dispersion relation and hence breaks its even symmetry. In fact, small modifications in the odd-power coefficients can and do have an important impact on the nature (real vs. complex) of the solutions. As we will see in §2.3 and describe in further detail in §2.4, these curvature terms introduce further coupling between the radial and toroidal directions, which in turn result in a strong coupling between the Alfvén and the slow mode.

Also important is the fact that some of the coefficients in the dispersion relation (2.25) are no longer real due to the factors ik_r . The presence of these terms does not allow us to affirm that complex roots will appear in conjugate pairs. As

we discuss in Appendix A, the terms proportional to ik_r play an important role in determining the stability of modes for which the ratio k_r/k_z is non-negligible, even in the local limit, i.e., when $k_r \gg 1$. Of course the smaller the ratio k_r/k_z , the smaller the effects of the factors ik_r will be. If we consider the limit $k_z \gg k_r$ in equation (2.25), the imaginary part of all the coefficients in the dispersion relation will become negligible. In this limiting case, whenever a given complex root is a solution of the dispersion relation (2.25) so is its complex conjugate, since the dispersion relation has real coefficients (see Appendix A).

In the next section, we will show that the dispersion relation (2.25) reduces to the dispersion relations previously derived in many local studies in different regimes. It is important to emphasize, however, that this dispersion relation fully considers the effects of compressibility and magnetic tension simultaneously without imposing any restrictions on the field strength or geometry. This feature is crucial in determining the stability properties of the MHD flow when strong toroidal fields are considered.

2.2.3 Previous Treatments

There has been some discussion in the past about the importance of the curvature terms for the stability of magnetized Keplerian flows (Knobloch, 1992; Gammie & Balbus, 1994). In studies in which these terms were considered (Knobloch, 1992; Dubrulle & Knobloch, 1993), compressibility effects were neglected. On the other hand, there have also been treatments in which compressibility was addressed but the curvature terms were neglected (Blaes & Balbus, 1994). Both types of studies provided arguments for and against the importance of these terms. The limit of cold MHD flows has been addressed by Kim & Ostriker (2000). These authors concluded that when the magnetic field strength is superthermal, the inclusion of toroidal fields tends to suppress the growth of the MRI and that for

quasi-toroidal field configurations no axisymmetric MRI takes place in the limit $c_s \rightarrow 0$.

Because of the generality of our treatment, in which both curvature terms and compressibility effects are fully taken into account, we are able to address all of these issues in §2.5. For the time being, and as a check, we can take the appropriate limits in the general dispersion relation (2.25) to recover the dispersion relations derived in the aforementioned works.

Compressibility with no field curvature — Setting $\epsilon_i = 0$, for $i = 1, 2, 3, 4$, and considering perturbations propagating only in the vertical direction (this can be formally done by taking the limit $k_z \gg k_r$ in equation [2.25]) we recover the dispersion relation derived in the compressible, weak-field limit by Blaes & Balbus (1994),

$$\begin{aligned} \omega^6 &= [k_z^2(c_s^2 + v_{A\phi}^2 + 2v_{Az}^2) + \kappa^2]\omega^4 \\ &+ k_z^2 \left[k_z^2 v_{Az}^2 (2c_s^2 + v_{A\phi}^2 + v_{Az}^2) + \kappa^2 (c_s^2 + v_{A\phi}^2) + 2 \frac{d \ln \Omega}{d \ln r} v_{Az}^2 \right] \omega^2 \\ &- k_z^4 v_{Az}^2 c_s^2 \left(k_z^2 v_{Az}^2 + 2 \frac{d \ln \Omega}{d \ln r} \right) = 0. \end{aligned} \quad (2.31)$$

The stability criterion derived from this dispersion relation is not different from the one derived, within the Boussinesq approximation, by Balbus & Hawley (1991). All the perturbations with vertical wavenumber smaller than the critical wavenumber k_{BH} are unstable, with

$$k_{BH}^2 v_{Az}^2 \equiv -2 \frac{d \ln \Omega}{d \ln r}. \quad (2.32)$$

In this case, the strength of the toroidal component of the magnetic field does not play any role in deciding which modes are subject to instabilities.

Field curvature with no compressibility — It is important to stress that even in the incompressible limit not all the terms proportional to ϵ_i in the dispersion relation

(2.25) are negligible (of course, the ones proportional to ϵ_2 are). To see that this is the case, we can take the limit $c_s \rightarrow \infty$ in the dispersion relation (2.25) to obtain

$$\begin{aligned}
& (k_z^2 + k_r^2 - ik_r \epsilon_4) \omega^4 \\
& - k_z^2 [2v_{Az}^2 (k_z^2 + k_r^2 - \epsilon_4 i k_r) + \kappa^2 + 2\epsilon_1 \epsilon_4 v_{A\phi}^2] \omega^2 \\
& - 2k_z^3 v_{A\phi} v_{Az} (2\epsilon_1 + \epsilon_3 + \epsilon_4) \omega \\
& + k_z^4 v_{Az}^2 \left[(k_z^2 + k_r^2 - \epsilon_4 i k_r) v_{Az}^2 + 2 \frac{d \ln \Omega}{d \ln r} - 2\epsilon_1 \epsilon_3 v_{A\phi}^2 \right] = 0, \quad (2.33)
\end{aligned}$$

where we have explicitly left the factors ϵ_i that should be considered as unity. This incompressible version of our dispersion relation is to be compared with the one obtained by Dubrulle & Knobloch (1993) as the local limit of the corresponding eigenvalue problem. Note that, in order to compare expression (2.33) with the dispersion relation (eq. [37]) presented in Dubrulle & Knobloch (1993), it is necessary to consider the limit $\partial v_{A\phi}/\partial r, \partial v_{Az}/\partial r \rightarrow 0$ in their equation (9). We also note that the radial wavenumber k_r appears in equation (2.33) only in the combination $k_z^2 + k_r^2 - ik_r$ while in equation (37) in Dubrulle & Knobloch (1993) we only find it as $k_z^2 + k_r^2$ (i.e., $n^2 + k^2$ in their notation). This is because when taking the local limit, $k_r \gg 1$, in the process of deriving their equation (37) from their equation (9), the terms proportional to ik_r were neglected against k_r^2 by Dubrulle & Knobloch (1993).

When the toroidal component of the magnetic field is negligible, i.e., when $v_{A\phi} \rightarrow 0$ in equation (2.33), and we consider vertical modes ($k_z \gg k_r$), we recover the dispersion relation for the incompressible MRI; the onset of unstable modes is still given by expression (2.32). For weak toroidal fields, i.e., when $v_{A\phi} \ll 1$, we can read off the small corrections to the critical wavenumber from the constant coefficient,

$$(k_z^{0i})^2 v_{Az}^2 = -2 \frac{d \ln \Omega}{d \ln r} + 2\epsilon_1 \epsilon_2 v_{A\phi}^2. \quad (2.34)$$

For stronger fields, however, the $\omega = 0$ mode is no longer unstable (see Appendix B for a general discussion on the stability of the $\omega = 0$ mode when compressibility and curvature terms are considered) and it is necessary to solve equation (2.33) in order to find the critical wavenumber for the onset of the instability. Roughly speaking, we would expect the solutions of equation (2.33) to depart significantly from the solutions to the incompressible version of the dispersion relation (2.31) when $v_{A\phi}^2 \gtrsim |d \ln \Omega / d \ln r|$, or $v_{A\phi} \gtrsim 1.2$ for a Keplerian disk. Since we are concerned here with rotationally supported configurations (i.e., $v_{A\phi} \lesssim 1$), we will not address the modifications to the mode structure caused by curvature terms in incompressible MHD flows.

It is important to stress that, for both dispersion relations (2.31) and (2.33), in the case of rotationally supported disks, the stability criterion is insensitive (or, at most, very weakly sensitive, in the incompressible case) to the magnitude of the toroidal component of the field. As we will see throughout our study, the stability criteria that emerge from equation (2.25) are significantly different from the ones discussed in this section, when we consider fields for which $v_{A\phi} > c_s$. We will also see that the term proportional to ϵ_2 , which depends on curvature and compressibility effects and is, therefore, absent from either equation (2.31) or (2.33), plays an important role in determining the mode structure in the general case.

Cold limit with no field curvature — Another limit of interest is the one corresponding to the cold, MHD, cylindrical shearing flows usually involved in the modeling of cold disk winds (i.e., far away from the disk). In this context, Kim & Ostriker (2000) addressed the behavior of the compressible axisymmetric MRI in the limit $c_s \rightarrow 0$. These authors obtained a dispersion relation considering both vertical and radial wavenumbers and derived the criterion for instability asso-

ciated with it. Their dispersion relation in the fully compressible case [eq. (57)] reads

$$\begin{aligned} & \omega^6 - [(k_z^2 + k_r^2)(c_s^2 + v_{A\phi}^2 + v_{Az}^2) + k_z^2 v_{Az}^2 + \kappa^2] \omega^4 \\ & + k_z^2 \left[(k_z^2 + k_r^2) v_{Az}^2 (2c_s^2 + v_{A\phi}^2 + v_{Az}^2) + \kappa^2 (c_s^2 + v_{A\phi}^2) + 2 \frac{d \ln \Omega}{d \ln r} v_{Az}^2 \right] \omega^2 \\ & - k_z^4 v_{Az}^2 c_s^2 \left[(k_z^2 + k_r^2) v_{Az}^2 + 2 \frac{d \ln \Omega}{d \ln r} \right] = 0. \end{aligned} \quad (2.35)$$

This dispersion relation can be obtained from equation (2.25) if we set $\epsilon_i = 0$, for $i = 1, 2, 3, 4$. Note that if we take the limit $k_z \gg k_r$ in equation (2.35) we recover equation (2.31).

For extremely cold flows we can take the limit $c_s \rightarrow 0$ in equation (2.35) to obtain

$$\begin{aligned} \omega^4 & - [(k_z^2 + k_r^2)(v_{A\phi}^2 + v_{Az}^2) + k_z^2 v_{Az}^2 + \kappa^2] \omega^2 \\ & + k_z^2 v_{Az}^2 (k_z^2 + k_r^2)(v_{A\phi}^2 + v_{Az}^2) + \kappa^2 k_z^2 v_{Az}^2 + 2 k_z^2 v_{Az}^2 \frac{d \ln \Omega}{d \ln r} = 0. \end{aligned} \quad (2.36)$$

On the other hand, taking the limit $c_s \rightarrow 0$ in equation (2.25), we obtain the more general dispersion relation

$$\begin{aligned} \omega^6 & - \{(k_z^2 + k_r^2) v_A^2 - i k_r [(2\epsilon_1 - \epsilon_2) v_{A\phi}^2 + \epsilon_4 v_{Az}^2] + k_z^2 v_{Az}^2 + \kappa^2 + \epsilon_2 \epsilon_4 v_{A\phi}^2\} \omega^4 \\ & - (2\epsilon_1 + \epsilon_3) 2 k_z v_{A\phi} v_{Az} \omega^3 + \left\{ k_z^2 v_{Az}^2 [(k_z^2 + k_r^2 - \epsilon_4 i k_r) v_A^2 + i k_r (\epsilon_2 - \epsilon_3) v_{A\phi}^2] \right. \\ & + k_z^2 \left[\kappa^2 v_{A\phi}^2 + \epsilon_2 \epsilon_4 v_{A\phi}^4 + 2 \frac{d \ln \Omega}{d \ln r} v_{Az}^2 + (\epsilon_2 \epsilon_4 - 2\epsilon_1 \epsilon_3) v_{A\phi}^2 v_{Az}^2 \right] \Big\} \omega^2 \\ & + 2 k_z^3 v_{A\phi} v_{Az} (\epsilon_2 + \epsilon_3) v_{A\phi}^2 \omega + k_z^4 v_{Az}^2 \epsilon_2 \epsilon_3 v_{A\phi}^4 = 0, \end{aligned} \quad (2.37)$$

where $v_A^2 = v_{A\phi}^2 + v_{Az}^2$. Note that in this expression, as it was also the case in the incompressible limit, several of the terms that are due to the finite curvature of the toroidal field lines are still present.

Analyzing the limit $c_s \rightarrow 0$ in the dispersion relation (2.35), Kim & Ostriker (2000) concluded that toroidal fields tend to suppress the growth of the MRI and

that, for a Keplerian rotation law, no axisymmetric MRI occurs if $i < 30^\circ$, where i is the local pitch angle of the magnetic fields defined by $i \equiv \tan^{-1}(v_{Az}/v_{A\phi})$. However, the eigenfrequencies satisfying the dispersion relations (2.25) and (2.35) in the limit $c_s \rightarrow 0$ are different and so are the criteria for instability which they are subject to. In §2.5.3, we comment in more detail on how the solutions to the dispersion relations (2.25) and (2.35) differ in the limit $c_s \rightarrow 0$ and on the implications regarding the stabilization of the MRI in cold MHD shearing flows.

In order to investigate how previous results from local stability analyses of the weak field MRI are modified as the strength of the toroidal field component increases, we will focus our attention on the stability of modes with $k_z \gg k_r$.² This approach is physically motivated, since vertical modes correspond to the most unstable modes in the well studied MRI, and is also more tractable mathematically. In the next two sections, we will perform a thorough numerical and semi-analytical study of the general dispersion relation (2.25) in the limit $k_z \gg k_r$, with particular emphasis on the case of strong toroidal fields. We will then be in a better position to understand the similarities and differences of our findings with those of the aforementioned studies and we will address them in §2.5.

2.3 Numerical Solutions

We solved numerically the dispersion relation (2.25) for the frequency ω as a function of the wavenumber k_z , employing Laguerre's root finding method (Press et al. 1992). As a typical situation of interest, we consider a Keplerian disk with $c_s = 0.05$ and $v_{Az} = 0.01$. As it will be seen from the range of values of k_z in which the various instabilities occur, the case of quasi-toroidal superthermal fields is perfectly suited to be studied in the local approximation, i.e., when $k_z \gg 1$,

²In Appendix A, we briefly describe how these results are modified when finite ratios k_r/k_z are considered. I thank Ethan Vishniac for encouraging me to address this limit.

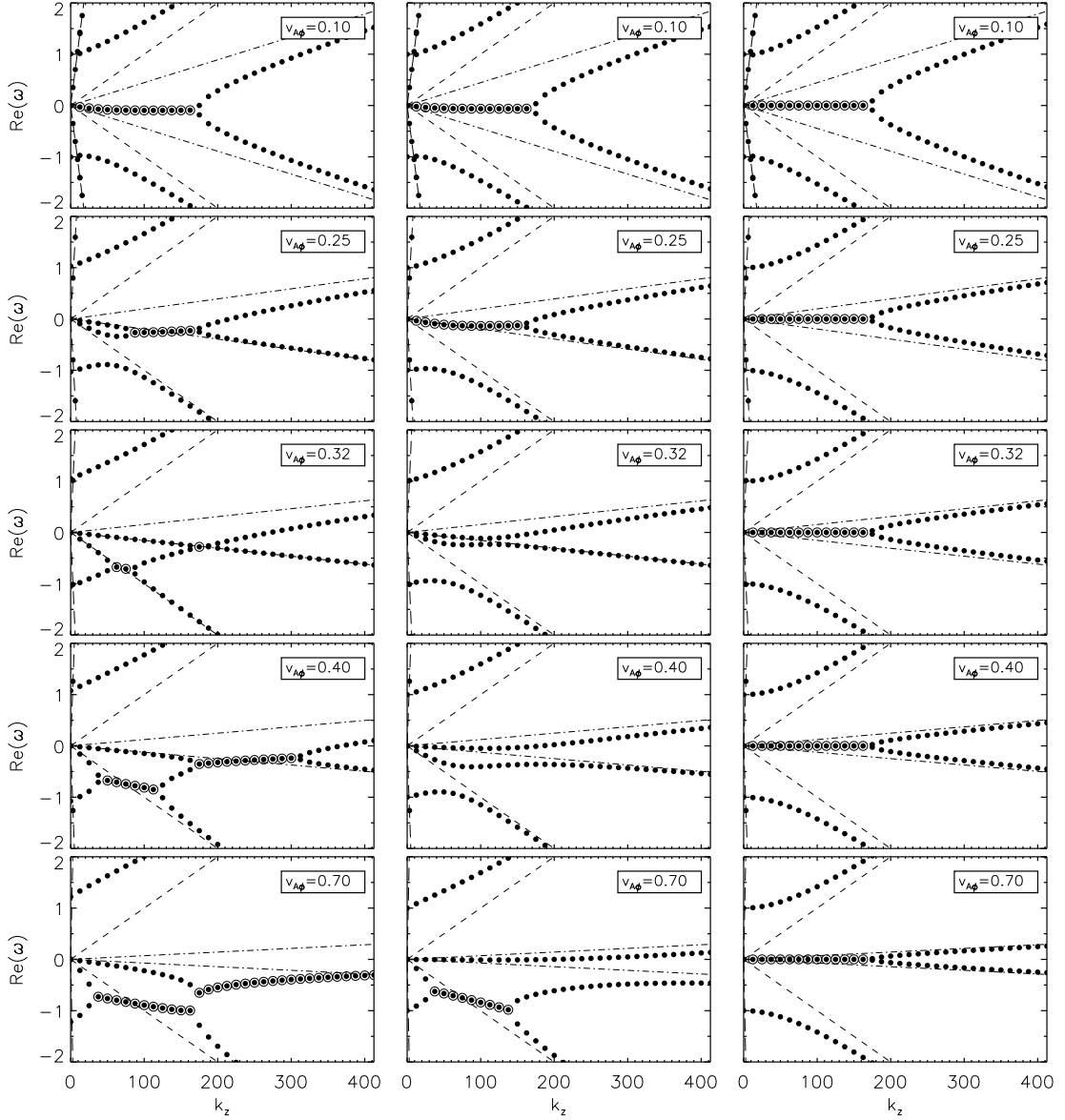


Figure 2.1 The real parts of the numerical solutions to the dispersion relation (2.25) corresponding to a Keplerian disk with $c_s = 0.05$ and $v_{Az} = 0.01$. *Left panel:* solutions to the full problem ($\epsilon_1 = \epsilon_2 = \epsilon_3 = \epsilon_4 = 1$). *Central panel:* the case in which compressibility is neglected in the curvature terms ($\epsilon_1 = \epsilon_3 = \epsilon_4 = 1$ and $\epsilon_2 = 0$). *Right panel:* the case in which all curvature terms are neglected ($\epsilon_1 = \epsilon_2 = \epsilon_3 = \epsilon_4 = 0$). Open circles indicate unstable modes (i.e., those with positive imaginary part). Long-dashed, short-dashed, and point-dashed lines show the fast, Alfvén, and slow modes, respectively, in the limit of no rotation.

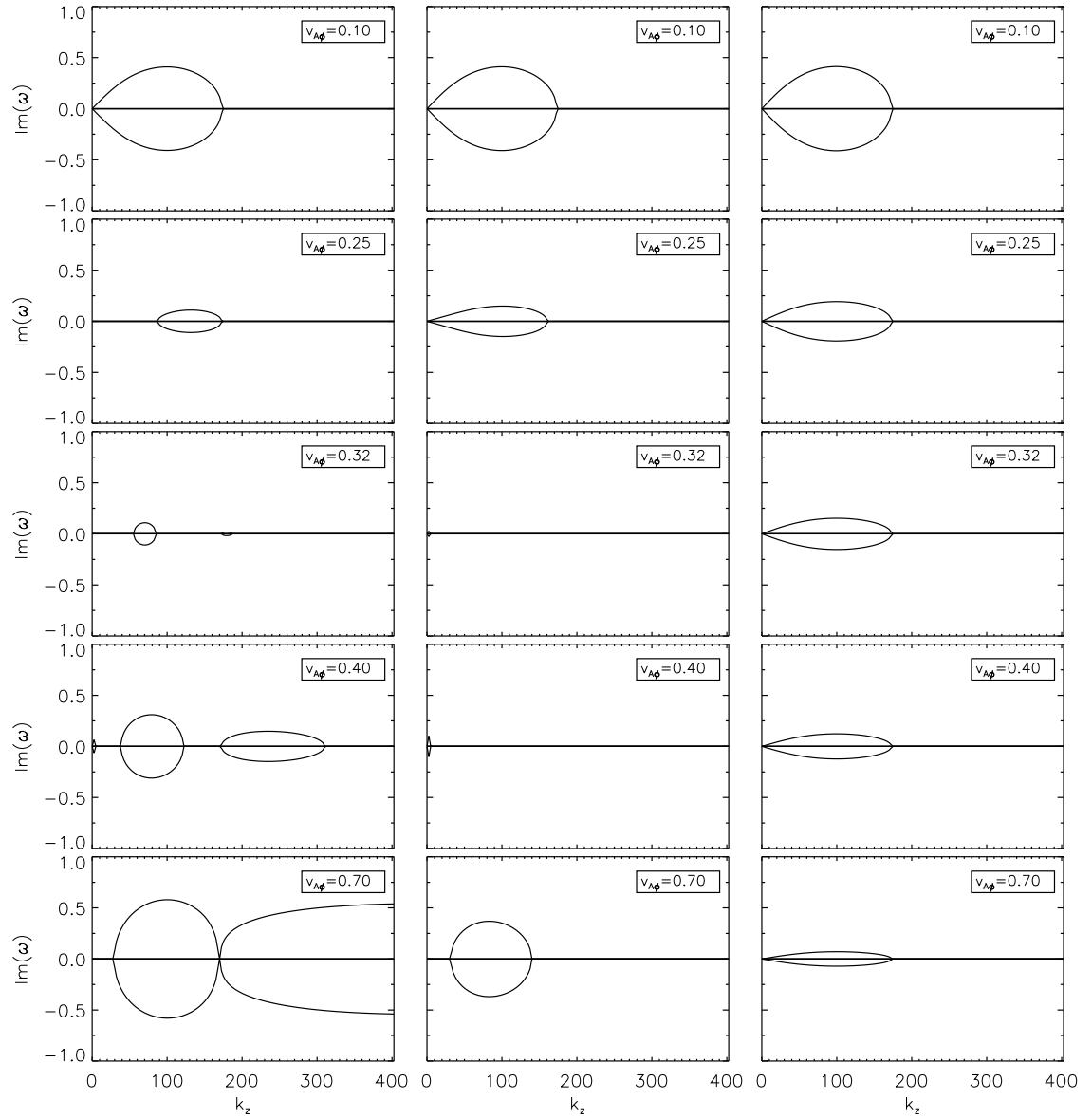


Figure 2.2 The imaginary parts for the cases discussed in Figure 2.1.

provided that the vertical component of the magnetic field is weak enough (i.e., $v_{Az} \ll 1$).

To better appreciate the effects that the curvature terms have on the stability of the modes, a set of solutions to the dispersion relation (2.25) is shown in Figures 2.1 and 2.2.³ Each of the three panels, in both figures, shows the real and imaginary parts of the solutions for different values of the toroidal field strength, parameterized by $v_{A\phi}$. The left panel shows the solutions to the full dispersion relation (2.25), i.e., when $\epsilon_1 = \epsilon_2 = \epsilon_3 = \epsilon_4 = 1$. The central panel shows the solutions to equation (2.25) when compressibility is neglected in the curvature terms, i.e., when $\epsilon_1 = \epsilon_3 = \epsilon_4 = 1$ and $\epsilon_2 = 0$. For the sake of comparison, the right panel shows the solutions to the dispersion relation (2.31), in which all curvature terms are neglected.

We first analyze Figure 2.1. When all magnetic tension terms are neglected (right panel), the qualitative structure of the normal modes of the plasma is insensitive to the magnitude of the toroidal field component (see Blaes & Balbus 1994). However, the situation is very different when the magnetic tension terms are included. For weak toroidal fields, i.e., when $v_{A\phi} \lesssim 0.1$, the solutions seem quite insensitive to the curvature terms; indeed these terms do not seem to play a significant role in altering the local stability properties of magnetized Keplerian flows compared to what is quoted elsewhere in the literature. As we will see later, for a Keplerian disk, the presence of the curvature terms is significant once $v_{A\phi}^2 \gtrsim c_s$, which in this case translates into $v_{A\phi} \gtrsim 0.22$.

For stronger toroidal fields, i.e., when $v_{A\phi} \gtrsim 0.2$, the modes with the longest wavelengths become stable when all curvature terms are included, in sharp contrast to the case in which $\epsilon_2 = 0$. For even stronger toroidal fields, i.e., when

³Some animations of the results presented in Figs. 2.1, 2.2, 2.7, and 2.8 are available at <http://www.physics.arizona.edu/~mpessah/research/>

$v_{A\phi} \gtrsim 0.3$, a second instability appears at long wavelengths, while the original instability is suppressed. When $v_{A\phi} \gtrsim 0.4$, both instabilities coexist as separate entities and the original instability reaches smaller and smaller spatial scales, when the magnitude of the toroidal field increases. For even higher toroidal fields, i.e., when $v_{A\phi} \gtrsim 0.7$, the largest unstable wavenumber of the instability that developed for $v_{A\phi} \gtrsim 0.3$ approaches k_{BH} (see eq. [2.32]). The major implication of neglecting compressibility in the curvature terms is that the original instability seems to be totally suppressed for toroidal fields larger than the ones corresponding to $v_{A\phi} \gtrsim 0.3$.

As it is clear from the dispersion relation (2.25), the presence of the toroidal component in the field introduces odd powers of the mode frequency ω and hence breaks the symmetry between positive and negative real parts of the solutions. The physical meaning of this is clear. The phase velocities of the instabilities are no longer zero and they are propagating vertically throughout the disk. This, of course, is not the case for the unstable solutions to the dispersion relation (2.31) regardless of the magnitude of $v_{A\phi}$. In that case, the most noticeable effect of an increasing toroidal field is to reduce the phase velocity of the stable modes beyond k_{BH} (which is itself independent of $v_{A\phi}$).

It is also interesting to analyze how the presence of the curvature terms modifies the growth rates of the unstable modes as a function of the toroidal magnetic field. This is shown in Figure 2.2. Again, there are no significant changes for $v_{A\phi} \lesssim 0.1$; however, quite significant modifications to the growth rates are present for $v_{A\phi} \gtrsim 0.2$. The sequence of plots in the left panel shows more clearly the suppression of the original instability, the appearance of the instability at low wavenumbers, the return of the instability at high wavenumbers, and finally the fusion of these last two. The right panel in this figure shows the effects that the

presence of a strong toroidal component has on the mode structure when curvature terms are not considered. In this case, the critical wavenumber for the onset of instabilities is not modified while there is a clear reduction in the growth rate of the non-propagating unstable modes as the magnitude of the toroidal field component increases. When the curvature terms are considered fully, the effects are more dramatic. Note also that the growth rate of the original instability is reduced faster from the first to the second plot in the left panel in Figure 2.2 with respect to their counterparts in the right panel of the same figure.

2.4 The Onset of Instabilities

2.4.1 Unstable Modes

In §2.3 we presented how the structure of the various modes evolves as a function of the toroidal field strength and noted that, for a range of field strengths, two different instabilities are clearly distinguishable. Here, we obtain the conditions (i.e., the range of wavenumbers and toroidal field strengths) for which these unstable modes are present. We start by plotting in Figure 2.3 the range of unstable wavenumbers as a function of the toroidal field strength. As a reference, we have plotted the case for a Keplerian disk. The black dots in the diagram represent the unstable vertical wavenumbers, in units of $k_z v_{Az}/c_s$, for a given toroidal Alfvén speed, in terms of $v_{A\phi}/c_s$. Three regions of unstable modes are clearly distinguishable:

- *Region I* shows the evolution of the original instability present in the top-most three plots in the left panel in Figure 2.1. This is the region where the MRI lives. Strictly speaking, the MRI is confined to the region where $v_{A\phi}/c_s \ll 1$. As we will comment in §2.4.2, instability I is no longer incompressible beyond this point. The maximum wavenumber for which

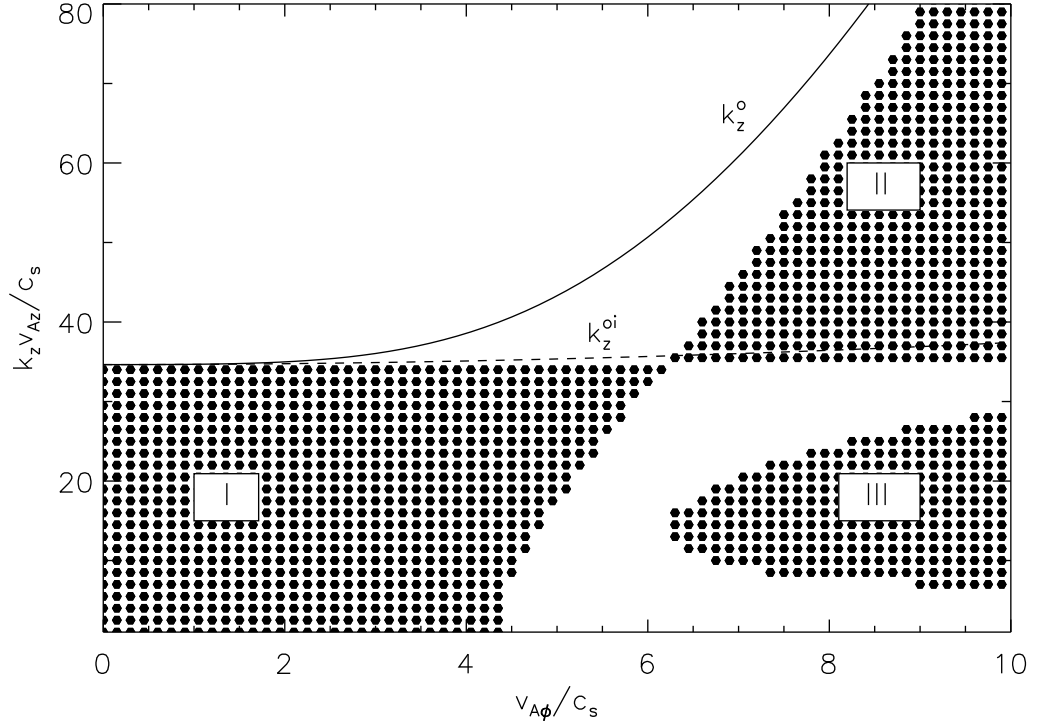


Figure 2.3 The black dots represent unstable modes obtained from solving the dispersion relation (2.25) numerically for a Keplerian disk with $c_s = 0.05$ and $v_{Az} = 0.01$. The solid (k_z^o) and dashed (k_z^{oi}) lines correspond to the critical wavenumber for which the $\omega = 0$ mode exists in the case of a compressible (see Appendix B) and an incompressible (discussed in §2.2) flow, respectively. For strong toroidal fields, compressibility plays a crucial role in the stability of the $\omega = 0$ mode. Note that, in the limit of small $v_{A\phi}/c_s$ we have $k_z^o, k_z^{oi} \rightarrow k_{BH}$, and the trivial mode becomes unstable.

this instability exists is independent of $v_{A\phi}$ and corresponds to the critical wavenumber for the onset of the MRI (i.e., k_{BH} in eq. [2.32]). The stabilization of the long-wavelength perturbations beyond a critical value of the toroidal Alfvén speed is also evident in this region. For larger toroidal field strengths, shorter and shorter wavelengths are stabilized up to the ones corresponding to k_{BH} .

- *Region II* represents the evolution of the instability that is only present for wavenumbers $k_z > k_{\text{BH}}$. Note that k_{BH} is now the minimum wavenumber for the onset of instability II. In this case, increasing $v_{A\phi}/c_s$ gives rise to unstable modes with even shorter wavelengths (two bottommost plots in the left panel of either Figure 2.1 or 2.2).
- *Region III* shows the instability that appears for intermediate wavenumbers (see for example the third plot in the left panel in Figure 2.1). Note that the shortest unstable wavelength in this region approaches k_{BH} for large values of $v_{A\phi}/c_s$ (i.e., bottommost plot in the left panel of either Figure 2.1 or 2.2).

2.4.2 Analytic Approximations

In this section we obtain analytical approximations to the dispersion relation (2.25) in various limits, which will help us identify the different critical curves in Figure 2.3.

The fast (or magnetosonic) modes are reasonably well decoupled from the rest of the oscillations (see left panels in Fig. 2.1). By studying the modes that satisfy the condition $\omega^2 \ll k_z^2 c_s^2$, we effectively eliminate the fast modes from our analysis. This can be done for strong toroidal fields because, even in the presence of rotation, the magnetosonic modes are well described by $\omega^2 \simeq k_z^2 (c_s^2 + v_A^2)$. Note that imposing $\omega^2 \ll k_z^2 c_s^2$ is a distinct and weaker condition than asking for the

MHD fluid to be incompressible ($c_s \rightarrow \infty$). By eliminating these fastest modes, it is possible to find a 4th degree dispersion relation in ω , with solutions that constitute a very good approximation to the interesting modes seen in Figures 2.1 and 2.2.

We first write the equations for the evolution of the perturbations in the magnetic field. For the sake of clarity, we present the intermediate steps with the appropriate physical dimensions but we drop the index indicating local values. Substituting equations (2.16), (2.20), and (2.22) in equation (2.19) we obtain δv_z in terms of δB_ϕ and δB_z ,

$$\delta v_z = -\frac{k_z \omega c_s^2}{(k_z c_s)^2 - \omega^2} \left[\frac{v_{A\phi}^2}{c_s^2} \frac{\delta B_\phi}{B_\phi} + \frac{\delta B_z}{B_z} \right]. \quad (2.38)$$

Using this result in equation (2.21) we find,

$$ik_z B_z \delta v_\phi = -\frac{d\Omega}{d \ln r} \delta B_r - i\omega \delta B_\phi - i\omega B_\phi \frac{(k_z c_s)^2}{(k_z c_s)^2 - \omega^2} \left[\frac{v_{A\phi}^2}{c_s^2} \frac{\delta B_\phi}{B_\phi} + \frac{\delta B_z}{B_z} \right]. \quad (2.39)$$

From equations (2.16), (2.22), and (2.38) we can recast $\delta \rho$ in terms of δB_ϕ and δB_z as

$$\frac{\delta \rho}{\rho} = -\frac{k_z^2 v_{A\phi}^2}{(k_z c_s)^2 - \omega^2} \frac{\delta B_\phi}{B_\phi} + \left[1 - \frac{(k_z c_s)^2}{(k_z c_s)^2 - \omega^2} \right] \frac{\delta B_z}{B_z}. \quad (2.40)$$

Finally, we can write equations (2.38)-(2.40) for the modes with frequencies such that $\omega^2 \ll k_z^2 c_s^2$ as,

$$\delta v_z = -\frac{\omega}{k_z} \left[\left(\frac{v_{A\phi}}{c_s} \right)^2 \frac{\delta B_\phi}{B_\phi} + i \frac{\epsilon_4}{k_z r} \frac{\delta B_r}{B_z} \right], \quad (2.41)$$

$$ik_z B_z \delta v_\phi = -\left[\frac{d\Omega}{d \ln r} - \frac{\epsilon_4}{r} \frac{\omega}{k_z} \frac{B_\phi}{B_z} \right] \delta B_r - \left[1 + \left(\frac{v_{A\phi}}{c_s} \right)^2 \right] i\omega \delta B_\phi, \quad (2.42)$$

and

$$\frac{\delta \rho}{\rho} = -\frac{v_{A\phi}^2}{c_s^2} \frac{\delta B_\phi}{B_\phi}, \quad (2.43)$$

where we have used equations (2.20) and (2.22) to recast δB_z in terms of δB_r . Note that, neglecting the factor ω^2 against $k_z^2 c_s^2$ in equation (2.38), and therefore in

equations (2.39) and (2.40), effectively reduces to neglecting the term proportional to ω in equation (2.19). Thus, for the modes of interest, the condition $\omega^2 \ll k_z^2 c_s^2$ is a statement about force balance in the vertical direction, which is made explicit in equation (2.43). In this way, we can see how important perturbations in the density are, in the presence of strong toroidal fields (see also Balbus & Hawley 1991). For $v_{A\phi} \gg c_s$, even small variations in the toroidal component of the field can have an important impact on the dynamics of the perturbations. For this reason, the assumption of an incompressible MHD flow is not valid, whenever superthermal toroidal fields are considered. Note that, in order to recover the incompressible MRI when $\epsilon_i = 0$, for $i = 1, 2, 3, 4$, we have not neglected the factor unity against $(v_{A\phi}/c_s)^2$, in equation (2.42).

We now have all the elements to write equations (2.17) and (2.18) in terms of δB_r and δB_ϕ . Using equations (2.41)-(2.43), valid in the limit $\omega^2 \ll k_z^2 c_s^2$, we obtain, in terms of the dimensionless variables,

$$\begin{aligned} -\omega^2 \delta B_r + 2i\omega \left[1 + \left(\frac{v_{A\phi}}{c_s} \right)^2 \right] \delta B_\phi = & - \left[2 \frac{d \ln \Omega}{d \ln r} + (k_z v_{Az})^2 - 2\epsilon_4 \frac{\omega}{k_z} \frac{v_{A\phi}}{v_{Az}} \right] \delta B_r \\ & - ik_z v_{A\phi} v_{Az} \left[2\epsilon_1 + \epsilon_2 \left(\frac{v_{A\phi}}{c_s} \right)^2 \right] \delta B_\phi, \end{aligned} \quad (2.44)$$

$$-\omega^2 \delta B_\phi \left[1 + \left(\frac{v_{A\phi}}{c_s} \right)^2 \right] - i\omega \left[2 + \epsilon_4 \frac{\omega}{k_z} \frac{v_{A\phi}}{v_{Az}} \right] \delta B_r = -(k_z v_{Az})^2 \delta B_\phi + ik_z v_{A\phi} v_{Az} \epsilon_3 \delta B_r. \quad (2.45)$$

These equations are the generalization of the set of equations used to illustrate the physics behind the weak-field MRI as a system of masses coupled by a spring in a differentially rotating background. Indeed, in the incompressible limit and neglecting the curvature terms proportional to ϵ_i , for $i = 1, 2, 3, 4$, we recover the set of equations presented elsewhere (Balbus & Hawley 1992, 1998).

Setting the determinant of the linear system (2.44)-(2.45) equal to zero and

taking the limit $v_{A\phi} \gg c_s$ provides the following approximate dispersion relation that is valid for strong toroidal fields⁴,

$$\begin{aligned} \omega^4 &= (\kappa^2 + k_z^2 v_{Az}^2 + \epsilon_2 \epsilon_4 v_{A\phi}^2) \omega^2 - 2k_z v_{A\phi} v_{Az} (\epsilon_2 + \epsilon_3) \omega \\ &+ k_z^2 v_{Az}^2 \left[\frac{c_s^2}{v_{A\phi}^2} \left(k_z^2 v_{Az}^2 + 2 \frac{d \ln \Omega}{d \ln r} \right) - \epsilon_2 \epsilon_3 v_{A\phi}^2 \right] = 0. \end{aligned} \quad (2.46)$$

Note that we have not neglected the factor $c_s^2/v_{A\phi}^2$ in the last term in equation (2.46) because its contribution is non-negligible at large wavenumbers. The solutions to the dispersion relation (2.46), for a Keplerian disk with $c_s = 0.05$, $v_{Az} = 0.01$, and $v_{A\phi} = 0.4$, are shown in the central panels in Figure 2.4. For the sake of comparison, the left panels in the same figure show the solutions of the full dispersion relation (2.25). The solutions to the approximate dispersion relation (2.46) are in excellent agreement with the solutions to the general dispersion relation (2.25) for which $\omega^2 \ll k_z^2 c_s^2$.

Note that the term proportional to ϵ_1 is not present in equation (2.46). This feature has important consequences for us to understand the physics behind the stability of strongly magnetized compressible flows. It has been suggested (Curry & Pudritz, 1995) that the magnetic tension term $B_\phi \delta B_\phi / r_0$ (i.e., the one proportional to ϵ_1 in eq. [2.17]) is responsible for the stabilization of long-wavelength perturbations via the restoring forces provided by strong toroidal field lines in incompressible MHD flows. This argument sounds compelling, but we can see from the last term in equation (2.44) that the term proportional to ϵ_1 is not dynamically important for compressible flows in which $v_{A\phi} \gg c_s$. At least in the radial direction, it is rather the term proportional to ϵ_2 the one governing the deviation compared to the stability properties of weak toroidal fields. This is in complete agreement with equation (2.43).

⁴Note that, had we taken the opposite limit, i.e., $c_s \gg v_{A\phi}$, we would have recovered the dispersion relation (2.33) in the limit $k_r/k_z \rightarrow 0$.

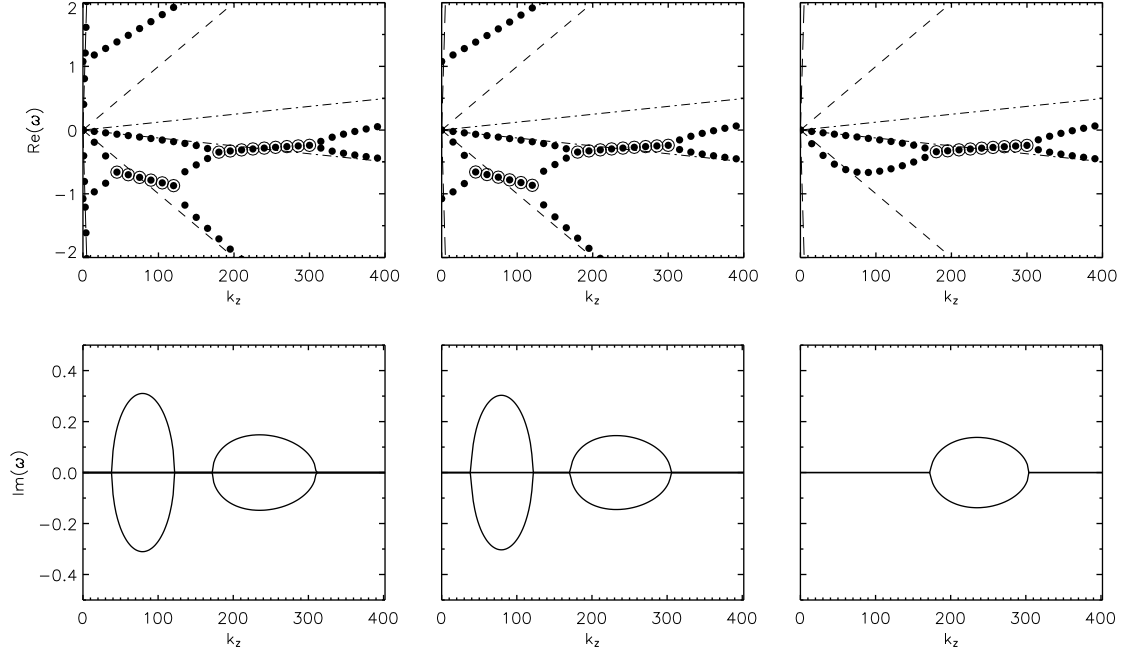


Figure 2.4 *Left panels*: Solutions to the full dispersion relation (2.25). *Central panels*: Solutions to the 4th order, approximate dispersion relation (2.46), with $\epsilon_2 = \epsilon_3 = \epsilon_4 = 1$. *Right panels*: Solutions to the 2nd order, approximate dispersion relation (2.49), with $\epsilon_2 = \epsilon_3 = 1$ and $\epsilon_4 = 0$. All solutions correspond to a Keplerian disk with $c_s = 0.05$, $v_{Az} = 0.01$, and $v_{A\phi} = 0.40$. Open circles in upper panels indicate unstable modes. Note that the phase velocities of the two instabilities (seen in either the leftmost or central upper panels and corresponding to Region II and III in §2.4.1) are similar to the phase velocities, positive and negative respectively, of the slow mode (point-dashed line) in the limit of no rotation. The fast magnetosonic modes can barely be seen close to the left axis in the upper left panel.

The dispersion relation (2.46) is of the form

$$\omega^4 + b_2\omega^2 + b_1\omega + b_0 = 0 . \quad (2.47)$$

For this 4th order equation to have complex roots (corresponding to unstable modes), its discriminant has to be negative, i.e.,

$$D_4(v_{A\phi}, k_z v_{Az}) = -4b_2^3b_1^2 - 27b_1^4 + 16b_0b_2^4 - 128b_2b_0^2 + 144b_2b_1^2b_0 + 256b_0^3 < 0 . \quad (2.48)$$

The modes satisfying this condition are shown as black dots in Figure 2.5. This analytical criterion agrees well with the numerical results for most of the parameter space $(v_{A\phi}/c_s, k_z v_{Az}/c_s)$ with the exception of some of the unstable modes close to the separatrix of the Regions I and II, defined in §2.4.1.

Limiting wavenumbers for Regions I and II.— The modes satisfying the condition $D_4 = 0$ correspond to the limits of Regions I, II, and III in Figure 2.5. Their analytical expressions, however, are complicated. More progress can be made by realizing that the solutions to the second order equation obtained by simply dropping the ω^4 term in equation (2.46),

$$\begin{aligned} (\kappa^2 + k_z^2 v_{Az}^2 + \epsilon_2 \epsilon_4 v_{A\phi}^2) \omega^2 &+ 2k_z v_{A\phi} v_{Az} (\epsilon_2 + \epsilon_3) \omega \\ &- k_z^2 v_{Az}^2 \left[\frac{c_s^2}{v_{A\phi}^2} \left(k_z^2 v_{Az}^2 + 2 \frac{d \ln \Omega}{d \ln r} \right) - \epsilon_2 \epsilon_3 v_{A\phi}^2 \right] = 0 , \end{aligned} \quad (2.49)$$

constitute a very good approximation to the solutions of the dispersion relation (2.25) whenever the frequencies of the modes satisfy $\omega^2 \ll 1$. This can be appreciated by comparing the left and right panels in Figure 2.4. The physics behind this approximation is not as direct as the physics behind the condition $\omega^2 \ll k_z^2 c_s^2$, but it can also be understood in terms of force balance, this time in the radial direction. The dispersion relation (2.49) can be obtained by neglecting the term proportional to ω^2 in equation (2.44), setting to zero the determinant of the resulting

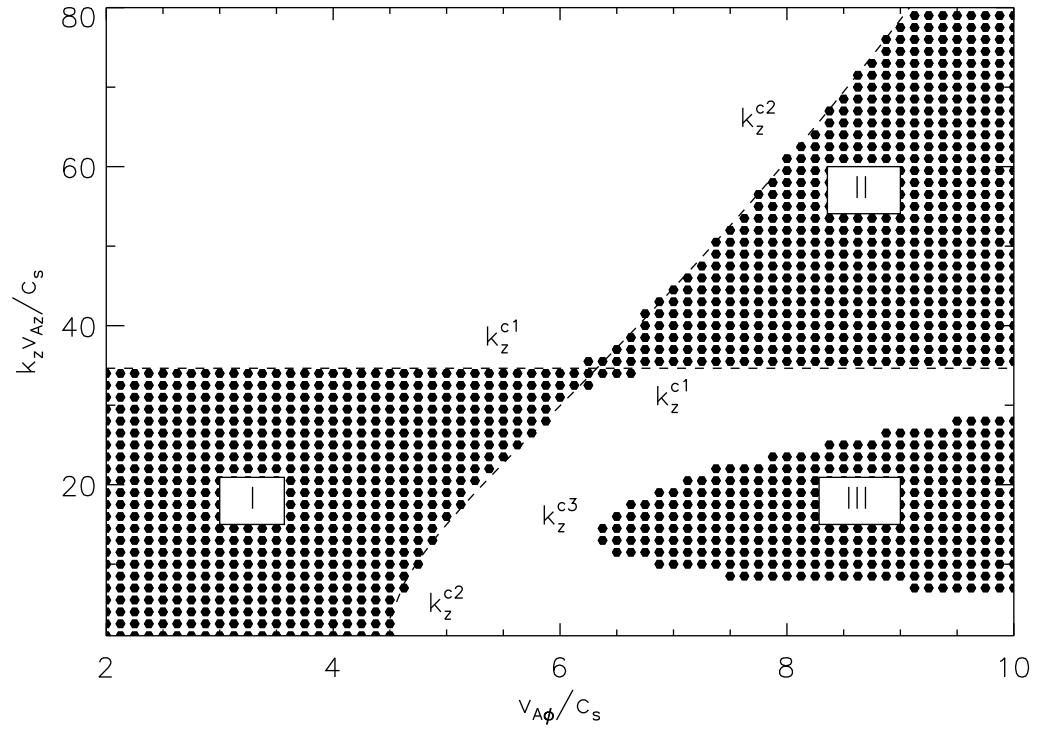


Figure 2.5 The black dots represent unstable modes satisfying the approximate instability criteria (2.48), described in §2.4.2. The dashed lines, labeled by k_z^{c1} and k_z^{c2} , are the limits of Regions I and II obtained analytically, also in §2.4.2. The onset of instability III is labeled by k_z^{c3} . As in Figure 2.3, we have assumed a Keplerian disk with $c_s = 0.05$ and $v_{Az} = 0.01$.

linear system given by equations (2.44)-(2.45) and taking the limit $v_{A\phi} \gg c_s$. This approximation is equivalent to neglecting the term proportional to ω in equation (2.17) and hence related to neglecting the radial acceleration experienced by a displaced fluid element.

Setting the discriminant of equation (2.49) to zero, gives an equation in k_z with solutions that are the limiting wavenumbers for the onset of instabilities I and II in Figure 2.5, i.e.,

$$D_2(v_{A\phi}, k_z v_{Az}) = (k_z v_{Az})^4 + \left[\kappa^2 + 2 \frac{d \ln \Omega}{d \ln r} - v_{A\phi}^2 \left(\frac{v_{A\phi}^2}{c_s^2} - \epsilon_4 \frac{c_s^2}{v_{A\phi}^2} \right) \right] (k_z v_{Az})^2 + 2 \frac{d \ln \Omega}{d \ln r} \left[\kappa^2 - v_{A\phi}^2 \left(\frac{v_{A\phi}^2}{c_s^2} - \epsilon_4 \frac{c_s^2}{v_{A\phi}^2} \right) \right] - \epsilon_4 v_{A\phi}^4 = 0. \quad (2.50)$$

Here, we have set $\epsilon_2 = \epsilon_3 = 1$ but have explicitly left ϵ_4 to show that its contribution to the onset of instabilities I and II is not important when $v_{A\phi} \gg c_s$, as long as we are considering a rotationally supported disk. We mention, however, that the numerical solutions show that the contribution of the term proportional to ϵ_4 is small but not negligible for the unstable modes in region III. Neglecting the terms proportional to ϵ_4 , the solutions to equation (2.50) are simply

$$(k_z^c v_{Az})^2 = \frac{1}{2} \left[\frac{v_{A\phi}^4}{c_s^2} - \left(\kappa^2 + 2 \frac{d \ln \Omega}{d \ln r} \right) \right] \pm \frac{1}{2} \left| \frac{v_{A\phi}^4}{c_s^2} - 4 \right|. \quad (2.51)$$

One of these solutions always coincides with k_{BH} (eq. [2.32]),

$$(k_z^{c1} v_{Az})^2 = -2 \frac{d \ln \Omega}{d \ln r}, \quad (2.52)$$

and the other one is

$$(k_z^{c2} v_{Az})^2 = \frac{v_{A\phi}^4}{c_s^2} - \kappa^2. \quad (2.53)$$

The modes with wavenumbers in the range $[\min(k_z^{c1}, k_z^{c2}), \max(k_z^{c1}, k_z^{c2})]$ are unstable. In Figure 2.5, the critical curves $k_z^{c1}(v_{A\phi})$ and $k_z^{c2}(v_{A\phi})$ are shown, with

the proper normalization, as dashed lines. The critical wavenumber k_z^{c2} in equation (2.53) will be positive only for toroidal Alfvén speeds larger than

$$v_{A\phi}^I = \sqrt{\kappa c_s} . \quad (2.54)$$

This is the critical value of the Alfvén speed beyond which the modes with longest wavelength in Region I (see Fig. 2.5) begin to be stable. For a Keplerian disk, the epicyclic frequency coincides with the orbital frequency and thus, in dimensionless units, $\kappa^2 = 1$. In this case, the critical Alfvén speed for k_z^{c2} to be positive corresponds to $v_{A\phi} = 0.223$. This is the reason for which the long-wavelength modes are already stable in the second plot in the left panel in Figure 2.1, where $v_{A\phi} = 0.25$.

Incidentally, we find that the values of toroidal Alfvén speeds for which the standard MRI gives the appropriate range of unstable modes are not restricted to $v_{A\phi} \ll c_s$ but rather to $v_{A\phi} \ll \sqrt{\kappa c_s}$. For $v_{A\phi} \gtrsim \sqrt{\kappa c_s}$, the standard MRI is stabilized at low wavenumbers. We point out that, Papaloizou & Szuszkiewicz (1992) found, by means of a global stability analysis of a compressible flow, that for a slim disk threaded only by a vertical field, the flow is stable if the vertical Alfvén speed exceeds, within a factor of order unity, the geometrical mean of the sound speed and the rotational speed. In dimensionless units, this stability criterion translates into $v_{Az} \gtrsim \sqrt{c_s}$.

The limiting case in which $k_z^{c1} = k_z^{c2}$, is reached for

$$v_{A\phi}^{II} = \sqrt{2c_s} . \quad (2.55)$$

Note that, for $c_s = 0.05$, this corresponds to a value for the critical toroidal Alfvén speed of $v_{A\phi} = 0.316$. This situation is to be compared with the mode structure in the third plot in the left panel in Figure 2.1, where $v_{A\phi} = 0.32$.

Limiting wavenumbers for Region III.— In the previous section we presented some useful analytical approximations to describe the dependence of the critical values of the toroidal Alfvén speeds and wavenumbers defining Regions I and II on the different quantities characterizing the MHD flow. We could not, however, find simple analytical expressions to describe satisfactorily the corresponding behavior of the critical values defining Region III. We will describe next how the different unstable regions in Figure 2.3 depend on the magnitude of the sound speed and the steepness of the rotation profile.

2.5 Discussion

In this section, we address several issues related to the importance of the curvature terms in determining the stability criteria obeyed by the solutions to the dispersion relation (2.25). We comment on some controversies raised by previous investigations that have treated the standard MRI taking into account, in various ways, either compressibility or curvature of the background magnetic field. We also comment on the importance in the outcome of the instabilities played by the magnetic tension produced by toroidal field lines in the limit of cold MHD flows. We highlight the similarities and differences of our findings with the results of Curry & Pudritz (1995), who also found the emergence of a new (but different) instability for strong toroidal fields in the case of an incompressible MHD flow. Finally, we address the potential implications of our findings for shearing box models in which magnetic tension terms, induced by the curvature of the background field, are not considered.

2.5.1 Importance of Curvature Terms

In section §2.2 we mentioned that the terms proportional to ϵ_i , for $i = 1, 2, 3, 4$, are usually neglected in local stability analyses due to their $1/r_0$ dependence. Some

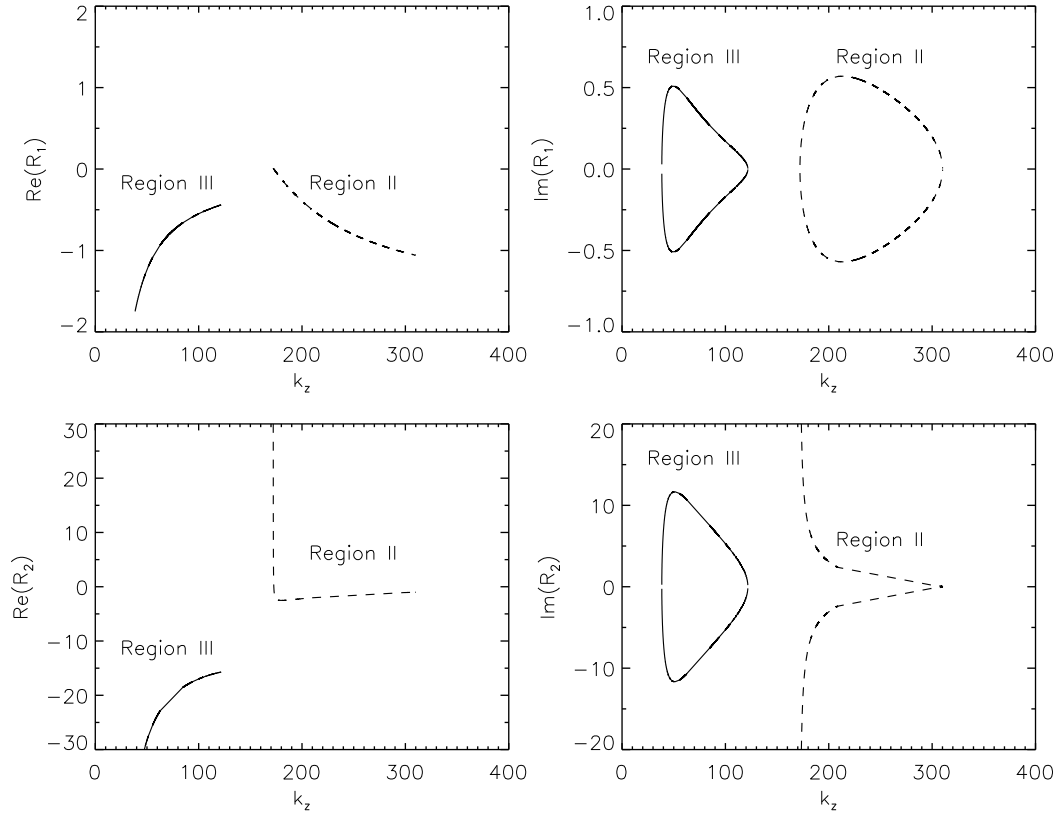


Figure 2.6 The importance of the curvature terms proportional to ϵ_2 and ϵ_3 , as defined by the ratios R_1 (eq. [2.57]) and R_2 (eq. [2.58]). For illustrative purposes, we have considered a Keplerian disk with $c_s = 0.05$, $v_{Az} = 0.01$, and $v_{A\phi} = 0.4$.

of these terms, however, are also proportional to the magnitude of the toroidal field. In this chapter, we found that, when strong toroidal fields are considered, these terms led to substantial modifications to the stability criteria of MHD modes known to be valid in the limit of weak fields. After solving the full problem, we are in a better position to understand why this is the case.

To illustrate the point, consider the ratio of the term proportional to k_z to the one proportional to ϵ_2 in equation (2.17) and the ratio of the term proportional to k_z to the one proportional to ϵ_3 in equation (2.18), i.e.,

$$R_1 \equiv \frac{\epsilon_2}{ik_z} \frac{v_{A\phi}^2}{v_{Az}} \frac{\delta\rho}{\delta v_{Ar}} \quad \text{and} \quad R_2 \equiv \frac{\epsilon_3}{ik_z} \frac{v_{A\phi}}{v_{Az}} \frac{\delta v_{Ar}}{\delta v_{A\phi}}. \quad (2.56)$$

In order to ensure that the contributions due to curvature are negligible in a local analysis regardless of the magnitude of the toroidal field component, we should be able to ensure that the conditions $R_1 \ll 1$ and $R_2 \ll 1$ hold in the limit of large k_z for any value of $v_{A\phi} \lesssim 1$. While it is encouraging that both dimensionless ratios are proportional to $1/k_z$, they are also proportional to the ratio of perturbed quantities, which we do not know *a priori*. It is only after having found the eigenfrequencies $\omega(k_z)$ by taking into account all the curvature terms that we can properly address this issue.

We can calculate how the ratios R_1 and R_2 depend on the wavenumber k_z as follows. The ratio R_1 can be recast using equations (2.43) and (2.44) as

$$R_1 = \frac{\epsilon_2}{k_z} \frac{v_{A\phi}}{v_{Az}} \left(\frac{v_{A\phi}}{c_s} \right)^2 \frac{\omega^2 - \left(2 \frac{d \ln \Omega}{d \ln r} + k_z^2 v_{Az}^2 - 2 \epsilon_4 \frac{\omega}{k_z} \frac{v_{A\phi}}{v_{Az}} \right)}{2\omega \left[1 + \left(\frac{v_{A\phi}}{c_s} \right)^2 \right] + k_z v_{Az} v_{A\phi} \left[2\epsilon_1 + \epsilon_2 \left(\frac{v_{A\phi}}{c_s} \right)^2 \right]}. \quad (2.57)$$

In a similar way, we can rewrite the ratio R_2 using equation (2.45) as

$$R_2 = \frac{\epsilon_3}{k_z} \frac{v_{A\phi}}{v_{Az}} \frac{\omega^2 \left[1 + \left(\frac{v_{A\phi}}{c_s} \right)^2 \right] - k_z^2 v_{Az}^2}{\omega \left[2 + \epsilon_4 \frac{\omega}{k_z} \frac{v_{A\phi}}{v_{Az}} \right] + \epsilon_3 k_z v_{Az} v_{A\phi}}. \quad (2.58)$$

For the sake of simplicity, let us consider a given value for the toroidal Alfvén speed, e.g., $v_{A\phi} = 0.4$. Figure 2.6 shows the dependence of the ratios R_1 and R_2 on wavenumber for the unstable modes. The eigenfrequencies $\omega(k_z)$ were obtained by solving equation (2.25) with $\epsilon_i = 1$, for $i = 1, 2, 3, 4$, considering a Keplerian disk with $c_s = 0.05$ and $v_{Az} = 0.01$. The ratios R_1 and R_2 for the unstable modes (with $v_{A\phi} = 8c_s$) in Regions II and III in Figure 2.3 are clearly identified. The complete mode structure corresponding to this case can be seen in the left panels of Figure 2.4.

It is important to stress that neither the real nor the imaginary parts of either R_1 or R_2 are negligible compared to unity even for Alfvén speeds of order a few times the sound speed. In fact, for the unstable modes, the ratio R_1 is of order unity and the ratio R_2 is in some cases larger than one by one order of magnitude. Their functional form is significantly different than the assumed $1/k_z$.

2.5.2 Magnetorotational Instabilities with Superthermal Fields

In §2.3 we demonstrated that, when the toroidal magnetic field in a differentially rotating MHD flow becomes superthermal, three distinct instabilities can be identified, which we denote by roman numerals I, II, and III in Figure 2.3. We summarize the qualitative characteristics of these instabilities below.

In contrast to the weak-field MRI, all three instabilities correspond to compressible MHD modes. Moreover, while the traditional MRI corresponds to perturbations with negligible displacements along the vertical direction, this is not true for any of the three instabilities with superthermal toroidal fields. Instead, vertical displacements are an important characteristic of these instabilities and they occur with negligible acceleration, under a force balance between thermal and magnetic pressure. Finally, as in the case of the MRI, there is no significant acceleration along the radial direction but rather a force balance between mag-

netic tension, magnetic pressure, and thermal pressure.

In Figures 2.7 and 2.8 we study numerically the dependences of the three instabilities on the properties of the background flow. As also shown in the case of the weak-field MRI (Balbus & Hawley, 1991), instability I occurs only in differentially rotating flows, with radially decreasing angular velocity. However, instability I also requires the presence of a non-negligible thermal pressure. Either a radially increasing angular velocity or a superthermal toroidal field can suppress instability I and hence the traditional MRI.

Instability II is ubiquitous, whenever the background toroidal field of the flow is significantly superthermal. Indeed, it occurs even for flat rotation profiles (see Fig. 2.7) or very cold (see Fig. 2.8) flows. In a sense opposite to instability I, the steepness of the rotational profile determines the minimum unstable wavenumber, whereas the magnitude of the sound speed determines the minimum toroidal field strength required for the instability to occur. This instability seems to correspond to a generalization of the axisymmetric toroidal buoyancy (ATB) mode identified in Kim & Ostriker (2000), where the case $c_s = 0$ was studied. In a similar way to instability II, the ATB modes with $c_s = 0$ become unstable for all wavenumbers exceeding a critical value (for vertical modes this value is just given by k_{BH}). When a finite sound speed is considered, however, thermal effects play an important role at small scales by completely stabilizing all the modes with wavenumbers larger than k_z^{c2} (eq. [2.53]).

Finally, instability III depends strongly on the rotational profile but very weakly on the sound speed. For rotationally supported flows (i.e., for $v_{\text{A}\phi} \ll 1$), instability III occurs only for significantly steep rotational profiles, e.g., $q = |d \ln \Omega / d \ln r| \gtrsim 1.0$, for the parameters depicted in Figure 2.7.

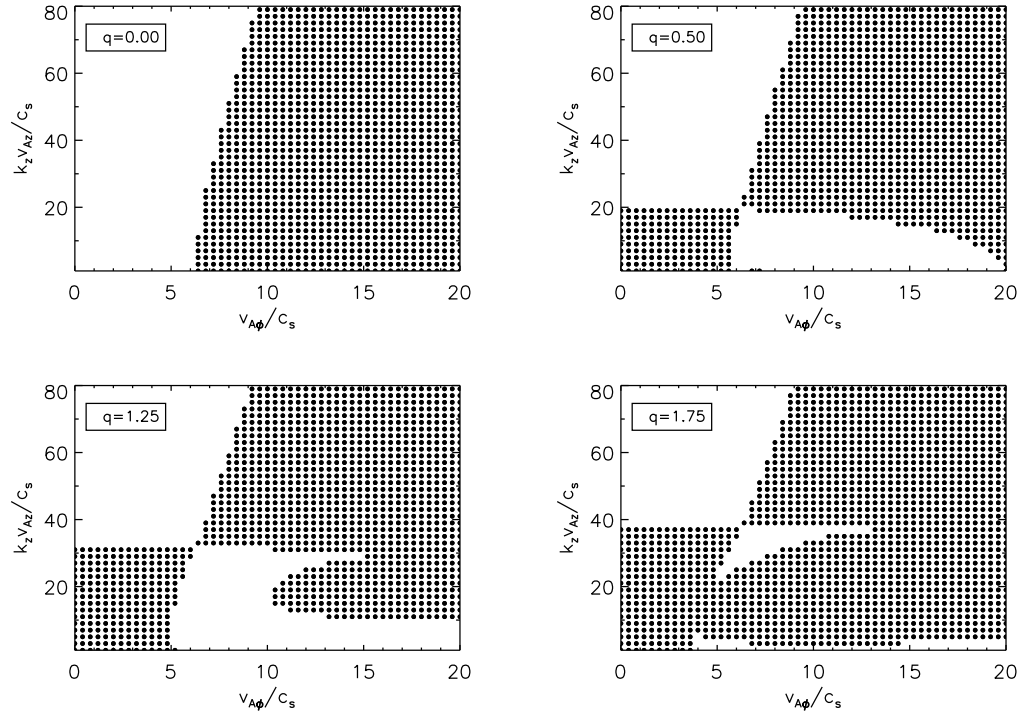


Figure 2.7 The black dots represent unstable modes obtained from solving numerically the dispersion relation (2.25) as a function of the toroidal Alfvén speed. As an example, we have assumed $c_s = 0.05$ and $v_{Az} = 0.01$. In each plot, we consider different values of the rotational profile, $q = -d \ln \Omega / d \ln r$. Note that, the highest value of the local toroidal Alfvén speed considered here corresponds to the local circular velocity.

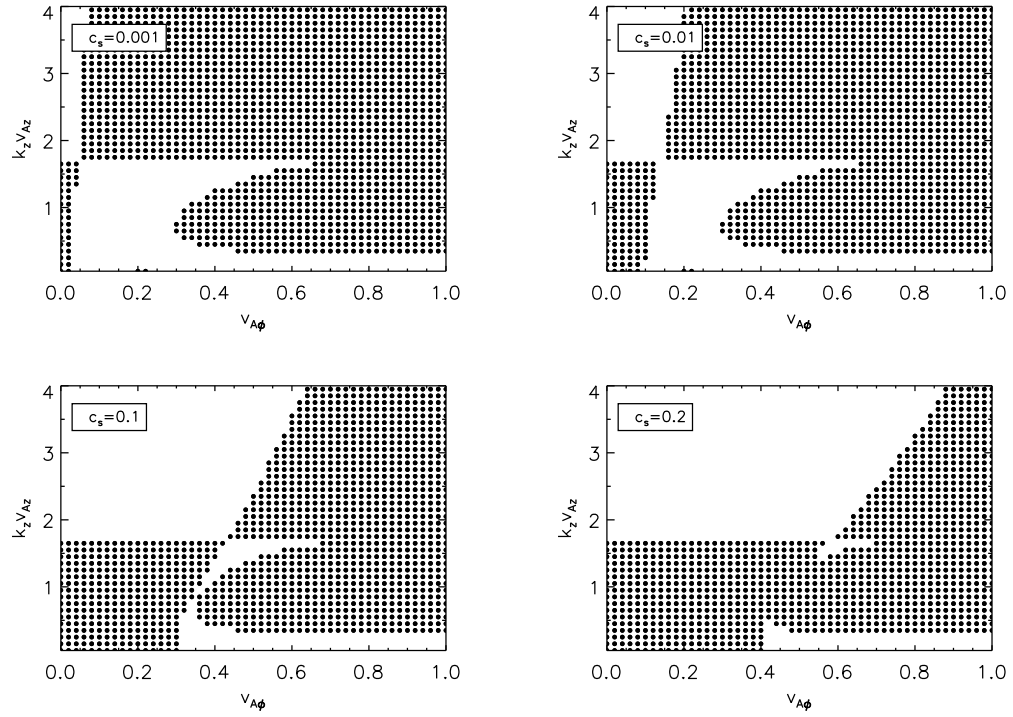


Figure 2.8 The black dots represent unstable modes obtained from solving the dispersion relation (2.25) numerically, for a Keplerian disk with $v_{Az} = 0.01$. In each plot, different values of the local sound speed, c_s , are considered. Note that in this case, the axes are not normalized by the particular value of the local sound speed, but rather by our initial choice of dimensionless variables, see §2.2.

2.5.3 Comparison to Previous Analytical Studies

Soon after the original paper by Balbus & Hawley (1991), Knobloch (1992) critiqued their approach to the study of local instabilities for lacking the contributions of curvature terms. Knobloch (1992) formulated the stability analysis of a vertically unstratified, incompressible disk as an eigenvalue problem in the radial coordinate. He found that the presence of a toroidal field component changes the conditions for the presence of the instability as well as the character of the unstable modes from purely exponentials to overstable (i.e., $Re[\omega] \neq 0$). Gammie & Balbus (1994) argued against Knobloch's findings regarding overstability, stating that it arose as a consequence of having kept only small order terms (like v_A/c_s and $v_A/\Omega_0 r_0$). They concluded that these contributions would have been negligible had the flow been considered compressible.

As we comment in §2.4.2, Knobloch's dispersion relation is correct even in the limit $c_s \gg v_{A\phi}$ (i.e., without the necessity of imposing strict incompressibility). Formally speaking, the linear term in ω in equation (2.33) does break the symmetry of the problem allowing for unstable modes with $Re(\omega) \neq 0$. But it is also the case that, in the limit $c_s \gg v_{A\phi}$, because of the relative magnitude of the coefficients in the dispersion relation (2.33), we do not expect the stability properties of the flow to differ greatly from those described by the incompressible MRI. As we mention in §2.2.3, in order to see significant differences, the Alfvén speed would have to be of the order of the circular speed and therefore we do not expect the curvature terms to play a significant role on the stability of incompressible, rotationally supported flows. On the other hand, if we allow the MHD fluid to be compressible and consider the curvature of the background flow, the mode structure can be radically different from what is expected for the compressible MRI (c.f. Blaes & Balbus 1994). This is the case, even if the toroidal Alfvén speed ex-

ceeds the sound speed by a factor of a few without the necessity of violating the condition of a rotationally supported disk (see Fig. 2.1).

The stability of axisymmetric perturbations in weakly ionized and weakly magnetized shear flows was considered by Blaes & Balbus (1994). They showed that, when ionization equilibrium is considered in the two-fluid approach, strong toroidal fields can fully stabilize the flow. As part of their study, they relaxed the Boussinesq approximation in the case of a single fluid and argued that, to all orders in the field strength, the magnitude of B_ϕ does not affect the stability criterion. As noted by Curry & Pudritz (1995), this conclusion was reached because the terms proportional to B_ϕ/r_0 were not included in the local analysis.

The behavior of the MRI in cold MHD shearing flows, has been addressed by Kim & Ostriker (2000). When performing their local analysis, these authors obtained the compressible version of the standard dispersion relation for the MRI and studied its solutions for different values of the ratio c_s^2/v_A^2 . Analyzing their dispersion relation (i.e., their equation [57] which is equivalent to equation [2.35] in this study), Kim & Ostriker (2000) concluded that, when the magnetic field is superthermal, the inclusion of a toroidal component suppresses the growth rate of the MRI. Moreover, they found that, for a Keplerian rotation law, no axisymmetric MRI takes place in very cold MHD flows if $i < 30^\circ$, where i is the pitch angle of the local magnetic fields, $i \equiv \tan^{-1}(v_{Az}/v_{A\phi})$.

In §2.4 we showed that, depending on the strength of the toroidal field component, accounting for the finite curvature of the background magnetic field and the finite compressibility of the flow could be crucial in establishing which modes are subject to instabilities. In particular, we stated that both effects should be considered simultaneously whenever the local value of the toroidal Alfvén speed exceeds the geometric mean of the local sound speed and the local rotational speed

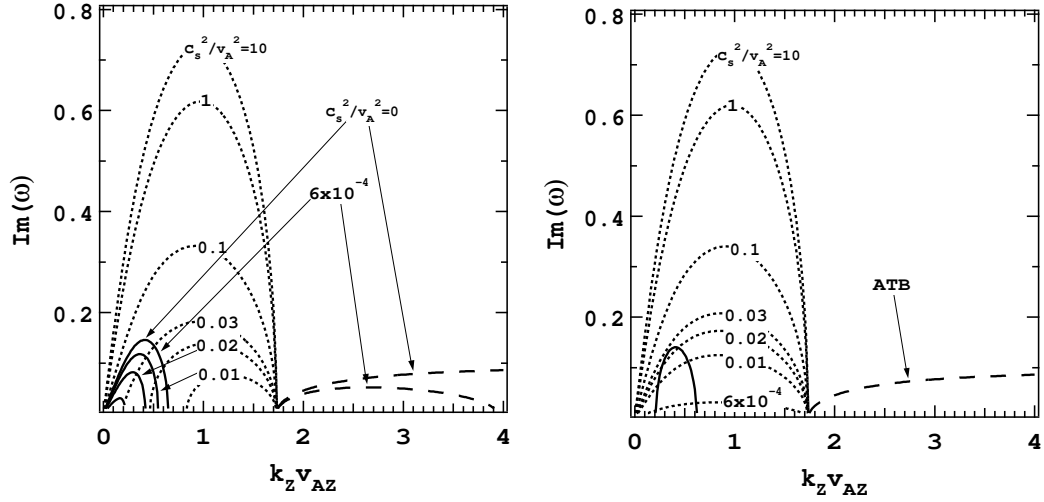


Figure 2.9 The growth rate evolution of the different instabilities defined in §2.4.1 for increasing magnetic field strength parameterized in terms of the ratio c_s^2/v_A^2 for a fixed pitch angle $i \equiv \tan^{-1}(v_{Az}/v_{A\phi}) = 25^\circ$. *Left panels:* Growth rates of the unstable solutions to the full dispersion relation (2.25), when all curvature terms are taken into account. *Right panels:* Growth rates of the unstable solutions to the dispersion relation (2.35), i.e., when all curvature terms are neglected. In both cases, we have considered a vanishing ratio k_r/k_z , $v_{Az} = 0.05$, and a Keplerian disk. The dotted lines, in both panels, show the stabilization of the standard MRI as the magnetic field becomes superthermal (instability I). The solid and dashed lines on the left panel show the growth rates corresponding to instability III and II respectively. As discussed in §2.3, these instabilities do not have a counterpart when the magnetic tension induced by bending of toroidal field lines is neglected. For completeness we have included, in the right panel, with solid and dashed lines the unstable solutions to equation (44) in Kim & Ostriker (2000). Instability II corresponds to a generalization of the ATB mode when thermal effects are accounted for.

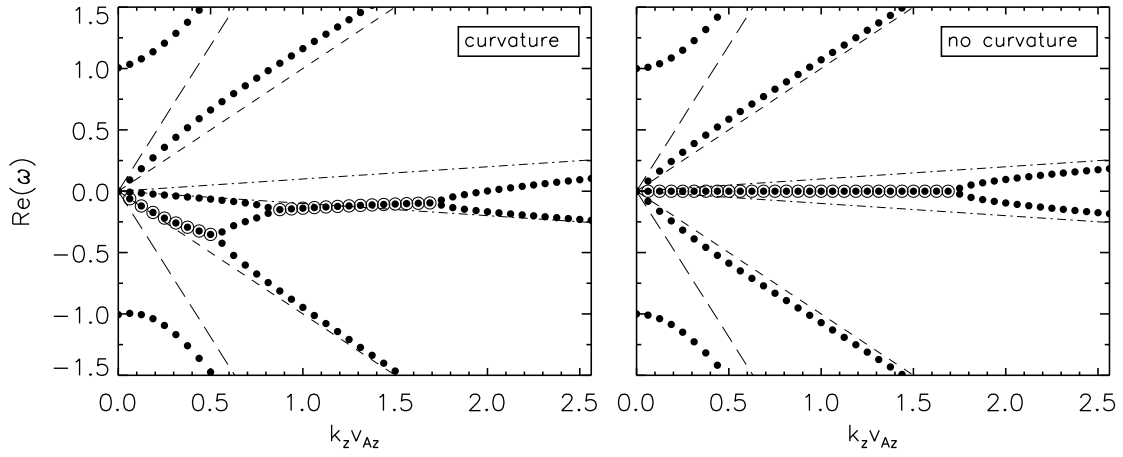


Figure 2.10 The real parts of the solutions to the dispersion relation (2.25) corresponding to $c_s^2/v_A^2 = 0.01$ for a pitch angle $i = \tan^{-1}(v_{Az}/v_{A\phi}) = 25^\circ$, a vanishing ratio k_r/k_z , $v_{Az} = 0.05$, and a Keplerian disk. *Left panel:* Solutions to the full dispersion relation (2.25), when all curvature terms are taken into account. *Right panel:* Solutions to the dispersion relation (2.31), i.e., when all curvature terms are neglected. Open circles indicate unstable modes. In both cases, the unstable modes with the shortest wavelength correspond to $k_{BH}v_{Az}$.

(for a Keplerian disk). However, this analytic criterion was found to be relevant for the modes with frequencies satisfying the condition $\omega^2 \ll k_z^2 c_s^2$. Therefore, it is not obvious that we can trust this criterion in the limit $c_s \rightarrow 0$.

In order to see whether finite curvature effects do play a role in the stability of cold MHD flows we solved the complete dispersion relation (2.25) for a pitch angle $i = 25^\circ$ and considered different values for the ratio c_s^2/v_A^2 . Figure 2.9 shows the growth rates for the unstable modes of our dispersion relation (i.e., eq. [2.25]) and compares them to the ones of the dispersion relation obtained when the curvature terms are neglected (i.e., eq. [2.35]). In both cases, we have considered $k_z \gg k_r$, $v_{Az} = 0.05$, and a Keplerian disk. The stabilization of the standard MRI (i.e., instability I) as the magnetic field becomes superthermal ($v_A > c_s$) is evident (dotted lines in both panels). When the effects of magnetic tension are considered, not only does the growth rate of the MRI decrease faster for low values of c_s^2/v_A^2 but the modes with longest wavelengths are no longer unstable (e.g. when $c_s^2/v_A^2 = 0.01$). Because of this, the MRI is completely stabilized even for finite values of c_s^2/v_A^2 . In contrast, when the curvature of the field lines is neglected, the growth rates decrease but the range of unstable modes remains unchanged as $c_s \rightarrow 0$ (right panel in Figure 2.9); it is only when $c_s = 0$ that the MRI is completely suppressed. For completeness, we present in Figure 2.10 the real parts of the solutions to the dispersion relation (2.25) for $i = 25^\circ$, $k_z \gg k_r$, $v_{Az} = 0.05$, $c_s^2/v_A^2 = 0.01$ and a Keplerian disk, in the cases where curvature terms are considered (left panel) and neglected (right panel). The stabilization of the MRI at low wavenumbers and the emergence of instability III are evident. Note that, from Figure 2.10, it is clear that the inclusion of magnetic tension terms can cause modifications to the mode structure when $v_A \gg c_s$, even when the toroidal and vertical components of the magnetic field are comparable.

In §2.5.2 we mentioned that instability II seems to be a generalization of the axisymmetric toroidal buoyancy (ATB) modes, identified by Kim & Ostriker (2000), that accounts for finite temperature effects. Further indication that this is indeed the case can be found in Figure 2.9 where we have plotted (dashed lines) the growth rates corresponding to instability II and the one corresponding to the ATB mode (solutions of equation [44] with $\omega^2 \ll k_z^2 v_A^2$ in Kim & Ostriker 2000). Although finite compressibility suppresses instability II at large wavenumbers, it is clear that, as $c_s \rightarrow 0$, the growth rates associated with instability II tend continuously to the growth rate of the cold ATB mode. For completeness, we have also included, in the right panel of Figure 2.9, the growth rate corresponding to the remaining unstable solution of equation (44) in Kim & Ostriker (2000) (solid line). This growth rate should be interpreted with great care since the aforementioned equation was derived under the condition $\omega^2 \ll k_z^2 v_A^2$, which is not satisfied by the corresponding unstable mode. Nonetheless, we have included it to show the similarities that it shares with the growth rates corresponding to instability III (solid lines in the left panel) as $c_s \rightarrow 0$. Note that the growth rates corresponding to instability III increase as $c_s \rightarrow 0$ and they saturate at $c_s = 0$. Although the higher critical wavenumber and the growth rate around this critical wavenumber seem to be the same for both instabilities, the differences between them at low wavenumbers is also evident. These differences become more dramatic as the pitch angle increases.

Curvature terms cannot, of course, be neglected in global treatments of magnetized accretion disks. It is, therefore, not surprising that new instabilities, distinct from the MRI, have already been found in global studies in which strong fields were considered. In particular, Curry & Pudritz (1995) performed a global stability analysis to linear axisymmetric perturbations of an incompressible, dif-

ferentially rotating fluid, threaded by vertical and toroidal fields. They considered power-law radial profiles for the angular velocity and the toroidal and vertical components of the field. Each of these were parameterized as $\Omega \propto r^{-a}$, $B_\phi \propto r^{-b+1}$, and $B_z \propto r^{-c+1}$, respectively. Most of their analysis dealt with a constant vertical field and they allowed variations of the exponents (a, b) , with the restriction that they correspond to a physical equilibrium state with a stationary pressure distribution. Although the majority of that paper dealt with global characteristics, they also performed a WKB analysis and concluded that, for $3/2 \leq a = b \leq 2$ and $v_{A\phi} < 1$, the growth rate of unstable modes is suppressed for both short and long wavelengths and it approaches zero when $v_{A\phi} \rightarrow 1$. On the other hand, for $a = b \neq 2$ and $v_{A\phi} > 1$, they found a new instability, with a growth rate that increased with $v_{A\phi}$. They call this the Large Field Instability (LFI) and showed that it can be stabilized for sufficiently large v_{Az} .

It is worth mentioning the major qualitative differences between the LFI and the new instability discussed in §2.3 that emerges for $k_z < k_{\text{BH}}$ after the stabilization of the MRI. Although it is true that, for our instability to be present, it is necessary for the toroidal Alfvén speed to exceed the local sound speed, there is no need to invoke Alfvén speeds larger than the local rotational speed. This is in sharp contrast with the LFI which only appears for $v_{A\phi} > 1$. Regarding the range of unstable wavenumbers, the LFI remains unstable for $k_z \rightarrow 0$, albeit with a diminishing growth rate for large values of v_{Az} . This is not the case for the new instability present at low wavenumbers in our study. This can be seen, for example, in the left panels in Figure 2.4. Perhaps the most noticeable difference is that the two instabilities in Curry & Pudritz (1995) that are present in the case $a = b \neq 2$ do not seem to coexist under any particular circumstances. The instability present for $v_{A\phi} < 1$ reaches zero growth for $v_{A\phi} \rightarrow 1$, while the LFI appears

for $v_{A\phi} = 1$ and its growth rate is proportional to $v_{A\phi}$. When compressibility is considered, however, the two new instabilities found in our study can coexist even for Alfvén speeds smaller than the local rotational speed.

2.5.4 Implications for Shearing Box Simulations

In an attempt to capture the most relevant physics without all the complexities involved in global simulations, the shearing box approach has been widely used in numerical studies of magnetized accretion disks (see, e.g., Hawley, Gammie, & Balbus 1994). The aim of the shearing box approximation is to mimic a small region of a larger disk. The size of the box is usually $H_z \times 2\pi H_z \times H_z$, with H_z the thermal scale height of the isothermal disk. In this approach, it is common to adopt a pseudo-Cartesian local system centered at r_0 and in corotation with the disk with an angular frequency Ω_0 , with coordinates $x = r - r_0$, $y = r_0(\phi - \Omega_0 t)$, and z . The effects of differential rotation are then considered by imposing a velocity gradient in the radial direction. For a Keplerian accretion disk this is achieved by setting $v_y = -(3/2)\Omega_0 x$.

In most studies of unstratified shearing boxes, Alfvén speeds rarely exceed the value of the local sound speed (e.g., Hawley, Gammie, & Balbus 1995, 1996). This is mainly because they are designed to simulate the mid-plane of the disk where the flow is relatively dense. In §2.4.2, we have seen that, as long as the toroidal Alfvén speed does not exceed the critical value $v_{A\phi}^2 = c_s \kappa$, neglecting magnetic tension due to the curvature of toroidal field lines does not seem to affect the outcome of the MRI and hence the shearing box approach is well justified. However, when stratification is taken into account, usually by adopting a density profile of the form $\rho \propto \exp[-z^2/(2H^2)]$ in the case of isothermal disks, the steep drop in the density beyond a few scale heights can potentially lead to a magnetically dominated flow, with Alfvén speeds larger than the critical value $v_{A\phi}^2 = \kappa c_s$.

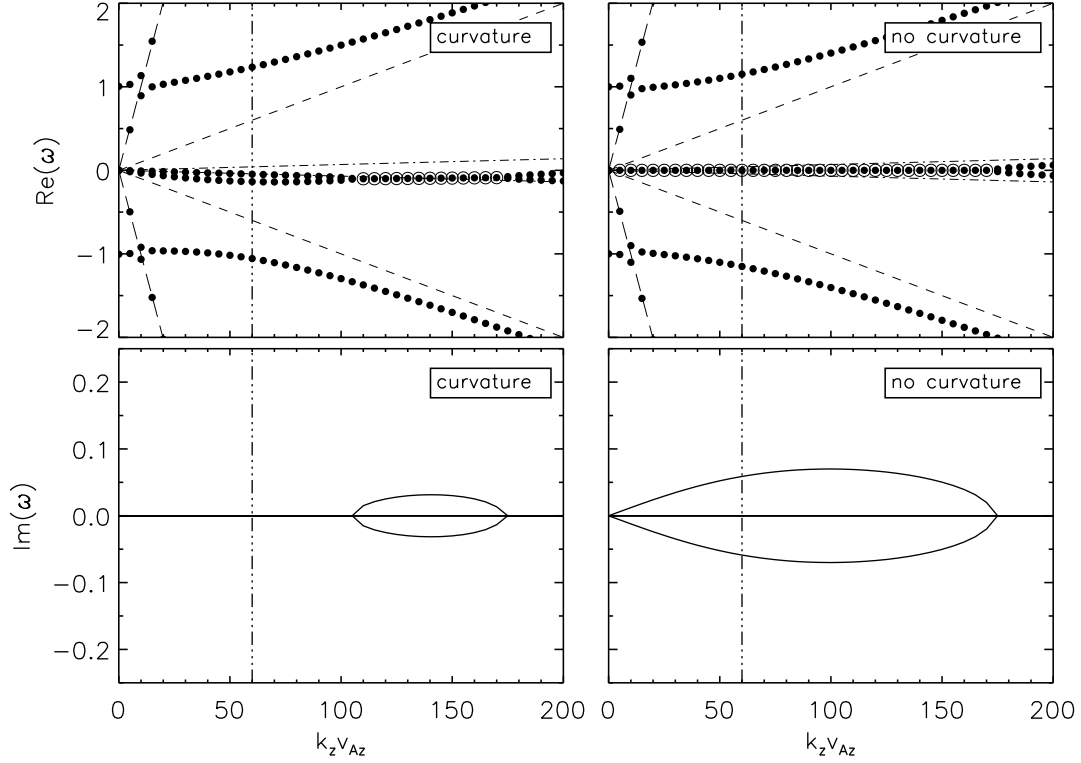


Figure 2.11 The implication of our study for shearing box simulations. *Left panels:* Solutions to the full dispersion relation (2.25), when all curvature terms are taken into account. *Right panels:* Solutions to the dispersion relation (2.31), i.e., when all curvature terms are neglected. In both cases, we have considered $c_s = 0.007$, $v_{Az} = 0.01$, $v_{A\phi} = 0.1$, and a Keplerian disk. Open circles in upper panels indicate unstable modes. The vertical line indicates the minimum wavenumber (i.e., largest wavelength) that can be accommodated in the simulations of a strongly-magnetized corona above a weakly magnetized disk by Miller & Stone (2000).

As discussed in the introduction, Miller & Stone (2000) carried out three-dimensional MHD simulations to study the evolution of a vertically stratified, isothermal, compressible, magnetized shear flow. The simulations were local in the plane of the disk but vertically extended up to ± 5 thermal scale heights. This allowed them to follow the highly coupled dynamics of the weakly magnetized disk core and the rarefied magnetically-dominated (i.e., $\beta < 1$) corona that formed above the disk, for several (10 to 50) orbital periods.

Miller & Stone (2000) considered a variety of models, all sharing the same initial physical background, but with different initial field configurations. In particular, they considered the following values: $\Omega_0 = 10^{-3}$, $2c_s^2 = 10^{-6}$ (so that $H_z = \sqrt{2}c_s/\Omega_0 = 1$), and $r_0 = 100$. We mention some of the results they obtained for the models with initial toroidal fields (BY), which were qualitatively similar to the zero net z -field (ZNZ) models. After a few orbital periods, the presence of a highly magnetized (with plasma $\beta \simeq 0.1 - 0.01$) and rarefied (with densities two orders of magnitude lower than the disk mid-plane density) corona above ~ 2 scale heights is evident. Within both the disk and the corona, the “toroidal” component of the field (B_y), favored by differential rotation, dominates the poloidal component of the field by more than one order of magnitude (with $B_x^2 \simeq B_z^2$).

We can compare the predictions of our study to the mode structure that one might expect from the standard compressible MRI for the particular values of sound and Alfvén speeds found in the strongly magnetized corona by Miller & Stone (2000). To this end, we consider as typical (dimensionless) values $c_s = 0.007$, $v_{A\phi} = 0.1$ and $v_{Az} = 0.01$, where we have assumed $\beta = 2(c_s/v_A)^2 \simeq 0.01$ and $B_\phi = 10B_z$. The largest features that their simulations are able to accommodate are those with $k_z \sim 60$ (corresponding to a wavelength of 10 in the vertical direction). As is seen in Figure 2.11, the role of the curvature terms is not negli-

ble in two different respects. First, they completely stabilize the perturbations on the longest scales well inside the numerical domain. Second, they significantly reduce the growth of the unstable modes.

It is difficult to extrapolate from the present work to address how the instabilities discussed here would couple to buoyancy in the presence of a stratified medium like the one considered by Miller & Stone (2000). Shearing boxes might also suffer from other problems when used to model strongly magnetized plasmas (e.g., the shearing sheet boundary conditions in the radial direction might not be appropriate for strong fields). The question is raised, however, about whether, because of their own Cartesian nature, they constitute a good approach at all to simulating compressible flows in which superthermal toroidal fields are present. Despite the fact that the generation of strongly magnetized regions via the MRI in stratified disks seems hard to avoid, their stability properties will ultimately depend on both the use of proper boundary conditions and proper accounting of the field geometry.

2.6 Summary and Conclusions

In this chapter we have addressed the role of toroidal fields on the stability of local axisymmetric perturbations in compressible, differentially rotating, MHD flows, when the geometrical curvature of the background is taken into account. In order to accomplish this task, without imposing restrictions on the strength of the background equilibrium field, we relaxed the Boussinesq approximation. In particular, we have studied under which circumstances the curvature terms, intimately linked to magnetic tension in cylindrical coordinate systems, cannot be neglected. We have shown that the MRI is stabilized and two distinct instabilities appear for strong toroidal fields. At least for large wavenumbers, the

structure of the modes seems to be the result of a purely local effect that is accounted for when compressibility and curvature terms are consistently taken into account. In particular, we have demonstrated that, even for rotationally supported cylindrical flows, both curvature terms and flow compressibility have to be considered if, locally, the toroidal Alfvén speed exceeds the critical value given by $v_{A\phi}^2 = (\kappa/\Omega)c_s\Omega r$ (in physical units).

There is little doubt that a realistic treatment of normal modes in magnetized accretion disks has to include gradients in the flow variables over large scales and should, therefore, be global in nature. The results presented in this chapter, however, provide the complete dispersion relation and, more importantly, analytic expressions for some of its solutions that should be recovered, in the appropriate limit, by a study of global modes in magnetized accretion disks, where compressibility effects are likely to be non negligible.

CHAPTER 3

THE SIGNATURE OF THE MAGNETOROTATIONAL INSTABILITY IN THE REYNOLDS AND MAXWELL STRESS TENSORS IN ACCRETION DISKS

The magnetorotational instability is thought to be responsible for the generation of magnetohydrodynamic turbulence that leads to enhanced outward angular momentum transport in accretion disks. In this Chapter, we present the first formal analytical proof showing that, during the exponential growth of the instability, the mean (averaged over the disk scale-height) Reynolds stress is always positive, the mean Maxwell stress is always negative, and hence the mean total stress is positive and leads to a net outward flux of angular momentum. More importantly, we show that the ratio of the Maxwell to the Reynolds stresses during the late times of the exponential growth of the instability is determined only by the local shear and does not depend on the initial spectrum of perturbations or the strength of the seed magnetic field. Even though we derived these properties of the stress tensors for the exponential growth of the instability in incompressible flows, numerical simulations of shearing boxes show that this characteristic is qualitatively preserved under more general conditions, even during the saturated turbulent state generated by the instability.

3.1 Introduction

Magnetohydrodynamic (MHD) turbulence has long been considered responsible for angular momentum transport in accretion disks surrounding astrophysical objects (Shakura & Sunyaev, 1973). Strong support for the importance of magnetic fields in accretion disks followed the realization by Balbus & Hawley (1991) that laminar flows with radially decreasing angular velocity profiles, that are hy-

drodynamically stable, turn unstable when threaded by a weak magnetic field. Since the discovery of this magnetorotational instability (MRI), a variety of local (e.g., Hawley, Gammie, & Balbus, 1995, 1996; Brandenburg, Nordlund, Stein, & Torkelsson, 1995; Brandenburg, 2001; Sano, Inutsuka, Turner, & Stone, 2004) and global (e.g., Hawley, 2000, 2001; Stone & Pringle, 2001) numerical simulations have shown that its non-linear evolution gives rise to a turbulent state characterized by enhanced Reynolds and Maxwell stresses, which in turn lead to outward angular momentum transport.

The relevance of the Reynolds and Maxwell stresses in determining the dynamics of a magnetized accretion disk is best appreciated by examining the equation for the dynamical evolution of the mean angular momentum density of a fluid element (see, e.g., Balbus & Hawley, 1998; Balbus & Papaloizou, 1999). Defining this quantity for a fluid element with mean density $\bar{\rho}$ as $\bar{l} \equiv r\bar{\rho}\bar{v}_\phi$ we can write in cylindrical coordinates

$$\partial_t \bar{l} + \nabla \cdot (\bar{l} \bar{\mathbf{v}}) = \frac{1}{4\pi} \nabla \cdot r (\bar{B}_\phi \bar{\mathbf{B}}) + \frac{1}{4\pi} \nabla \cdot r \overline{\delta B_\phi \delta \mathbf{B}} - \nabla \cdot r \overline{\rho \delta v_\phi \delta \mathbf{v}}, \quad (3.1)$$

where $\bar{\mathbf{v}}$, $\bar{\mathbf{B}}$, $\delta \mathbf{v}$, and $\delta \mathbf{B}$ stand for the means and fluctuations of the velocity and magnetic fields, respectively, and the bars denote suitable averages. It is clear that the presence of mean magnetic fields or of non-vanishing correlations between the fluctuations in the magnetic or velocity field can potentially allow for the specific angular momentum of a fluid element to change. In the absence of strong large-scale magnetic fields, the last two terms on the right hand side will dominate and we can simplify equation (3.1) as

$$\partial_t \bar{l} + \nabla \cdot (\bar{l} \bar{\mathbf{v}}) = -\nabla \cdot (r \bar{\mathcal{F}}), \quad (3.2)$$

where the vector $\bar{\mathcal{F}}$ characterizes the flux of angular momentum. Its components are related to the Reynolds and Maxwell stresses, $\bar{R}_{ij} = \overline{\rho \delta v_i \delta v_j}$ and $\bar{M}_{ij} =$

$\overline{\delta B_i \delta B_j} / 4\pi$ via

$$\bar{\mathcal{F}}_i \equiv \bar{R}_{i\phi} - \bar{M}_{i\phi} = \bar{T}_{i\phi}. \quad (3.3)$$

It is straightforward then to see that in order for matter in the disk to accrete, i.e., to lose angular momentum, the sign of the mean total stress, $\bar{T}_{r\phi}$, must be positive. Note that in the MRI-literature the Maxwell stress is defined as the negative of the correlations between magnetic field fluctuations. We have chosen instead to use a definition in which the sum of the diagonal terms has the same sign as the magnetic energy density.

In a differentially rotating MHD turbulent flow, the sign of the stress component $\bar{T}_{r\phi}$ will depend on the mechanism driving the turbulence (presumably the MRI), the mechanism mediating the energy cascade between different scales, and the dissipative processes that lead to saturation. Nevertheless, mechanical analogies of the MRI (Balbus & Hawley, 1992, 1998; Kato, Fukue, & Mineshige, 1998; Brandenburg & Campbell, 1997; Balbus, 2003) as well as analyses involving the excitation of single-wavenumber modes (Balbus & Hawley, 1992, 2002; Narayan, Quataert, Igumenshchev, & Abramowicz, 2002, see also §4) suggest that angular momentum is transported outwards even during the linear phase of the instability.

In this chapter, we derive analytic expressions that relate the dynamics of the MRI-driven fluctuations in Fourier space with the mean values, averaged over the disk scale-height, of the different stresses in physical space. This allows us to provide the first formal analytical proof showing that the MRI leads to a positive mean total stress $\bar{T}_{r\phi}$ which, in turn, leads to a net outward transport of angular momentum. Within this formalism, we demonstrate that the Reynolds stress is always positive, the Maxwell stress is always negative, and that the absolute value of the Maxwell stress is larger than the Reynolds stress as long as the flow

in the absence of magnetic fields is Rayleigh-stable. Moreover, we uncover a robust relationship between the Maxwell and Reynolds stresses as well as between the magnetic and kinetic energy of the MHD fluctuations during the late times of the linear phase of the instability. Specifically, we show that the ratio of the absolute value of the Maxwell and Reynolds stresses is equal to the ratio of magnetic and kinetic energy densities, and that both ratios depend only on the value of the local shear characterizing the flow.

The rest of the chapter is organized as follows. In §2 we state our assumptions. In §3 we present the complete solution to the MRI-eigenvector problem in Fourier space. We pay particular attention to the characterization of the complex nature of the MRI-eigenvectors. In §4, we present the formalism to derive analytic expressions for the mean physical Reynolds and Maxwell stresses in terms of the fluctuations in spectral space. We show that the MRI leads to a net outward transport of angular momentum. We also study there the different properties of the MRI-driven stresses during the late times of their exponential growth. In §5 we compare these stress properties with similar properties found in previous numerical simulations that addressed the non-linear turbulent regime using shearing boxes. We also present our conclusions there.

3.2 Assumptions

We are concerned here with the signature of the axisymmetric MRI in the mean values (averaged over the disk scale-height) of the Reynolds and Maxwell stress tensors. In particular, we consider a cylindrical, incompressible background, characterized by an angular velocity profile $\Omega = \Omega(r)\hat{z}$, threaded by a weak vertical magnetic field $\bar{\mathbf{B}} = \bar{B}_z\hat{z}$. In order to address this issue, we work in the shearing sheet approximation, which has proven useful to understand the physics of

disk phenomena when the scales involved are smaller than the disk radius.

The shearing sheet approximation consists of a first order expansion in the variable $r - r_0$ of all the quantities characterizing the flow at the fiducial radius r_0 . The goal of this expansion is to retain the most important terms governing the dynamics of the MHD fluid in a locally-Cartesian coordinate system co-orbiting and corotating with the background flow with local (Eulerian) velocity $\mathbf{v} = r_0 \Omega_0 \check{\phi}$. (For a more detailed discussion regarding the shearing sheet approximation, see Goodman & Xu 1994 and references therein.)

The equations for an incompressible MHD flow in the shearing sheet limit are given by

$$\begin{aligned} \frac{\partial \mathbf{v}}{\partial t} + (\mathbf{v} \cdot \nabla) \mathbf{v} &= -2\Omega_0 \times \mathbf{v} + q\Omega_0^2 \nabla (r - r_0)^2 \\ &\quad - \frac{1}{\rho} \nabla \left(P + \frac{\mathbf{B}^2}{8\pi} \right) + \frac{(\mathbf{B} \cdot \nabla) \mathbf{B}}{4\pi\rho} \end{aligned} \quad (3.4)$$

$$\frac{\partial \mathbf{B}}{\partial t} + (\mathbf{v} \cdot \nabla) \mathbf{B} = (\mathbf{B} \cdot \nabla) \mathbf{v} \quad (3.5)$$

where P is the pressure, ρ is the (constant) density, the factor $q \equiv -d \ln \Omega / d \ln r|_{r_0}$ parametrizes the magnitude of the local shear, and we have defined the (locally-Cartesian) differential operator

$$\nabla \equiv \check{\mathbf{r}} \frac{\partial}{\partial r} + \frac{\check{\phi}}{r_0} \frac{\partial}{\partial \phi} + \check{\mathbf{z}} \frac{\partial}{\partial z}, \quad (3.6)$$

where $\check{\mathbf{r}}$, $\check{\phi}$, and $\check{\mathbf{z}}$ are coordinate-independent, orthonormal vectors corotating with the background flow at r_0 .

In what follows, we focus our attention on fluctuations that depend only on the vertical coordinate. These types of fluctuations are known to have the fastest growth rates (Balbus & Hawley, 1992, 1998) and will, therefore, constitute the most important contributions to the corresponding Reynolds and Maxwell stresses during the exponential growth of the instability. The equations govern-

ing the dynamics of these fluctuations can be obtained by noting that the velocity and magnetic fields given by

$$\mathbf{v} = \delta v_r(z)\check{\mathbf{r}} + [-q\Omega_0(r - r_0) + \delta v_\phi(z)]\check{\boldsymbol{\phi}} + \delta v_z(z)\check{\mathbf{z}}, \quad (3.7)$$

$$\mathbf{B} = \delta B_r(z)\check{\mathbf{r}} + \delta B_\phi(z)\check{\boldsymbol{\phi}} + [\bar{B}_z + \delta B_z(z)]\check{\mathbf{z}}, \quad (3.8)$$

constitute a family of exact, non-linear, solutions to the one-dimensional incompressible MHD equations in the shearing sheet limit. As noted in Goodman & Xu (1994), the only non-linear terms, which are present through the perturbed magnetic energy density, are irrelevant in the incompressible case under study (i.e., the total pressure can be found *a posteriori* using the condition $\nabla \cdot \mathbf{v} = 0$).

Due to the divergenceless nature of the disturbances under consideration, the fluctuations in the vertical coordinate, $\delta v_z(z)$ and $\delta B_z(z)$, reduce to a constant. Without loss of generality, we take both constants to be zero¹. We can further simplify the system of equations (3.4) and (3.5) by removing the background shear flow $\mathbf{v}_{\text{shear}} = -q\Omega_0(r - r_0)\check{\boldsymbol{\phi}}$. We obtain the following set of equations for the fluctuations

$$\frac{\partial}{\partial t}\delta v_r = 2\Omega_0\delta v_\phi + \frac{\bar{B}_z}{4\pi\rho}\frac{\partial}{\partial z}\delta B_r, \quad (3.9)$$

$$\frac{\partial}{\partial t}\delta v_\phi = -(2 - q)\Omega_0\delta v_r + \frac{\bar{B}_z}{4\pi\rho}\frac{\partial}{\partial z}\delta B_\phi, \quad (3.10)$$

$$\frac{\partial}{\partial t}\delta B_r = \bar{B}_z\frac{\partial}{\partial z}\delta v_r, \quad (3.11)$$

$$\frac{\partial}{\partial t}\delta B_\phi = -q\Omega_0\delta B_r + \bar{B}_z\frac{\partial}{\partial z}\delta v_\phi, \quad (3.12)$$

where the first term on the right hand side of equation (3.10) is related to the epicyclic frequency $\kappa \equiv \sqrt{2(2 - q)}\Omega_0$, at which the flow variables oscillate in an unmagnetized disk.

¹Note that the fluctuations studied in Goodman & Xu (1994) are a particular case of the more general solutions (3.7) and (3.8).

It is convenient to define the new variables $\delta b_i \equiv \delta B_i / \sqrt{4\pi\rho}$ for $i = r, \phi$, and introduce dimensionless quantities by considering the characteristic time- and length-scales set by $1/\Omega_0$ and $\bar{B}_z/(\sqrt{4\pi\rho}\Omega_0)$. The equations satisfied by the dimensionless fluctuations, $\delta\tilde{v}_i, \delta\tilde{b}_i$, are then given by

$$\partial_{\tilde{t}}\delta\tilde{v}_r = 2\delta\tilde{v}_\phi + \partial_{\tilde{z}}\delta\tilde{b}_r, \quad (3.13)$$

$$\partial_{\tilde{t}}\delta\tilde{v}_\phi = -(2-q)\delta\tilde{v}_r + \partial_{\tilde{z}}\delta\tilde{b}_\phi, \quad (3.14)$$

$$\partial_{\tilde{t}}\delta\tilde{b}_r = \partial_{\tilde{z}}\delta\tilde{v}_r, \quad (3.15)$$

$$\partial_{\tilde{t}}\delta\tilde{b}_\phi = -q\delta\tilde{b}_r + \partial_{\tilde{z}}\delta\tilde{v}_\phi, \quad (3.16)$$

where \tilde{t} and \tilde{z} denote the dimensionless time and vertical coordinate, respectively.

In order to simplify the notation, we drop hereafter the tilde denoting the dimensionless quantities. In the rest of this chapter, all the variables are to be regarded as dimensionless, unless otherwise specified.

3.3 The Eigenvalue Problem for the MRI: A Formal Solution

In this section we provide a complete solution to the set of equations (3.13)–(3.16) in Fourier space. Taking the Fourier transform of this set with respect to the z -coordinate, we obtain the matrix equation

$$\partial_t \hat{\boldsymbol{\delta}}(k_n, t) = L \hat{\boldsymbol{\delta}}(k_n, t), \quad (3.17)$$

where the vector $\hat{\boldsymbol{\delta}}(k_n, t)$ stands for

$$\hat{\boldsymbol{\delta}}(k_n, t) = \begin{bmatrix} \delta\hat{v}_r(k_n, t) \\ \delta\hat{v}_\phi(k_n, t) \\ \delta\hat{b}_r(k_n, t) \\ \delta\hat{b}_\phi(k_n, t) \end{bmatrix} \quad (3.18)$$

and L represents the matrix

$$L = \begin{bmatrix} 0 & 2 & ik_n & 0 \\ -(2-q) & 0 & 0 & ik_n \\ ik_n & 0 & 0 & 0 \\ 0 & ik_n & -q & 0 \end{bmatrix}. \quad (3.19)$$

The functions denoted by $\hat{f}(k_n, t)$ correspond to the Fourier transform of the real functions, $f(z, t)$, and are defined via

$$\hat{f}(k_n, t) \equiv \frac{1}{2H} \int_{-H}^H f(z, t) e^{-ik_n z} dz, \quad (3.20)$$

where H is the (dimensionless) scale-height and k_n is the wavenumber in the z -coordinate,

$$k_n \equiv \frac{n\pi}{H}, \quad (3.21)$$

with n being an integer. Here, we have assumed periodic boundary conditions at $z = \pm H$.

In order to solve the matrix equation (3.17), it is convenient to find the base of eigenvectors, $\{\mathbf{e}_j\}$ with $j = 1, 2, 3, 4$, in which L is diagonal. This basis exists for all values of the wavenumber k_n (i.e., the rank of the matrix L is equal to 4, the dimension of the complex space) except for $k_n = 0$ and $k_n = \sqrt{2q}$. In this base, the action of L over the set $\{\mathbf{e}_j\}$ is equivalent to a scalar multiplication, i.e.,

$$L_{\text{diag}} \mathbf{e}_j = \sigma_j \mathbf{e}_j \quad \text{for } j = 1, 2, 3, 4, \quad (3.22)$$

where $\{\sigma_j\}$ are complex scalars.

3.3.1 Eigenvectors

In the base of eigenvectors, the matrix L has a diagonal representation $L_{\text{diag}} = \text{diag}(\sigma_1, \sigma_2, \sigma_3, \sigma_4)$. The eigenvalues $\{\sigma_j\}$, with $j = 1, 2, 3, 4$, are the roots of the

characteristic polynomial associated with L , i.e., the dispersion relation associated with the MRI (Balbus & Hawley, 1991, 1998),

$$(k_n^2 + \sigma_j^2)^2 + 2(2 - q)(k_n^2 + \sigma_j^2) - 4k_n^2 = 0, \quad (3.23)$$

and are given by

$$\sigma_j = \pm \left(-\Lambda \pm \sqrt{\Delta} \right)^{1/2}, \quad (3.24)$$

where we have defined the quantities Λ and Δ such that

$$\Lambda \equiv k_n^2 + (2 - q), \quad (3.25)$$

$$\Delta \equiv (2 - q)^2 + 4k_n^2. \quad (3.26)$$

For the modes with wavenumbers smaller than

$$k_{\text{BH}} \equiv \sqrt{2q}, \quad (3.27)$$

i.e., the largest unstable wavenumber for the the MRI, the difference $\sqrt{\Delta} - \Lambda$ is positive and we can define the “growth rate” γ and the “oscillation frequency” ω by

$$\gamma \equiv \left(\sqrt{\Delta} - \Lambda \right)^{1/2}, \quad (3.28)$$

$$\omega \equiv \left(\sqrt{\Delta} + \Lambda \right)^{1/2}, \quad (3.29)$$

both of which are real and positive (for all positive values of the parameter q). This shows that two of the solutions of equation (3.23) are real and the other two are imaginary. We can thus write the four eigenvalues in compact notation as

$$\sigma_1 = \gamma, \quad \sigma_2 = -\gamma, \quad \sigma_3 = i\omega, \quad \text{and} \quad \sigma_4 = -i\omega. \quad (3.30)$$

The set of normalized eigenvectors, $\{\mathbf{e}_{\sigma_j}\}$, associated with these eigenvalues can be written as

$$\mathbf{e}_{\sigma_j} \equiv \frac{\mathbf{e}_j}{\|\mathbf{e}_j\|} \quad \text{for} \quad j = 1, 2, 3, 4, \quad (3.31)$$

where

$$\mathbf{e}_j(k_n) = \begin{bmatrix} \sigma_j \\ (k_n^2 + \sigma_j^2)/2 \\ ik_n \\ -i2k_n\sigma_j/(k_n^2 + \sigma_j^2) \end{bmatrix}, \quad (3.32)$$

and the norms are given by

$$\|\mathbf{e}_j\| \equiv \left[\sum_{l=1}^4 e_j^l e_j^{l*} \right]^{1/2}, \quad (3.33)$$

where e_j^l is the l -th component of the (unnormalized) eigenvector associated with the eigenvalue σ_j . This set of four eigenvectors $\{\mathbf{e}_{\sigma_j}\}$, together with the set of scalars $\{\sigma_j\}$, constitute the full solution to the eigenvalue problem defined by the MRI.

The roots σ_j of the characteristic polynomial are not degenerate. Because of this, the set $\{\mathbf{e}_{\sigma_j}\}$ constitutes a basis set of four independent (complex) vectors that are able to span \mathbb{C}^4 , i.e., the space of tetra-dimensional complex vectors, for each value of k_n , provided that γ and ω are given by equations (3.28) and (3.29), respectively. Note, however, that they will not in general be orthogonal, i.e., $\mathbf{e}_{\sigma_j} \cdot \mathbf{e}_{\sigma_{j'}} \neq 0$ for $j \neq j'$. If desired, an orthogonal basis of eigenvectors can be constructed using the Gram-Schmidt orthogonalization procedure (see, e.g., Hoffman & Kunze, 1971).

3.3.2 Properties of the Eigenvectors

Despite the complicated functional dependence of the various complex eigenvector components on the wavenumber, k_n , some simple and useful relations hold for the most relevant (unstable) eigenvector. Figure 3.1 shows the four components of the eigenvector \mathbf{e}_γ as a function of the wavenumber for a Keplerian profile ($q = 3/2$) and illustrates the fact that the modulus of the different components

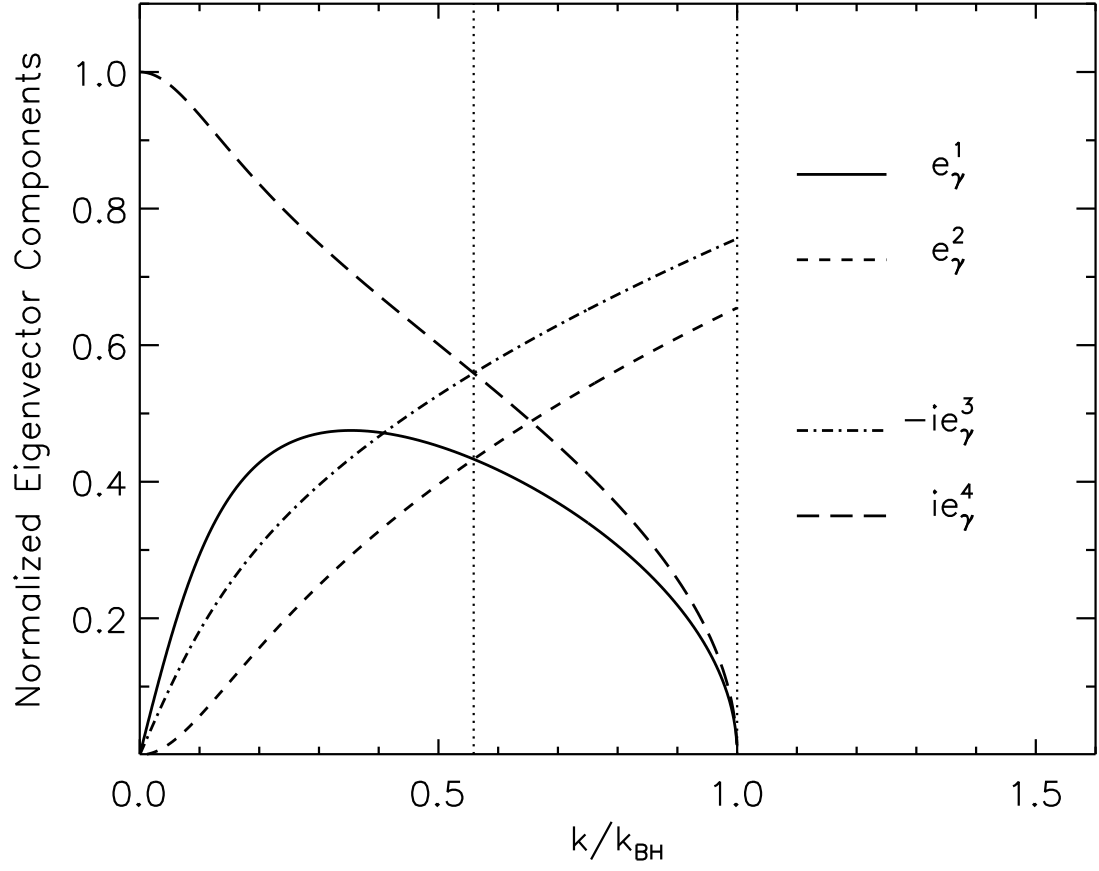


Figure 3.1 The components of the normalized unstable eigenvector e_γ defined in equation (3.31). The vertical *dotted* lines denote the wavenumber corresponding to the most unstable mode, k_{max} , (eq. [3.37]), and the largest unstable wavenumber, k_{BH} , (eq. [3.27]).

satisfy two simple inequalities

$$|e_\gamma^4| > |e_\gamma^1|, \quad (3.34)$$

$$|e_\gamma^3| > |e_\gamma^2|, \quad (3.35)$$

for all values of $0 < k_n < k_{\text{BH}}$. These inequalities do indeed hold for all values of the shear parameter $0 < q < 2$.

We also note that equation (3.32) exposes a relationship among the components of any given eigenvector e_{σ_j} . It is immediate to see that

$$\frac{-e_{\sigma_j}^4}{e_{\sigma_j}^1} = \frac{e_{\sigma_j}^3}{e_{\sigma_j}^2} = \frac{2ik_n}{k_n^2 + \sigma_j^2}, \quad \text{for } j = 1, 2, 3, 4. \quad (3.36)$$

In particular, the following equalities hold for the components of the unstable eigenvector, e_γ , at the wavenumber

$$k_{\text{max}} \equiv \frac{q}{2} \sqrt{\frac{4}{q} - 1}, \quad (3.37)$$

for which the growth rate is maximum, $\gamma_{\text{max}} \equiv q/2$,

$$e_\gamma^1(k_{\text{max}}) = e_\gamma^2(k_{\text{max}}) = \frac{1}{2} \sqrt{\frac{q}{2}}, \quad (3.38)$$

$$e_\gamma^3(k_{\text{max}}) = -e_\gamma^4(k_{\text{max}}) = \frac{i}{2} \sqrt{2 - \frac{q}{2}}. \quad (3.39)$$

As we show in the next section, the inequalities (3.34) and (3.35), together with equations (3.38) and (3.39), play an important role in establishing the relative magnitude of the different mean stress components and mean magnetic energies associated with the fluctuations in the velocity and magnetic fields.

Finally, we stress here that the phase differences among the different eigenvector components cannot be eliminated by a linear (real or complex) transformation. In other words, it is not possible to obtain a set of four real (or purely imaginary, for that matter) linearly independent set of eigenvectors that will also

form a basis in which to expand the general solution to equation (3.17). Taking into consideration the complex nature of the eigenvalue problem in MRI is crucial when writing the physical solutions for the spatio-temporal evolution of the velocity and magnetic field fluctuations in terms of complex eigenvectors. As we discuss in the next section, this in turn has a direct implication for the expressions that are needed in the calculation of the mean stresses in physical (as opposed to spectral) space.

3.3.3 Temporal Evolution

We have now all the elements to solve equation (3.17). In the base defined by $\{\mathbf{e}_{\sigma_j}\}$, any given vector $\hat{\boldsymbol{\delta}}(k_n, t)$ can be written as

$$\hat{\boldsymbol{\delta}}(k_n, t) = \sum_{j=1}^4 a_j(k_n, t) \mathbf{e}_{\sigma_j}, \quad (3.40)$$

where the coefficients $a_j(k_n, t)$, i.e., the coordinates of $\hat{\boldsymbol{\delta}}(k_n, t)$ in the eigenvector basis, are the components of the vector $\mathbf{a}(k_n, t)$ obtained from the transformation

$$\mathbf{a}(k_n, t) = Q^{-1} \hat{\boldsymbol{\delta}}(k_n, t). \quad (3.41)$$

The matrix Q^{-1} is the matrix for the change of coordinates from the standard basis to the normalized eigenvector basis and can be obtained by calculating the inverse of the matrix

$$Q = [\mathbf{e}_{\sigma_1} \ \mathbf{e}_{\sigma_2} \ \mathbf{e}_{\sigma_3} \ \mathbf{e}_{\sigma_4}]. \quad (3.42)$$

Multiplying equation (3.17) at the left side by Q^{-1} and using the fact that

$$L_{\text{diag}} = Q^{-1} L Q, \quad (3.43)$$

we obtain a matrix equation for the vector $\mathbf{a}(k_n, t)$,

$$\partial_t \mathbf{a}(k_n, t) = L_{\text{diag}} \mathbf{a}(k_n, t), \quad (3.44)$$

which can be written in components as

$$\partial_t a_j(k_n, t) = \sigma_j a_j(k_n, t) \quad \text{with} \quad j = 1, 2, 3, 4. \quad (3.45)$$

The solution of these equations is then given by

$$a_j(k_n, t) = a_j(k_n, 0) e^{\sigma_j t} \quad \text{with} \quad j = 1, 2, 3, 4. \quad (3.46)$$

We can finally write the solution to equation (3.17) as

$$\hat{\boldsymbol{\delta}}(k_n, t) = \sum_{j=1}^4 a_j(k_n, 0) e^{\sigma_j t} \mathbf{e}_{\sigma_j}, \quad (3.47)$$

where $\{\sigma_j\}$ and $\{\mathbf{e}_{\sigma_j}\}$, for $j = 1, 2, 3, 4$, are given by equations (3.30) and (3.31), and the initial conditions $\mathbf{a}(k_n, 0)$ are related to the initial spectrum of fluctuations, $\hat{\boldsymbol{\delta}}(k_n, 0)$, via $\mathbf{a}(k_n, 0) = Q^{-1} \hat{\boldsymbol{\delta}}(k_n, 0)$.

3.4 Net Angular Momentum Transport by the MRI

Having obtained the solution for the temporal evolution of the velocity and magnetic field fluctuations in Fourier space we can now explore the effect of the MRI on the mean values of the Reynolds and Maxwell stresses.

3.4.1 Definitions and Mean Values of Correlation Functions

The average over the disk scale-height, $2H$, of the product of any two physical quantities, $f(z, t) g(z, t)$,

$$\overline{fg}(t) \equiv \frac{1}{2H} \int_{-H}^H f(z, t) g(z, t) dz, \quad (3.48)$$

can be written in terms of their corresponding Fourier transforms, $\hat{f}(k_n, t)$ and $\hat{g}(k_n, t)$, as

$$\overline{fg}(t) = 2 \sum_{n=1}^{\infty} \text{Re}[\hat{f}(k_n, t) \hat{g}^*(k_n, t)]. \quad (3.49)$$

Here, $\text{Re}[\]$ stands for the real part of the quantity between brackets, the asterisk in $\hat{g}^*(k_n, t)$ denotes the complex conjugate, and we have considered that the functions $f(z, t)$, and $g(z, t)$ (both with zero mean) are real and, therefore, their Fourier transforms satisfy $\hat{f}(-k_n, t) = \hat{f}^*(k_n, t)$.

For convenience, we provide here a brief demonstration of equation (3.49). The relationship between the mean value of the product of two real functions, \overline{fg} , and their corresponding Fourier transforms can be obtained by substituting the expressions for $f(z, t)$ and $g(z, t)$ in terms of their Fourier series, i.e.,

$$f(z, t) \equiv \sum_{n=-\infty}^{\infty} \hat{f}(k_n, t) e^{ik_n z}, \quad (3.50)$$

into the expression for the mean value, equation (3.48). The result is,

$$\overline{fg}(t) = \sum_{n,m=-\infty}^{\infty} \hat{f}(k_n, t) \hat{g}^*(k_m, t) \frac{1}{2H} \int_{-H}^H e^{i(k_n - k_m)z} dz, \quad (3.51)$$

which can be rewritten using the orthogonality of the Fourier polynomials in the interval $[-H, H]$ as

$$\overline{fg}(t) = \sum_{n=-\infty}^{\infty} \hat{f}(k_n, t) \hat{g}^*(k_n, t). \quad (3.52)$$

This is the discrete version of Plancherel's theorem which states that the Fourier transform is an isometry, i.e., it preserves the inner product (see., e.g., Shilov & Silverman, 1973). Denoting the Fourier transforms $\hat{f}(k_n, t)$ and $\hat{g}^*(k_n, t)$ by \hat{f}_n and

\hat{g}_n^* in order to simplify the notation, we can write the following series of identities

$$\overline{fg}(t) = \sum_{n=-\infty}^{\infty} \hat{f}_n \hat{g}_n^*, \quad (3.53)$$

$$= \hat{f}_0 \hat{g}_0 + \sum_{n=1}^{\infty} \hat{f}_n \hat{g}_n^* + \sum_{n=-\infty}^{-1} \hat{f}_n \hat{g}_n^* \quad (3.54)$$

$$= \hat{f}_0 \hat{g}_0 + \sum_{n=1}^{\infty} \left[\hat{f}_n \hat{g}_n^* + \hat{f}_{-n} \hat{g}_{-n}^* \right] \quad (3.55)$$

$$= \hat{f}_0 \hat{g}_0 + \sum_{n=1}^{\infty} \left[\hat{f}_n \hat{g}_n^* + \hat{f}_n^* \hat{g}_n \right] \quad (3.56)$$

$$= \hat{f}_0 \hat{g}_0 + 2 \sum_{n=1}^{\infty} \text{Re}[\hat{f}_n \hat{g}_n^*], \quad (3.57)$$

where we have used the fact that the functions $f(z, t)$ and $g(z, t)$ are real and, hence, their Fourier transforms satisfy $\hat{f}_{-n} = \hat{f}_n^*$ and $\hat{g}_{-n} = \hat{g}_n^*$. Note that the factors \hat{f}_0 and \hat{g}_0 are just the mean values of the functions $f(z, t)$ and $g(z, t)$ and, therefore, do not contribute to the final expression in equation (3.49). It is then clear that, no matter whether the initial Fourier transforms corresponding to the functions $f(z, t)$ and $g(z, t)$ are real or imaginary, the mean value, $\overline{fg}(t)$, will be well defined.

Using equation (3.49), we can write the mean values of the quantities

$$R_{ij}(z, t) \equiv \delta v_i(z, t) \delta v_j(z, t), \quad (3.58)$$

$$M_{ij}(z, t) \equiv \delta b_i(z, t) \delta b_j(z, t), \quad (3.59)$$

with $i, j = r, \phi$, as

$$\bar{R}_{ij}(t) \equiv 2 \sum_{n=1}^{\infty} \text{Re}[\delta \hat{v}_i(k_n, t) \delta \hat{v}_j^*(k_n, t)], \quad (3.60)$$

$$\bar{M}_{ij}(t) \equiv 2 \sum_{n=1}^{\infty} \text{Re}[\delta \hat{b}_i(k_n, t) \delta \hat{b}_j^*(k_n, t)], \quad (3.61)$$

where the temporal evolution of the fluctuations in Fourier space, $\delta \hat{v}_r(k_n, t)$, $\delta \hat{v}_\phi(k_n, t)$, $\delta \hat{b}_r(k_n, t)$, and $\delta \hat{b}_\phi(k_n, t)$, is governed by equation (3.47).

3.4.2 Properties of the MRI-Driven Stresses

At late times, during the exponential growth of the instability, the branch of unstable modes will dominate the growth of the fluctuations and we can write the most important (secular) contribution to the mean stresses by defining

$$\bar{R}_{r\phi}(t) = 2 \sum_{n=1}^{N_{\text{BH}}} \mathcal{R}_{r\phi}(k_n) |a_1|^2 e^{2\gamma t} + \dots, \quad (3.62)$$

$$\bar{M}_{r\phi}(t) = 2 \sum_{n=1}^{N_{\text{BH}}} \mathcal{M}_{r\phi}(k_n) |a_1|^2 e^{2\gamma t} + \dots, \quad (3.63)$$

where N_{BH} is the index associated with the largest unstable wavenumber (i.e., the mode labeled with highest $k_n < k_{\text{BH}}$)², the dots represent terms that grow at most as fast as $e^{\gamma t}$, and we have defined the functions

$$\mathcal{R}_{r\phi}(k_n) = \frac{\text{Re}[\mathbf{e}_\gamma^1 \mathbf{e}_\gamma^{2*}]}{\|\mathbf{e}_1\|^2}, \quad (3.64)$$

and

$$\mathcal{M}_{r\phi}(k_n) = \frac{\text{Re}[\mathbf{e}_\gamma^3 \mathbf{e}_\gamma^{4*}]}{\|\mathbf{e}_1\|^2}. \quad (3.65)$$

Note that these functions are not the Fourier transforms of the Reynolds and Maxwell stresses, but rather represent the contribution of the fluctuations at the scale k_n to the corresponding mean physical stresses. We will refer to these quantities as the *per-k* contributions to the mean.

The complex nature of the various components of the unstable eigenvector, together with the inequalities (3.34) and (3.35), dictate the relative magnitude of the *per-k* contributions associated with the Maxwell and Reynolds stresses and the magnetic and kinetic energy densities. Figure 3.2 shows the functions $\mathcal{R}_{r\phi}(k_n)$ and $\mathcal{M}_{r\phi}(k_n)$ for a Keplerian profile ($q = 3/2$). It is evident from this figure that, in this case, the *per-k* contribution of the Maxwell stress is always larger than

²Extending the summations to include the non-growing modes with $k_n > k_{\text{BH}}$ would only add a negligible oscillatory contribution to the mean stresses.

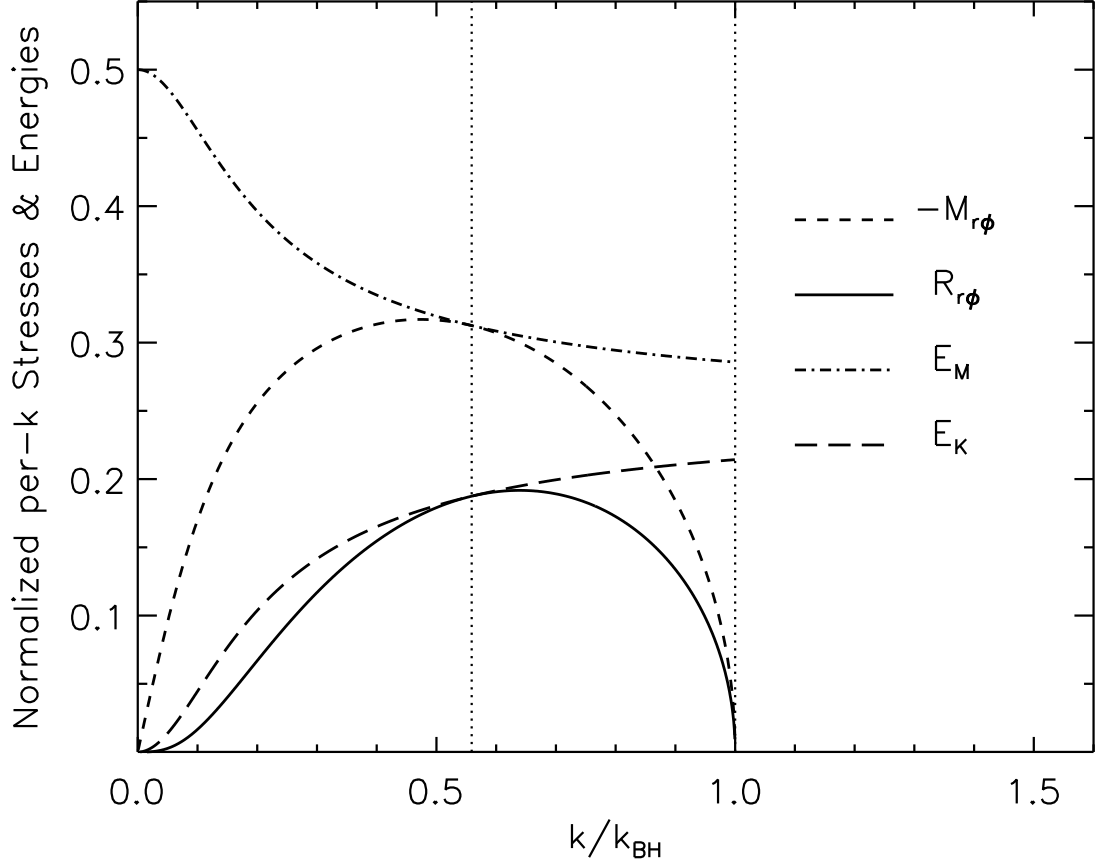


Figure 3.2 The *per-k* contributions, $\mathcal{R}_{r\phi}(k_n)$, $\mathcal{M}_{r\phi}(k_n)$, $\mathcal{E}_K(k_n)$, and $\mathcal{E}_M(k_n)$, associated with the corresponding mean physical stresses (3.62) and (3.63) and mean physical magnetic and kinetic energy densities, eqs. (3.75) and (3.74). The vertical *dotted* lines denote the wavenumber corresponding to the most unstable mode, k_{\max} , (eq. [3.37]), and the largest unstable wavenumber, k_{BH} , (eq. [3.27]).

the the *per-k* contribution corresponding to the Reynolds stress, i.e., $-\mathcal{M}_{r\phi}(k_n) > \mathcal{R}_{r\phi}(k_n)$. This is indeed true for all values of the shear parameter $0 < q < 2$ (see below).

The coefficients e_γ^j for $j = 1, 2, 3, 4$ in equations (3.64) and (3.65) are the components of the (normalized) unstable eigenvector given by equation (3.32) with $\sigma_1 = \gamma$. We can then write the mean values of the Reynolds and Maxwell stresses, to leading order in time, as

$$\bar{R}_{r\phi}(t) = \sum_{n=1}^{N_{\text{BH}}} \gamma (k_n^2 + \gamma^2) \frac{|a_1|^2}{\|\mathbf{e}_1\|^2} e^{2\gamma t}, \quad (3.66)$$

$$\bar{M}_{r\phi}(t) = -4 \sum_{n=1}^{N_{\text{BH}}} \frac{\gamma k_n^2}{k_n^2 + \gamma^2} \frac{|a_1|^2}{\|\mathbf{e}_1\|^2} e^{2\gamma t}. \quad (3.67)$$

Equations (3.66) and (3.67) show explicitly that the mean Reynolds and Maxwell stresses will be, respectively, positive and negative,

$$\bar{R}_{r\phi}(t) > 0 \quad \text{and} \quad \bar{M}_{r\phi}(t) < 0. \quad (3.68)$$

This, in turn, implies that the mean total MRI-driven stress will be always positive, i.e.,

$$\bar{T}_{r\phi}(t) = \bar{R}_{r\phi}(t) - \bar{M}_{r\phi}(t) > 0, \quad (3.69)$$

driving a net outward flux of angular momentum as discussed in §3.1.

It is not hard to show now that the magnitude of the Maxwell stress, $-\bar{M}_{r\phi}(t)$, will always be larger than the magnitude of the Reynolds stress, $\bar{R}_{r\phi}(t)$, provided that the shear parameter is $q < 2$. In order to see that this is the case, it is enough to show that the ratio of the *per-k* contributions to the Reynolds and Maxwell stresses, defined in equations (3.64) and (3.65), satisfy

$$\frac{-\mathcal{M}_{r\phi}(k_n)}{\mathcal{R}_{r\phi}(k_n)} = \frac{4k_n^2}{(k_n^2 + \gamma^2)^2} > 1, \quad (3.70)$$

for all the wavenumbers k_n . Adding and subtracting the factor $(k_n^2 + \gamma^2)^2$ in the numerator and using the dispersion relation (3.23) we obtain,

$$\frac{-\mathcal{M}_{r\phi}(k_n)}{\mathcal{R}_{r\phi}(k_n)} = 1 + \frac{2(2-q)}{k_n^2 + \gamma^2}, \quad (3.71)$$

which is clearly larger than unity for all values of k_n provided that $q < 2$. It is then evident that the mean Maxwell stress will be larger than the mean Reynolds stress as long as the flow is Rayleigh-stable, i.e.,

$$-\bar{M}_{r\phi}(t) > \bar{R}_{r\phi}(t) \quad \text{for} \quad 0 < q < 2. \quad (3.72)$$

This inequality provides analytical support to the results obtained in numerical simulations, i.e., that the Maxwell stress constitutes the major contribution to the total stress in magnetized accretion disks (see, e.g., Hawley, Gammie, & Balbus, 1995).

We conclude this section by calculating the ratio $-\bar{M}_{r\phi}(t)/\bar{R}_{r\phi}(t)$ at late times during the exponential growth of the instability. For times that are long compared to the dynamical time-scale, the unstable mode with maximum growth dominates the dynamics of the mean stresses and the sums over all wavenumbers in equations (3.66) and (3.67) can be approximated by a single term corresponding to $k_n = k_{\max}$. In this case, we can use equations (3.38) and (3.39) to write

$$\lim_{t \gg 1} \frac{-\bar{M}_{r\phi}(t)}{\bar{R}_{r\phi}(t)} = - \left. \frac{\text{Re}[\mathbf{e}_\gamma^3 \mathbf{e}_\gamma^{4*}]}{\text{Re}[\mathbf{e}_\gamma^1 \mathbf{e}_\gamma^{2*}]} \right|_{k_{\max}} = \frac{4-q}{q}. \quad (3.73)$$

This result shows explicitly that the ratio $-\bar{M}_{r\phi}(t)/\bar{R}_{r\phi}(t)$ depends only on the shear parameter and not on the magnitude or even the sign of the magnetic field. These same conclusions can be drawn for the ratio between the magnetic and kinetic energies associated with the fluctuations.

3.5 Energetics of MRI-driven Fluctuations

The relationships given in equation (3.36) lead to identities and inequalities involving the different mean stress components and the mean kinetic and magnetic energies associated with the fluctuations. In particular, the total mean stress is bounded by the total mean energy of the fluctuations. Moreover, the ratio of the mean magnetic to the mean kinetic energies is equal to the absolute value of the ratio between the mean Maxwell and the mean Reynolds stresses given by equation (3.84).

As we defined the mean stresses in terms of their *per-k* contributions in §3.4, we can also define, to leading order in time, the mean energies associated with the fluctuations in the velocity and magnetic field by

$$\bar{E}_K(t) = 2 \sum_{n=1}^{k_{\text{BH}}} \mathcal{E}_K(k_n) |a_1|^2 e^{2\gamma t}, \quad (3.74)$$

$$\bar{E}_M(t) = 2 \sum_{n=1}^{k_{\text{BH}}} \mathcal{E}_M(k_n) |a_1|^2 e^{2\gamma t}, \quad (3.75)$$

where the corresponding *per-k* contributions are given by

$$\mathcal{E}_K(k_n) = \frac{1}{2} [\mathcal{R}_{rr}(k_n) + \mathcal{R}_{\phi\phi}(k_n)], \quad (3.76)$$

$$\mathcal{E}_M(k_n) = \frac{1}{2} [\mathcal{M}_{rr}(k_n) + \mathcal{M}_{\phi\phi}(k_n)]. \quad (3.77)$$

Figure 3.2 shows the dependences of the functions $\mathcal{E}_K(k_n)$ and $\mathcal{E}_M(k_n)$ for a Keplerian profile, $q = 3/2$, and illustrates the fact that $\mathcal{E}_M(k_n) > \mathcal{E}_K(k_n)$ for $0 < k_n < k_{\text{BH}}$ and $0 < q < 2$.

Using equation (3.36) and the expression for the dispersion relation (3.23), it is easy to show that the following inequalities hold for *each* wavenumber k_n

$$\frac{\mathcal{R}_{r\phi}(k_n)}{\mathcal{E}_K(k_n)} = \frac{-\mathcal{M}_{r\phi}(k_n)}{\mathcal{E}_M(k_n)} = \frac{2\gamma(k_n)}{q} \leq 1, \quad (3.78)$$

as long as $q > 0$. It immediately follows that the same inequalities are also satisfied by the corresponding means, i.e.,

$$\bar{R}_{r\phi}(t) \leq \bar{E}_K(t), \quad (3.79)$$

$$-\bar{M}_{r\phi}(t) \leq \bar{E}_M(t). \quad (3.80)$$

This result, in turn, implies that the total mean energy associated with the fluctuations, $\bar{E}(t) = \bar{E}_K(t) + \bar{E}_M(t)$, sets an upper bound on the total mean stress, i.e.,

$$\bar{T}_{r\phi}(t) \leq \bar{E}(t). \quad (3.81)$$

At late times during the exponential growth of the instability, the growth of the fluctuations is dominated by the mode with $k_n = k_{\max}$ and the mean stress $\bar{T}_{r\phi}(t)$ will tend to the total mean energy $\bar{E}(t)$, i.e.,

$$\lim_{t \gg 1} \bar{T}_{r\phi}(t) = \lim_{t \gg 1} \bar{E}(t). \quad (3.82)$$

Furthermore, according to the first equality in equation (3.78), we can conclude that the ratio of the mean magnetic to the mean kinetic energies has the same functional dependence on the shear parameter, q , as does the (negative of the) ratio between the mean Maxwell and the mean Reynolds stresses given by equation (3.84), i.e.,

$$\lim_{t \gg 1} \frac{\bar{E}_M(t)}{\bar{E}_K(t)} = \frac{4 - q}{q}. \quad (3.83)$$

Therefore, the mean energy associated with magnetic fluctuations is always larger than the mean energy corresponding to kinetic fluctuations as long as the flow is Rayleigh-stable.

3.6 Discussion

In this chapter we have studied the properties of the mean Maxwell and Reynolds stresses in a differentially rotating flow during the exponential growth of the

magnetorotational instability and have identified its signature in their temporal evolution. In order to achieve this goal, we obtained the complex eigenvectors associated with the magnetorotational instability and presented the formalism needed to calculate the temporal evolution of the mean Maxwell and Reynolds stresses in terms of them.

We showed that, during the phase of exponential growth characterizing the instability, the mean values of the Reynolds and Maxwell stresses are always positive and negative, respectively, i.e., $\bar{R}_{r\phi}(t) > 0$ and $\bar{M}_{r\phi}(t) < 0$. This leads, automatically, to a net outward angular momentum flux mediated by a total mean positive stress, $\bar{T}_{r\phi}(t) = \bar{R}_{r\phi}(t) - \bar{M}_{r\phi}(t) > 0$. We further demonstrated that, for a flow that is Rayleigh-stable (i.e., when $q = -d \ln \Omega / d \ln r < 2$), the contributions to the total stress associated with the correlated magnetic fluctuations are always larger than the contributions due to the correlations in the velocity fluctuations, i.e., $-\bar{M}_{r\phi}(t) > \bar{R}_{r\phi}(t)$.

We also proved that, during the late times of the linear phase of the instability, the ratio of the Maxwell to the Reynolds stresses simply becomes

$$\lim_{t \gg 1} \frac{-\bar{M}_{r\phi}(t)}{\bar{R}_{r\phi}(t)} = \frac{4 - q}{q}. \quad (3.84)$$

This is a remarkable result, because it does not depend on the initial spectrum of fluctuations or the value of the seed magnetic field. It is, therefore, plausible that, even in the saturated state of the instability, when fully developed turbulence is present, the ratio of the Maxwell to the Reynolds stresses has also a very weak dependence on the properties of the turbulence and is determined mainly by the local shear.

For shearing box simulations with a Keplerian velocity profile, the ratio of the Maxwell to the Reynolds stresses in the saturated state has been often quoted to be constant indeed (of order $\simeq 4$), almost independent of the setup of the sim-

ulation, the initial conditions, and the boundary conditions. This is shown in Figure 3.3, where we plot the correlation between the Maxwell stress, $\bar{M}_{r\phi}$, and the Reynolds stress, $\bar{R}_{r\phi}$, at saturation, for a number of numerical simulations of shearing boxes, with Keplerian velocity profiles but different initial conditions (data points are from Hawley, Gammie, & Balbus 1995; Stone & Balbus 1996; Fleming & Stone 2003; Sano, Inutsuka, Turner, & Stone 2004; Gardiner & Stone 2005). It is remarkable that this linear correlation between the stresses, in fully developed turbulent states resulting from very different sets of initial conditions, spans over six orders of magnitude. The ratio $-\bar{M}_{r\phi}/\bar{R}_{r\phi} = 4$ is shown in the same figure with a *dashed line*, whereas the *solid line* shows the ratio obtained from equation (3.84) for $q = 3/2$, i.e., $-\bar{M}_{r\phi}/\bar{R}_{r\phi} = 5/3$, characterizing the linear phase of the instability. Hence, to within factors of order unity, the ratio between the stresses in the turbulent state seems to be independent of the initial set of conditions over a wide range of parameter space and to be similar to the value set during the linear phase of the instability.

The dependence of the ratio of the stresses on the shear parameter, q , has not been studied extensively with numerical simulations so far. The only comprehensive study is by Hawley, Balbus, & Winters (1999) and their result is shown in Figure 3.4. Note that, Hawley, Balbus, & Winters (1999) quote the average stresses and the width of their distribution throughout the simulations, but not the uncertainty in the mean values. In Fig. 3.4, we have assigned a nominal 30% uncertainty to their quoted mean values. This is comparable to the usual quoted uncertainty for the stresses and is also comparable to the spread in Fig. 3.3. Superimposed on the figure is the analytic prediction, equation (3.84), for the ratio of the stresses as a function of the shear q at late times during the exponential growth of the MRI. In this case, the qualitative trend followed by the ratio of

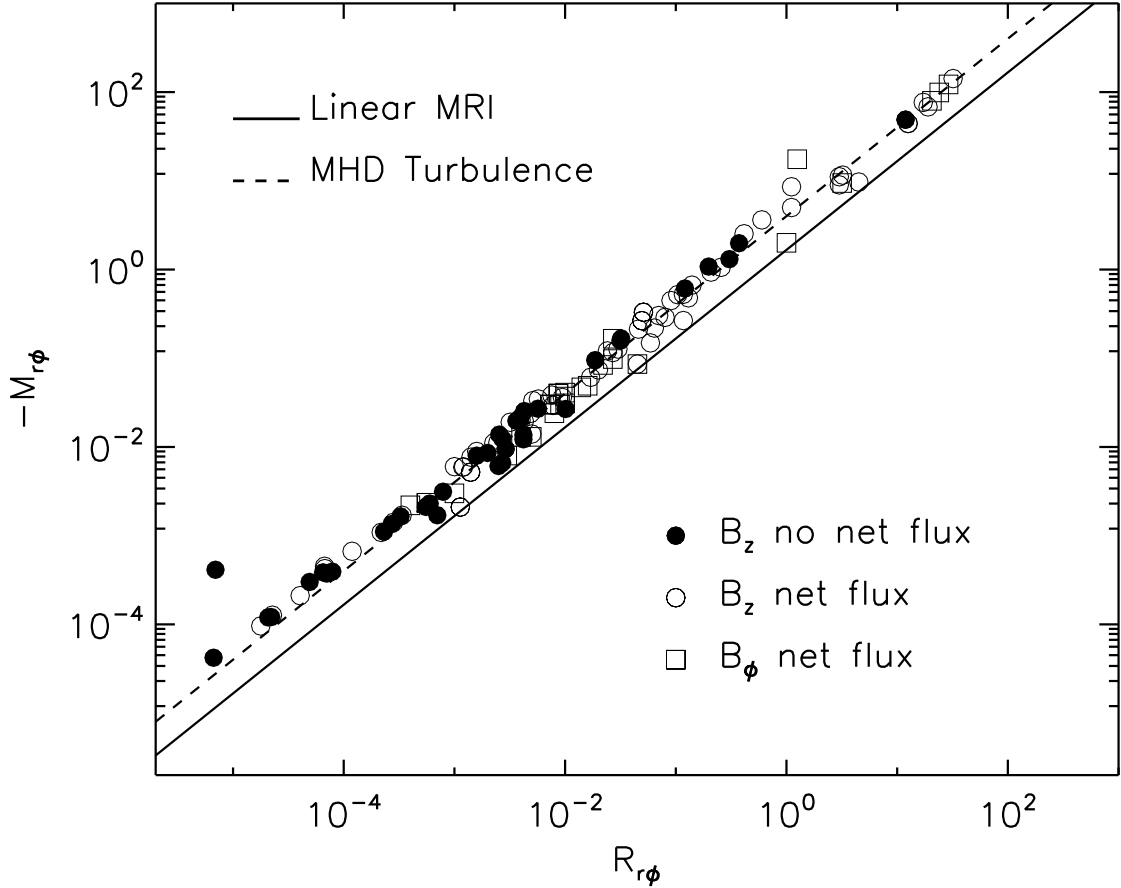


Figure 3.3 The correlation between the Maxwell stress, $\bar{M}_{r\phi}$, and the Reynolds stress, $\bar{R}_{r\phi}$, at saturation obtained in numerical simulations of shearing boxes with Keplerian velocity profiles but different initial conditions. *Filled circles* correspond to simulations with zero net vertical magnetic flux. *Open circles* correspond to simulations with finite net vertical magnetic flux. *Squares* correspond to simulations with an initial toroidal field. (See the text for references.) The *dashed line* is the correlation often quoted in the literature. The *solid line* corresponds to the late-time ratio of the two stresses during the exponential growth of the MRI, as predicted by equation (3.84) for $q = 3/2$.

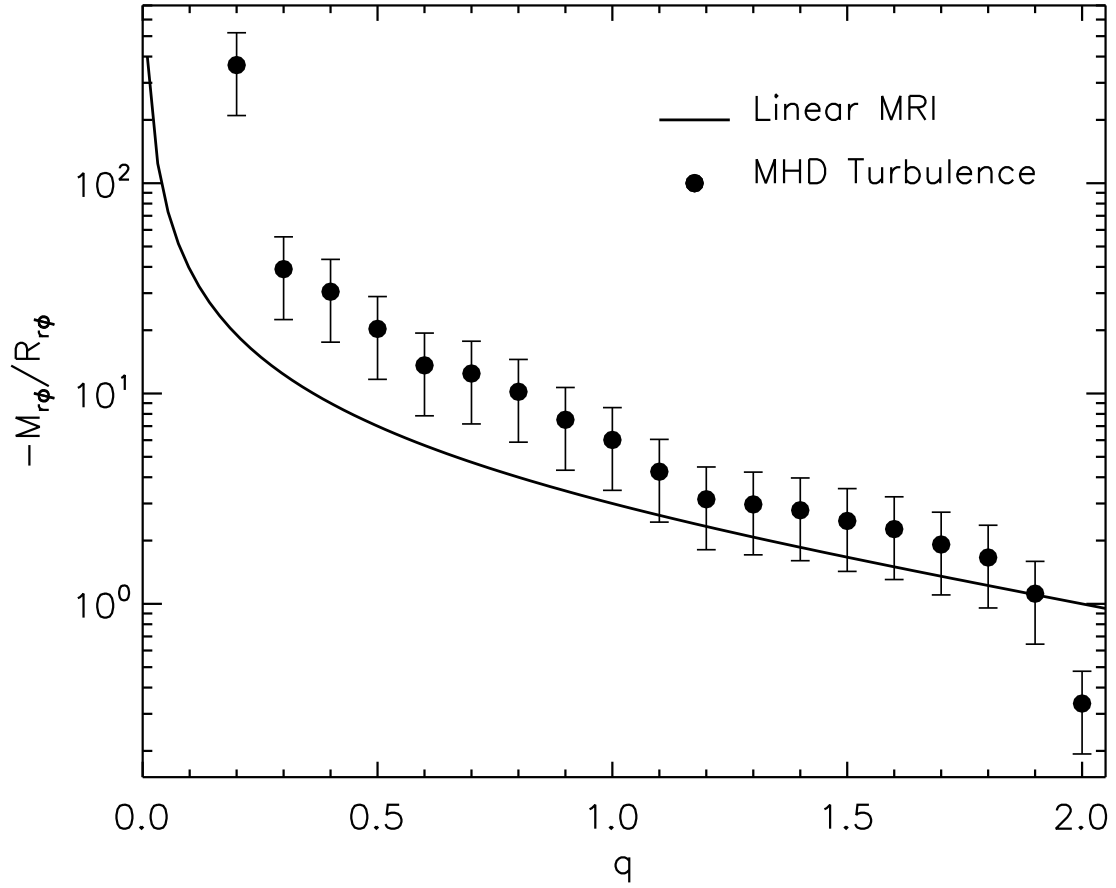


Figure 3.4 The dependence of the ratio of the mean Maxwell to the mean Reynolds stresses, $-\bar{M}_{r\phi}/\bar{R}_{r\phi}$, on the shear parameter q . The data points correspond to the results of shearing box simulations by Hawley, Balbus, & Winters (1999) in the saturated state. The *solid line* shows the analytic result (eq. [3.84]) for the ratio of the mean stresses during the late time of the exponential growth of the MRI.

the stresses at saturation as a function of the shear parameter q seems also to be similar to that obtained at late times during the linear phase of the instability.

The simultaneous analysis of Figures 3.3 and 3.4 demonstrates that the ratio $-\bar{M}_{r\phi}/\bar{R}_{r\phi}$ during the turbulent saturated state in local simulations of accretion disks is determined almost entirely by the local shear and depends very weakly on the other properties of the flow or the initial conditions. These figures also show that the ratios of the Maxwell to the Reynolds stresses calculated during the turbulent saturated state are qualitatively similar to the corresponding ratios found during the late times of the linear phase of the instability, even though the latter are slightly lower (typically by a factor of 2). This is remarkable because, when deriving equation (3.84) we have assumed that the MHD fluid is incompressible and considered only fluctuations that depend on the vertical, z , coordinate. Moreover, in the spirit of the linear analysis, we have not incorporated energy cascades between different scales, neither did we consider dissipation or reconnection processes that lead to saturation. Of course, the numerical simulations addressing the non-linear regime of the instability do not suffer from any of the approximations invoked to solve for the temporal evolution of the stresses during the phase of exponential growth. Nevertheless, the ratio of the Maxwell to the Reynolds stresses that characterize the turbulent saturated state are similar (to within factors of order unity) to the ratios characterizing the late times of the linear phase of the instability.

CHAPTER 4

A MODEL FOR ANGULAR MOMENTUM TRANSPORT IN ACCRETION DISKS
DRIVEN BY THE MAGNETOROTATIONAL INSTABILITY

In this Chapter, we develop a local model for the exponential growth and saturation of the Reynolds and Maxwell stresses in turbulent flows driven by the magnetorotational instability. We first derive equations that describe the effects of the instability on the growth and pumping of the stresses. We highlight the relevance of a new type of correlation that couples the dynamical evolution of the Reynolds and Maxwell stresses and plays a key role in developing and sustaining the magnetorotational turbulence. We then supplement these equations with a phenomenological description of the triple correlations that lead to a saturated turbulent state. We show that the steady-state limit of the model describes successfully the correlations among stresses found in numerical simulations of shearing boxes.

4.1 Introduction

Since the early days of accretion disk theory, it has been recognized that molecular viscosity cannot account for a number of observational properties of accreting objects. Shakura & Sunyaev (1973) introduced a parametrization of the shear stress that has been widely used since. Much of the success of their model lies on the fact that many disk observables are determined mostly by energy balance and depend weakly on the adopted prescription (Balbus & Papaloizou, 1999). However, this parametrization leaves unanswered fundamental questions on the origin of the anomalous transport and its detailed characteristics.

Strong support for the relevance of magnetic fields in accretion disks arose

with the realization that differentially rotating flows with radially decreasing angular velocities are unstable when threaded by weak magnetic fields (Balbus & Hawley, 1991, 1998). Since the discovery of this magnetorotational instability (MRI), a variety of local (Hawley, Gammie, & Balbus, 1995, 1996; Sano, Inutsuka, Turner, & Stone, 2004) and global (Hawley, 2000, 2001; Stone & Pringle, 2001; Hawley & Krolik, 2001) numerical simulations have confirmed that its long-term evolution gives rise to a sustained turbulent state and outward angular momentum transport. However, global simulations also demonstrate that angular momentum transfer in turbulent accretion disks cannot be adequately described by the Shakura & Sunyaev prescription. In particular, there is evidence that the turbulent stresses are not proportional to the local shear (Abramowicz, Brandenburg, & Lasota, 1996) and are not even determined locally (Armitage, 1998).

Some attempts to eliminate these shortcomings have been made within the formalism of mean-field magnetohydrodynamics (Krause & Rädler, 1980). This has been a fruitful approach for modeling the growth of mean magnetic fields in differentially rotating media (Brandenburg & Subramanian, 2005). However, it has proven difficult to use a dynamo model to describe the transport of angular momentum in these systems (Blackman, 2001; Brandenburg, 2005). This is especially true in turbulent flows driven by the MRI, where the fluctuations in the magnetic energy are larger than the mean magnetic energy, and the turbulent velocity and magnetic fields evolve simultaneously (Balbus & Hawley, 1991, 1998).

In order to overcome this difficulty various approaches have been taken in different physical setups. Blackman & Field (2002) derived a dynamical model for the nonlinear saturation of helical turbulence based on a damping closure for the electromotive force in the absence of shear. On the other hand, Kato and

Yoshizawa (see, e.g., Kato & Yoshizawa 1993, 1995; Kato, Fukue, & Mineshige 1998) and Ogilvie (2003) derived a set of closed dynamical equations that describe the growth and saturation of the Reynolds and Maxwell stresses in shearing flows in the absence of mean magnetic fields.

In this chapter, we relax some of the key assumptions made in previous works and develop the first local model for the dynamical evolution of the Reynolds and Maxwell tensors in turbulent magnetized accretion disks that explicitly incorporates the MRI as their source.

4.2 A Model for MHD Turbulent Pumping by the MRI

The equation describing the dynamical evolution of the mean angular momentum density, \bar{l} , of a fluid element in an accretion disk with tangled magnetic fields is

$$\partial_t \bar{l} + \nabla \cdot (\bar{l} \bar{\mathbf{v}}) = -\nabla \cdot (r \bar{\mathcal{F}}). \quad (4.1)$$

Here, the over-bars denote properly averaged values, $\bar{\mathbf{v}}$ is the mean flow velocity, and the vector $\bar{\mathcal{F}}$ characterizes the flux of angular momentum. Its radial component, $\bar{\mathcal{F}}_r \equiv \bar{R}_{r\phi} - \bar{M}_{r\phi}$, is equal to the total stress acting on a fluid element. The stresses due to correlations in the velocity field, $\bar{R}_{r\phi} \equiv \langle \rho \delta v_r \delta v_\phi \rangle$, and magnetic field fluctuations, $\bar{M}_{r\phi} \equiv \langle \delta B_r \delta B_\phi \rangle / 4\pi$, are the Reynolds and Maxwell stresses, respectively. A self-consistent accretion disk model based on the solution of the equations for the mean velocities requires a closed system of equations for the temporal evolution of these mean stresses.

In a recent paper (Pessah, Chan, & Psaltis, 2006a), we identified the signature of the magnetorotational instability in the mean Maxwell and Reynolds stresses due to correlated fluctuations of the form $\delta \mathbf{v} = [\delta v_r(t, z), \delta v_\phi(t, z), 0]$ and $\delta \mathbf{B} = [\delta B_r(t, z), \delta B_\phi(t, z), 0]$ in an incompressible, cylindrical, differentially rotating flow,

threaded by a mean vertical magnetic field, \bar{B}_z . We demonstrated that a number of properties of the mean stresses during the initial phase of exponential growth of the MRI are approximately preserved in the saturated state reached in local three-dimensional numerical simulations. As a first step in our calculation, we aim to derive dynamical equations for the mean stresses that describe this result.

In order to work with dimensionless variables we consider the characteristic time- and length-scales set by $1/\Omega_0$ and \bar{v}_{Az}/Ω_0 . Here, Ω_0 and $\bar{v}_{Az} = \bar{B}_z/\sqrt{4\pi\rho_0}$ denote the local values of the angular frequency and the (vertical) Alfvén speed in the disk with local density ρ_0 at the fiducial radius r_0 . The equations governing the local dynamics of the (dimensionless) MRI-driven fluctuations in Fourier space, are then given by (Pessah, Chan, & Psaltis, 2006a),

$$\partial_t \delta \hat{v}_r = 2\delta \hat{v}_\phi + ik_n \delta \hat{b}_r, \quad (4.2)$$

$$\partial_t \delta \hat{v}_\phi = (q - 2)\delta \hat{v}_r + ik_n \delta \hat{b}_\phi, \quad (4.3)$$

$$\partial_t \delta \hat{b}_r = ik_n \delta \hat{v}_r, \quad (4.4)$$

$$\partial_t \delta \hat{b}_\phi = -q\delta \hat{b}_r + ik_n \delta \hat{v}_\phi, \quad (4.5)$$

where $\delta \hat{v}_i$ and $\delta \hat{b}_i$ stand for the Fourier transform of the dimensionless physical fluctuations $\delta v_i/\bar{v}_{Az}$ and $\delta B_i/\bar{B}_z$. The wavenumber, k_n , denotes the mode with n nodes in the vertical direction and the parameter $q \equiv -d \ln \Omega / d \ln r|_{r_0}$ is a measure of the local shear.

Using the fact that the modes with vertical wavevectors dominate the fast growth driven by the MRI, we obtain a set of equations to describe the initial exponential growth of the Reynolds and Maxwell stresses. We start from the equations for the fluctuations (4.2)–(4.5) and use the fact that the mean value of the product of two functions f and g , with zero means, is given by (Pessah, Chan,

& Psaltis 2006a; see also chapter 3),

$$\langle fg \rangle(t) \equiv 2 \sum_{n=1}^{\infty} \text{Re}[\hat{f}(k_n, t) \hat{g}^*(k_n, t)] . \quad (4.6)$$

By combining different moments of equations (4.2)–(4.5) we obtain the dimensionless set

$$\partial_t \bar{R}_{rr} = 4\bar{R}_{r\phi} + 2\bar{W}_{r\phi} , \quad (4.7)$$

$$\partial_t \bar{R}_{r\phi} = (q-2)\bar{R}_{rr} + 2\bar{R}_{\phi\phi} - \bar{W}_{rr} + \bar{W}_{\phi\phi} , \quad (4.8)$$

$$\partial_t \bar{R}_{\phi\phi} = 2(q-2)\bar{R}_{r\phi} - 2\bar{W}_{\phi r} , \quad (4.9)$$

$$\partial_t \bar{M}_{rr} = -2\bar{W}_{r\phi} , \quad (4.10)$$

$$\partial_t \bar{M}_{r\phi} = -q\bar{M}_{rr} + \bar{W}_{rr} - \bar{W}_{\phi\phi} , \quad (4.11)$$

$$\partial_t \bar{M}_{\phi\phi} = -2q\bar{M}_{r\phi} + 2\bar{W}_{\phi r} , \quad (4.12)$$

where we have defined the tensor \bar{W}_{ij} with components

$$\bar{W}_{rr} \equiv \langle \delta v_r \delta j_r \rangle = \langle \delta b_\phi \delta \omega_\phi \rangle , \quad (4.13)$$

$$\bar{W}_{r\phi} \equiv \langle \delta v_r \delta j_\phi \rangle = -\langle \delta b_r \delta \omega_\phi \rangle , \quad (4.14)$$

$$\bar{W}_{\phi r} \equiv \langle \delta v_\phi \delta j_r \rangle = -\langle \delta b_\phi \delta \omega_r \rangle , \quad (4.15)$$

$$\bar{W}_{\phi\phi} \equiv \langle \delta v_\phi \delta j_\phi \rangle = \langle \delta b_r \delta \omega_r \rangle . \quad (4.16)$$

Here, δj_i and $\delta \omega_i$, for $i = r, \phi$, stand for the components of the induced current $\delta \mathbf{j} = \nabla \times \delta \mathbf{b}$ and vorticity $\delta \boldsymbol{\omega} = \nabla \times \delta \mathbf{v}$ fluctuations. Note that the components of the tensor \bar{W}_{ij} are defined in terms of the correlations between the velocity and current fields. However, for the case under consideration, these are identical to the corresponding correlations between the magnetic field and vorticity fluctuations (eqs. [4.13]–[4.16]).

Equations (4.7)–(4.12) show that the MRI-driven growth of the Reynolds and Maxwell tensors can be described formally *only* via the correlations \bar{W}_{ij} that con-

nect the equations for their temporal evolution. Note that, in contrast to the correlations $\langle \delta v_i \delta \omega_k \rangle$ and $\langle \delta b_i \delta j_k \rangle$, that appear naturally in helical dynamo modeling and transform as tensor densities (i.e., as the product of a vector and an axial vector), the correlations $\langle \delta v_i \delta j_k \rangle$ and $\langle \delta b_i \delta \omega_k \rangle$ transform as tensors. Moreover, the tensor \bar{W}_{ij} cannot be recast in terms of the cross-helicity tensor $\bar{H}_{ij} \equiv \langle \delta v_i \delta b_j \rangle$ because, for the unstable MRI modes, the ratio $\bar{H}_{ij}/\bar{W}_{ij}$ approaches zero at late times. Neither can \bar{W}_{ij} be expressed in terms of the turbulent electromotive force $\langle \delta \mathbf{v} \times \delta \mathbf{b} \rangle$, as the latter vanishes under our set of assumptions, implying that no mean magnetic field is generated.

In order to describe the MRI-driven exponential growth of the stresses in equations (4.7)–(4.12) we need to write an additional set of dynamical equations for the evolution of the tensor \bar{W}_{ij} . Using appropriate combinations of different moments of equations (4.2)–(4.5) we obtain

$$\partial_t \bar{W}_{rr} = q \bar{W}_{r\phi} + 2 \bar{W}_{\phi r} + (\bar{k}_{r\phi}^R)^2 \bar{R}_{r\phi} - (\bar{k}_{r\phi}^M)^2 \bar{M}_{r\phi}, \quad (4.17)$$

$$\partial_t \bar{W}_{r\phi} = 2 \bar{W}_{\phi\phi} - (\bar{k}_{rr}^R)^2 \bar{R}_{rr} + (\bar{k}_{rr}^M)^2 \bar{M}_{rr}, \quad (4.18)$$

$$\partial_t \bar{W}_{\phi r} = (q - 2) \bar{W}_{rr} + q \bar{W}_{\phi\phi} + (\bar{k}_{\phi\phi}^R)^2 \bar{R}_{\phi\phi} - (\bar{k}_{\phi\phi}^M)^2 \bar{M}_{\phi\phi}, \quad (4.19)$$

$$\partial_t \bar{W}_{\phi\phi} = (q - 2) \bar{W}_{r\phi} - (\bar{k}_{r\phi}^R)^2 \bar{R}_{r\phi} + (\bar{k}_{r\phi}^M)^2 \bar{M}_{r\phi}, \quad (4.20)$$

where we have defined the set of mean wavenumbers

$$(\bar{k}_{ij}^R)^2 \equiv \frac{\sum_{n=1}^{\infty} k_n^2 \text{Re}[\delta \hat{v}_i \delta \hat{v}_j^*]}{\sum_{n=1}^{\infty} \text{Re}[\delta \hat{v}_i \delta \hat{v}_j^*]}, \quad (4.21)$$

and

$$(\bar{k}_{ij}^M)^2 \equiv \frac{\sum_{n=1}^{\infty} k_n^2 \text{Re}[\delta \hat{b}_i \delta \hat{b}_j^*]}{\sum_{n=1}^{\infty} \text{Re}[\delta \hat{b}_i \delta \hat{b}_j^*]}. \quad (4.22)$$

4.3 A Model for the Saturation of MRI-driven Turbulence

The system of equations (4.7)–(4.12) and (4.17)–(4.20) describes the temporal evolution of the stresses during the exponential growth of the MRI in a way that is formally correct, with no approximations. Motivated by the similarity between the ratios of the stresses during the exponential growth of the MRI and during the saturated turbulent state (Pessah, Chan, & Psaltis, 2006a), we propose to use the right-hand sides of equations (4.7)–(4.12) and (4.17)–(4.20) as a local model for the source of turbulence in MRI-driven magnetohydrodynamic flows. Of course, in the turbulent regime, the various average wavenumbers $\bar{k}_{ij}^{R,M}$ will depend on the spectrum of velocity and magnetic field fluctuations. As the lowest order model for these wavenumbers we choose

$$(\bar{k}_{ij}^{R,M})^2 = \zeta^2 k_{\max}^2 = \zeta^2 \left(q - \frac{q^2}{4} \right) \quad \text{for } i, j = r, \phi, \quad (4.23)$$

where ζ is a parameter of order unity and k_{\max} corresponds to the wavenumber at which the growth rate of the *fluctuations* reaches its maximum value, $\gamma_{\max} \equiv q/2$.

By construction, the set of equations (4.7)–(4.12) and (4.17)–(4.20) leads to the expected exponential growth of the mean stresses driven by modes with wavevectors perpendicular to the disk midplane. These modes, however, are known to be subject to parasitic instabilities, which transfer energy to modes in the perpendicular (k_r, k_ϕ) directions (Goodman & Xu, 1994). The initial fast growth experienced by the stresses will eventually be slowed down by the combined effects of non-linear couplings between modes and of dissipation at the smallest scales of interest.

The terms accounting for these interactions would appear in the equations for the stresses as triple correlations between components of the velocity and magnetic fields, i.e., they would be of the form $\langle \delta v_i \delta v_j \delta b_k \rangle$ and $\langle \delta v_i \delta b_j \delta b_k \rangle$. These types

of non-linear terms have also been considered by Ogilvie (2003), who proposed scalings of the form

$$\langle \delta v_i \delta v_j \delta b_k \rangle \sim \langle \delta v_i \delta v_j \rangle \langle \delta b_k \delta b_k \rangle^{1/2} \sim \bar{M}_{kk}^{1/2} \bar{R}_{ij}. \quad (4.24)$$

In the absence of a detailed model for these correlations and motivated again by the similarity of the stress properties during the exponential growth of the MRI and the saturated turbulent state (Pessah, Chan, & Psaltis, 2006a), we introduce a phenomenological description of the non-linear effects on the evolution of the various stresses. In particular, denoting by \bar{X}_{ij} the ij -component of any one of the three tensors, i.e., \bar{R}_{ij} , \bar{M}_{ij} , or \bar{W}_{ij} , we add to the equation for the temporal evolution of that component the sink term¹

$$\left. \frac{\partial \bar{X}_{ij}}{\partial t} \right|_{\text{sink}} \equiv -\sqrt{\frac{\bar{M}}{\bar{M}_0}} \bar{X}_{ij}. \quad (4.25)$$

Here, $\bar{M}/2 = (\bar{M}_{rr} + \bar{M}_{\phi\phi})/2$ is the mean magnetic energy density in the fluctuations and \bar{M}_0 is a parameter.

Adding the sink terms to the system of equations (4.7)–(4.12) and (4.17)–(4.20) leads to a saturation of the stresses after a few characteristic timescales, *preserving* the ratio of the various stresses to the value determined by the exponential growth due to the MRI and characterized by the parameter ζ . These non-linear terms dictate only the saturated level of the mean magnetic energy density according to $\lim_{t \rightarrow \infty} \bar{M} = \Gamma^2 \bar{M}_0$, where Γ is the growth rate for the *stresses*, which, in the case of a Keplerian disk, with $q = 3/2$, is given by

$$\Gamma^2 = 2 \left[\sqrt{1 + 15\zeta^2} - (1 + 15\zeta^2/8) \right]. \quad (4.26)$$

We infer the dependence of the energy density scale $\bar{M}_0/2$ on the four characteristic scales in the problem Ω_0 , H (the vertical length of the box), ρ_0 , and \bar{v}_{Az}

¹The complete set of equations is explicitly written in §5.3.3

using dimensional analysis. We obtain

$$\bar{M}_0/2 \propto \rho_0 H^\delta \Omega_0^\delta \bar{v}_{Az}^{2-\delta} \quad (4.27)$$

which leads, with the natural choice $\delta = 1$, to (in dimensional quantities)

$$\bar{M}_0/2 \equiv \xi \rho_0 H \Omega_0 \bar{v}_{Az}, \quad (4.28)$$

where we have introduced the parameter ξ .

Our expression for \bar{M}_0 describes the same scaling between the magnetic energy density during saturation and the various parameters characterizing the disk (ρ_0 , H , Ω_0 , and \bar{v}_{Az}) found in a series of shearing box simulations threaded by a finite vertical magnetic field and with a Keplerian shearing profile (Hawley, Gammie, & Balbus, 1995, 1996). By performing a numerical study of the late-time solutions of the proposed model, we found a unique set of values (ζ, ξ) such that its asymptotic limit describes the correlations found in these numerical simulations.

Figure 4.1 shows the correlations between the $r\phi$ -components of the Maxwell and Reynolds stresses and the mean magnetic energy density found during the saturated state in numerical simulations (Hawley, Gammie, & Balbus, 1995, 1996). In our model, this ratio depends only on the parameter ζ and the shear q (held fixed at $q = 3/2$ in the simulations). It is evident that, in the numerical simulations, the ratios of the stresses to the magnetic energy density are also practically independent of any of the initial parameters in the problem that determine the magnetic energy density during saturation (i.e., the x -axis in the plot). This is indeed why we required for our model of saturation to preserve the stress ratios that are determined during the exponential phase of the MRI. Assigning the same fractional uncertainty to all the numerical values for the stresses, our model describes both correlations simultaneously for $\zeta = 0.3$.

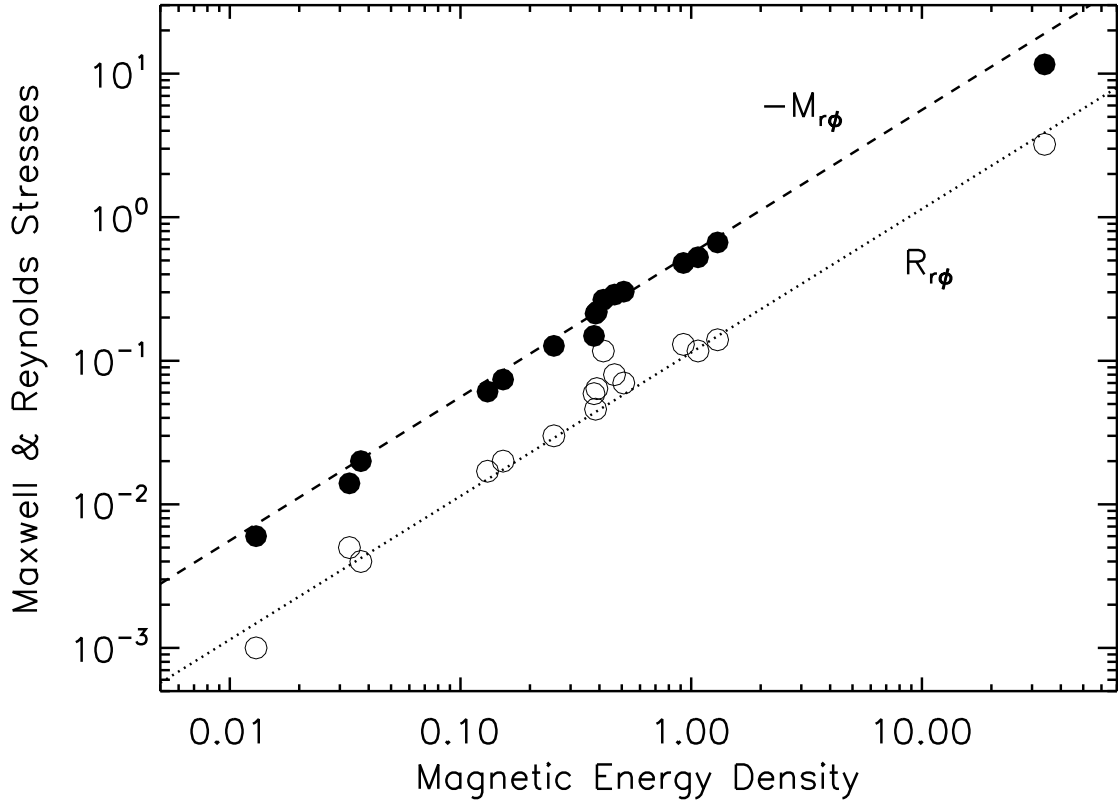


Figure 4.1 Correlations between the Maxwell and Reynolds stresses and mean magnetic energy density at saturation in MRI-driven turbulent shearing boxes (Hawley, Gammie, & Balbus, 1995, 1996). The lines show the result obtained with our model in the asymptotic limit for $\zeta = 0.3$.

Figure 4.2 shows the mean magnetic energy density in terms of a saturation predictor found in numerical simulations (Hawley, Gammie, & Balbus, 1995, 1996). For $\zeta = 0.3$ and assigning the same fractional uncertainty to all the numerical values for the stresses, we obtain the best fit for $\xi = 11.3$. These values for the parameters complete the description of our model.

4.4 Discussion

In summary, in this chapter we developed a local model for the evolution and saturation of the Reynolds and Maxwell stresses in MRI-driven turbulent flows. The model is formally complete when describing the initial exponential growth and pumping of the MRI-driven stresses and, thus, satisfies, by construction, all the mathematical requirements described by Ogilvie (2003). Although it is based on the absolute minimum physics (shear, uniform \bar{B}_z , $2D$ -fluctuations) for the MRI to be at work, the model is able, in its asymptotic limit, to recover successfully the correlations found in three-dimensional local numerical simulations (Hawley, Gammie, & Balbus, 1995, 1996).

Finally, the local model described here contains an unexpected feature. The mean magnetic field in the vertical direction couples the Reynolds and Maxwell stresses via the correlations between the fluctuations in the velocity field and the fluctuating currents generated by the perturbations in the magnetic field. These second order correlations, that we denoted by the tensor \bar{W}_{ij} , play a crucial role in driving the exponential growth of the mean stresses and energy densities observed in numerical simulations. To our knowledge this is the first time that their relevance has been pointed out in either the context of dynamo theory or MRI-driven turbulence.

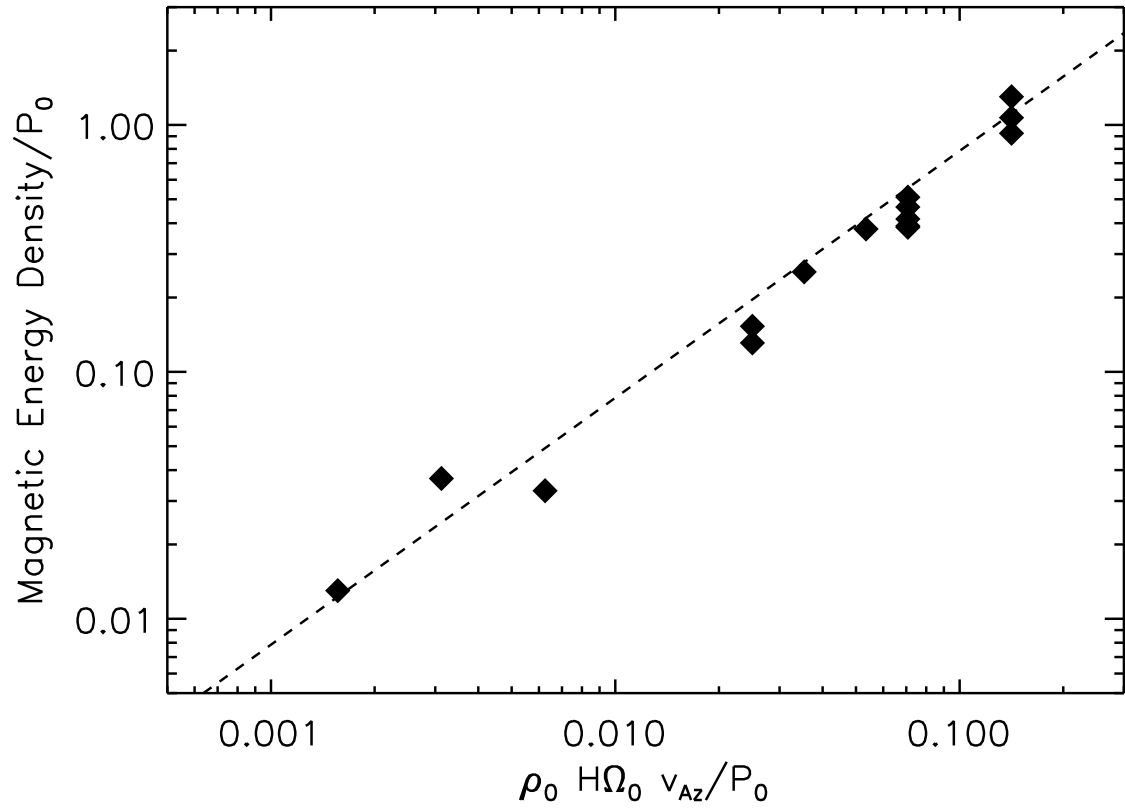


Figure 4.2 The mean magnetic energy density in terms of a saturation predictor found at late times in numerical simulations of MRI-driven turbulence (Hawley, Gammie, & Balbus, 1995, 1996). The line shows the result obtained with our model in the asymptotic limit for $\zeta = 0.3$ and $\xi = 11.3$.

CHAPTER 5

THE FUNDAMENTAL DIFFERENCE BETWEEN ALPHA-VISCOSITY AND
TURBULENT MAGNETOROTATIONAL STRESSES

Numerical simulations of turbulent, magnetized, differentially rotating flows driven by the magnetorotational instability are often used to calculate the effective values of alpha viscosity that is invoked in analytical models of accretion disks. In this chapter we use various dynamical models of turbulent magnetohydrodynamic stresses as well as numerical simulations of shearing boxes to show that angular momentum transport in accretion disks cannot be described by the alpha model. In particular, we demonstrate that turbulent magnetorotational stresses are not linearly proportional to the local shear and vanish identically for angular velocity profiles that increase outwards.

5.1 Introduction

It has long been recognized that molecular viscosity cannot be solely responsible for angular momentum transport in accretion disks. Shakura & Sunyaev (1973) offered an appealing solution to this problem by postulating a source of enhanced viscosity due to turbulence and magnetic fields. The standard accretion disk model rests on the idea that the stresses between adjacent disk annuli are proportional to the local shear, as in a Newtonian laminar shear flow, but that it is the interaction of large turbulent eddies that results in efficient transport. The idea that angular momentum transport in accretion disks can be described in terms of an enhanced version of shear-driven transport in (laminar) differentially rotating media has been at the core of the majority of studies in accretion disk theory and phenomenology ever since (see, e.g., Frank, King, & Raine, 2002).

The origin of the turbulence that leads to enhanced angular momentum transport in accretion disks has been a matter of debate since the work of Shakura & Sunyaev (1973). The issue of whether hydrodynamic turbulence can be generated and sustained in astrophysical disks, due to the large Reynolds numbers involved, is currently a matter of renewed interest (Afshordi, Mukhopadhyay, & Narayan, 2005; Mukhopadhyay, Afshordi, & Narayan, 2005). However, this idea has long been challenged by analytical (Ryu & Goodman, 1992; Balbus & Hawley, 2006), numerical (Stone & Balbus, 1996; Balbus, Hawley, & Stone, 1996; Balbus & Hawley, 1997; Hawley, Balbus, & Winters, 1999), and, more recently, experimental work (Ji, Burin, Scharfman, & Goodman, 2006).

During the last decade, it has become evident that the interplay between turbulence and magnetic fields is at a more fundamental level than originally conceived. There is now strong theoretical and numerical evidence suggesting that the process driving turbulence is related to a magnetic instability that operates in the presence of a radially decreasing angular velocity profile. Since the appreciation of the relevance of this magnetorotational instability (MRI) to accretion physics (Balbus & Hawley 1991; see Balbus & Hawley 1998 and Balbus 2003 for a more recent review), a variety of local (Hawley, Gammie, & Balbus, 1995, 1996; Stone, Hawley, Gammie, & Balbus, 1996; Brandenburg, Nordlund, Stein, & Torkelsson, 1995; Brandenburg, 2001; Sano, Inutsuka, Turner, & Stone, 2004) and global (Armitage, 1998; Hawley, 2000, 2001; Hawley & Krolik, 2001; Stone & Pringle, 2001) numerical simulations have revealed that its long-term evolution gives rise to a turbulent state and provides a natural avenue for vigorous angular momentum transport.

The fact that the overall energetic properties of turbulent magnetohydrodynamic (MHD) accretion disks are similar to those of viscous accretion disks (Bal-

bus & Papaloizou, 1999) has lead to the notion that angular momentum transport due to MRI-driven turbulence in rotating shearing flows can be described in terms of the alpha model proposed by Shakura & Sunyaev (1973). This, in turn, has motivated many efforts aimed to computing effective alpha values from numerical simulations (see, e.g., Gammie, 1998; Brandenburg, 1998, and references therein) in order to use them in large scale analytical models of accretion disks.

In this chapter, we address in detail how the transport of angular momentum mediated by MHD turbulence depends on the magnitude of the local shear and contrast this result to the standard model for shear viscosity. We find that one of the fundamental assumptions in which the standard viscous disk model is based, i.e., that angular momentum transport is linearly proportional to the local shear, is not appropriate for describing turbulent MRI-driven accretion disks.

5.2 Alpha Viscosity vs. MHD Stresses

The equation describing the dynamical evolution of the mean angular momentum density of a fluid element, \bar{l} , in an axisymmetric turbulent MHD accretion disk with tangled magnetic fields is

$$\frac{\partial \bar{l}}{\partial t} + \frac{1}{r} \frac{\partial}{\partial r} (r \bar{l} \bar{v}_r) = -\frac{1}{r} \frac{\partial}{\partial r} (r^2 \bar{T}_{r\phi}). \quad (5.1)$$

Here, the over-bars denote properly averaged values (see, e.g., Balbus & Hawley, 1998; Balbus & Papaloizou, 1999), \bar{v}_r is the radial mean flow velocity, and the quantity $\bar{T}_{r\phi}$ represents the total stress

$$\bar{T}_{r\phi} \equiv \bar{R}_{r\phi} - \bar{M}_{r\phi} \quad (5.2)$$

acting on a fluid element as a result of the correlated fluctuations in the velocity and magnetic fields in the turbulent flow, i.e.,

$$\bar{R}_{r\phi} \equiv \langle \rho \delta v_r \delta v_\phi \rangle, \quad (5.3)$$

$$\bar{M}_{r\phi} \equiv \frac{\langle \delta B_r \delta B_\phi \rangle}{4\pi}, \quad (5.4)$$

where $\bar{R}_{r\phi}$ and $\bar{M}_{r\phi}$ stand for the $r\phi$ -components of the Reynolds and Maxwell stress tensors, respectively.

Equation (5.1) highlights the all-important role played by correlated velocity and magnetic-field fluctuations in turbulent accretion disks; if they vanish, the mean angular momentum density of a fluid element is conserved. In order for matter in the bulk of the disk to accrete, i.e., to lose angular momentum, the sign of the mean total stress must be positive. Note that the potential for correlated kinetic fluctuations to transport angular momentum in unmagnetized disks is still present in the hydrodynamic version of equation (5.1). However, as noted by Balbus & Hawley (1997, 1998), the dynamical role played by the correlated velocity fluctuations in hydrodynamic flows is radically different from the corresponding role played by correlated velocity and magnetic field fluctuations in MHD flows, even when the magnetic fields involved are weak.

In order to calculate the structure of an accretion disk for which angular momentum transported is described by equation (5.1), it is necessary to obtain a closed system of equations for the second-order correlations defining the total stress $\bar{T}_{r\phi}$. In this context, the original proposal by Shakura and Sunyaev (see also, Lynden-Bell & Pringle, 1974) can be seen as a simple closure scheme for the correlations defining the total turbulent stress in terms of mean flow variables. The model for angular momentum transport on which the standard accretion disk is based rests on two distinct assumptions. First, it is postulated that the vertically averaged stress exerted on any given disk annulus can be modeled as a

shear viscous stress (Lynden-Bell & Pringle, 1974), i.e., in cylindrical coordinates,

$$\bar{T}_{r\phi}^v \equiv -r\Sigma\nu_{\text{turb}}\frac{d\Omega}{dr}, \quad (5.5)$$

where Σ and Ω stand for the vertically integrated disk density and the angular velocity at the radius r , respectively. This is the Newtonian model for the viscous stress between adjacent layers in a differentially rotating laminar flow (Landau & Lifshitz, 1959); the coefficient ν_{turb} describes in this case the turbulent kinematic viscosity. In this model, the direction of angular momentum transport is always opposite to the angular velocity gradient. This is the essence of a shear viscous disk.

Second, on dimensional grounds, it is assumed that the viscosity coefficient is given by $\nu_{\text{turb}} \equiv \alpha c_s H$. This is because the physical mechanism that allows for angular momentum transport is envisaged as the result of the interaction of turbulent eddies of typical size equal to the disk scale-height, H , on a turnover time of the order of H/c_s , where c_s is the isothermal sound speed. The parameter alpha is often assumed to be constant and smaller than unity. In the presence of a shearing background, the vertically integrated stress is then given by

$$\bar{T}_{r\phi}^v = -\alpha P \frac{d \ln \Omega}{d \ln r}, \quad (5.6)$$

where $P = \Sigma c_s^2$ stands for the average pressure and we have used the fact that the scale-height of a thin disk in vertical hydrostatic equilibrium is roughly $H \sim c_s/\Omega$. This parameterization of the coefficient of turbulent kinematic viscosity implies that the efficiency with which angular momentum is transported is proportional to the local average pressure. This is the idea behind the standard alpha-disk model.

Note that the expression usually employed to define the stress in alpha-models, i.e., $\bar{T}_{r\phi}^v = \alpha P$, only provides the correct order of magnitude for the stress in terms

of the pressure for a Keplerian disk. Indeed, in this case, the shear parameter is $q \equiv -d \ln \Omega / d \ln r = 3/2 \sim 1$. However, the fact that the viscous stress is proportional to the local shear cannot be overlooked for regions of the disk where the local angular velocity can differ significantly from its Keplerian value. This is expected to be the case in the boundary layer around an accreting star or close to the marginally stable orbit around a black hole. These inner disk regions are locally characterized by different, and possibly negative, shearing parameters q . It is important to emphasize that, if the explicit dependence of the stress on the local shear is not considered then equation (5.6) predicts unphysical, non-vanishing stresses for solid body rotation, $q \equiv 0$ (c.f., Blaes, 2004).

More than a decade after the paper by Balbus & Hawley (1991), the MRI stands as the most promising driver of the turbulence thought to enable the accretion process. It is important to note, however, that there is no a priori reason to assume that the correlated fluctuations defining the total turbulent stress in MRI-driven turbulence are linearly proportional to the local shear. In fact, this assumption can be challenged on both theoretical and numerical grounds.

5.3 Predictions from Stress Modeling

There are currently few models that aim to describe the local dynamics of turbulent stresses in differentially rotating magnetized media by means of high-order closure schemes (Kato & Yoshizawa, 1993, 1995; Ogilvie, 2003; Pessah, Chan, & Psaltis, 2006b)¹. In these models, the total stress, $\bar{T}_{r\phi} = \bar{R}_{r\phi} - \bar{M}_{r\phi}$, is not prescribed, as in equation (5.6), but its value is calculated considering the local energetics of the turbulent flow. This is achieved by deriving a set of non-linear cou-

¹The studies described here concern models for the evolution of the various correlated fluctuations relevant for describing the dynamics of a turbulent magnetized flow. We note that Vishniac & Brandenburg (1997) proposed an incoherent dynamo model for the transport of angular momentum driven by the generation of large-scale radial and toroidal magnetic fields.

pled equations for the various components of the Reynolds and Maxwell stress tensors. These equations involve unknown triple-order correlations among fluctuations making necessary the addition of ad hoc closure relations.

Although the available models differ on the underlying physical mechanisms that drive the turbulence and lead to saturation, some important characteristics of the steady flows that they describe are qualitatively similar. In particular, all of the models predict that turbulent kinetic/magnetic cells in magnetized Keplerian disks are elongated along the radial/azimuthal direction, i.e., $\bar{R}_{rr} > \bar{R}_{\phi\phi}$ while $\bar{M}_{\phi\phi} > \bar{M}_{rr}$. Furthermore, turbulent angular momentum transport is mainly carried by correlated magnetic fluctuations, rather than by their kinetic counterpart, i.e., $-\bar{M}_{r\phi} > \bar{R}_{r\phi}$. These properties are in general agreement with local numerical simulations. However, a distinctive quantitative feature of these models that concerns us here is that they make rather different predictions for how the stresses depend on the magnitude and sign of the angular velocity profile.

In the remainder of this section, we highlight the most relevant physical properties characterizing the various models and assess the functional dependence of the total stress, $\bar{T}_{r\phi}$, on the sign and steepness of the local angular velocity profile. For convenience, we summarize in Appendix A the various sets of equations that define each of the models.

5.3.1 Kato & Yoshizawa 1995

In a series of papers, Kato & Yoshizawa (1993, 1995) developed a model for hydromagnetic turbulence in accretion disks with no large scale magnetic fields (see Kato, Fukue, & Mineshige, 1998, for a review, and Nakao 1997 for the inclusion of large scale radial and toroidal fields). In their closure scheme, triple-order correlations among fluctuations in the velocity and magnetic fields are modeled in terms of second-order correlations using the two-scale direct interaction ap-

proximation (Yoshizawa, 1985; Yoshizawa, Itoh, & Itoh, 2003), as well as mixing length concepts. The temporal evolution of the Reynolds and Maxwell stresses is described by

$$\partial_t \bar{R}_{rr} = 4\bar{R}_{r\phi} + \bar{\Pi}_{rr} - \bar{S}_{rr} - \frac{2}{3}\epsilon_G, \quad (5.7)$$

$$\partial_t \bar{R}_{r\phi} = (q-2)\bar{R}_{rr} + 2\bar{R}_{\phi\phi} + \bar{\Pi}_{r\phi} - \bar{S}_{r\phi}, \quad (5.8)$$

$$\partial_t \bar{R}_{\phi\phi} = 2(q-2)\bar{R}_{r\phi} + \bar{\Pi}_{\phi\phi} - \bar{S}_{\phi\phi} - \frac{2}{3}\epsilon_G, \quad (5.9)$$

$$\partial_t \bar{R}_{zz} = \bar{\Pi}_{zz} - \bar{S}_{zz} - \frac{2}{3}\epsilon_G, \quad (5.10)$$

$$\partial_t \bar{M}_{rr} = \bar{S}_{rr} - 2\beta\bar{M}_{rr} - \frac{2}{3}\epsilon_M, \quad (5.11)$$

$$\partial_t \bar{M}_{r\phi} = -q\bar{M}_{rr} + \bar{S}_{r\phi} - 2\beta\bar{M}_{r\phi}, \quad (5.12)$$

$$\partial_t \bar{M}_{\phi\phi} = -2q\bar{M}_{r\phi} + \bar{S}_{\phi\phi} - 2\beta\bar{M}_{\phi\phi} - \frac{2}{3}\epsilon_M, \quad (5.13)$$

$$\partial_t \bar{M}_{zz} = \bar{S}_{zz} - 2\beta\bar{M}_{zz} - \frac{2}{3}\epsilon_M, \quad (5.14)$$

where the relevant characteristic speed used to define dimensionless variables is the local sound speed².

In this model, the flow of turbulent energy from kinetic to magnetic field fluctuations is determined by the tensor given by

$$\bar{S}_{ij} = C_1^S \bar{R}_{ij} - C_2^S \bar{M}_{ij}, \quad (5.15)$$

where C_1^S and C_2^S are model constants. This tensor plays the most relevant role in connecting the dynamics of the different components of the Reynolds and Maxwell tensors. If \bar{S}_{ij} is positive, the interactions between the turbulent fluid motions and tangled magnetic fields enhances the latter.

²In order to simplify the comparison between the different models, we adopt the notation introduced in §5.2, even if this was not the original notation used by the corresponding authors. With the same motivation, we work with dimensionless sets of equations obtained by using the inverse of the local angular frequency (Ω_0^{-1}) as the unit of time and the relevant characteristic speeds or lengths involved in each case. We also provide the values of the various model constants that were adopted in order to obtain the total turbulent stresses as a function of the local shear shown in Figure 5.1.

The pressure-strain tensor is modeled in the framework of the two scale direct interaction approximation according to

$$\begin{aligned}\bar{\Pi}_{ij} = & -C_1^\Pi(\bar{R}_{ij} - \delta_{ij}\bar{R}/3) - C_2^\Pi(\bar{M}_{ij} - \delta_{ij}\bar{M}/3) \\ & -q C_0^\Pi \bar{R}(\delta_{ir}\delta_{j\phi} + \delta_{i\phi}\delta_{jr}),\end{aligned}\quad (5.16)$$

where \bar{R} and \bar{M} stand for the traces of the Reynolds and Maxwell stresses, respectively. This tensor accounts for the redistribution of turbulent kinetic energy along the different directions and tends to make the turbulence isotropic. The dissipation rates are estimated using mixing length arguments and are modeled according to

$$\epsilon_G = \frac{3}{2}\nu_G(\bar{R} + \bar{M}), \quad (5.17)$$

$$\epsilon_M = \frac{3}{2}\nu_M(\bar{R} + \bar{M}), \quad (5.18)$$

where ν_G and ν_M are dimensionless constants. The escape of magnetic energy in the vertical direction is taken into account phenomenologically via the terms proportional to the (dimensionless) rate

$$\beta = X\bar{M}^{1/2}, \quad (5.19)$$

where $0 < X < 1$ is a dimensionless parameter.

The values of the constants that we considered in order to obtain the curve shown in Figure 5.1 are the same as the ones considered in case 2 in Kato & Yoshizawa (1995), i.e., $C_0^\Pi = C_1^\Pi = C_2^\Pi = C_1^S = C_2^S = 0.3$, $\nu_G = \nu_M = 0.03$. We further consider $X = 0.5$ as a representative case.

In this model, the shear parameter q appears explicitly only in the terms that drive the algebraic growth of the turbulent stresses. The physical mechanism that allows the stresses to grow is the shearing of magnetic field lines. This can be seen

by ignoring all the terms that connect the dynamical evolution of the Reynolds and Maxwell stresses. When this is the case, the dynamics of these two quantities are decoupled. The Maxwell stress exhibits algebraic growth while the Reynolds stress oscillates if the flow is Rayleigh stable. The growth of the magnetic stresses is communicated to the different components of the Reynolds stress via the tensor $\bar{S}_{ij} \equiv C_1^S \bar{R}_{ij} - C_2^S \bar{M}_{ij}$.

A characteristic feature of this model is that the physical mechanism that leads to saturation is conceived as the escape of magnetic energy in the vertical direction. This process is incorporated phenomenologically by accounting for the leakage of magnetic energy with terms of the form $-\beta \bar{M}_{ij}$, where β stands for the escape rate. Although turbulent kinetic and magnetic dissipation act as sink terms in the equations for the various stress components (proportional to the model parameters ϵ_G and ϵ_M , respectively), if it were not for the terms accounting for magnetic energy escape, the system of equations would be linear. This means that, in order for a stable steady-state solution to exist, either the initial conditions or the constants defining the model will have to be fine-tuned.

The functional dependence of the total stress on the shear parameter q for the model proposed in Kato & Yoshizawa (1995) is shown in Figure 5.1. The model predicts vanishingly small stresses for small values of $|q|$; the total stress $\bar{T}_{r\phi}$ is a very strong function of the parameter q . Indeed, for $q > 0$, the model predicts $\bar{T}_{r\phi} \sim q^8$.

5.3.2 Ogilvie 2003

Based on a set of fundamental principles constraining the non-linear dynamics of turbulent flows, Ogilvie (2003) developed a model for the dynamical evolution of the Maxwell and Reynolds stresses. Five non-linear terms accounting for key physical processes in turbulent media are modeled by considering the form of the

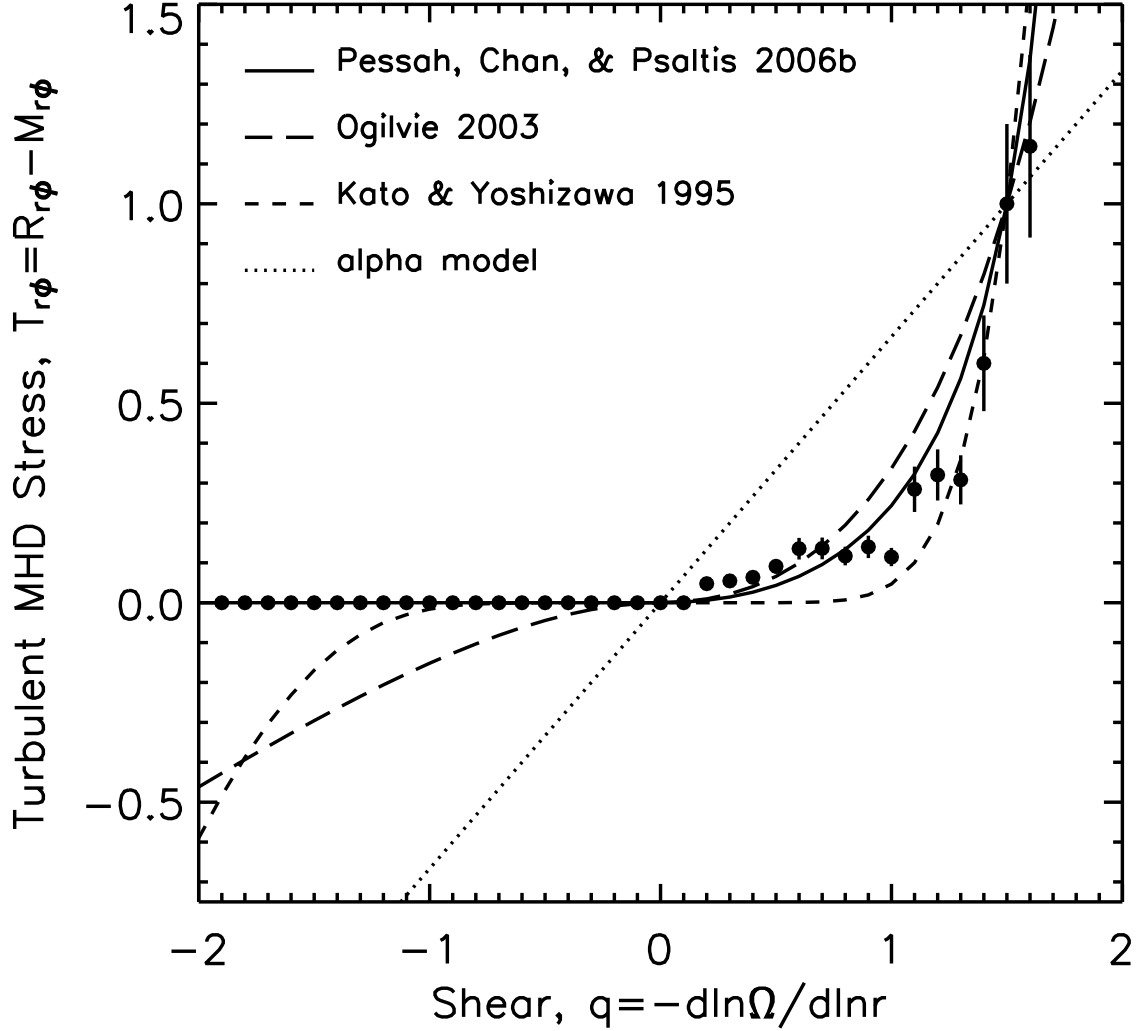


Figure 5.1 Total turbulent stress at saturation as a function of the shear parameter $q \equiv -d\ln\Omega/d\ln r$. The various lines show the predictions corresponding to the three models for turbulent MHD angular momentum transport discussed in §5.3. The filled circles correspond to the volume and time averaged MHD stresses calculated from the series of shearing box simulations described in §5.4. Vertical bars show the typical rms spread (roughly 20%) in the stresses as calculated from ten numerical simulations for a Keplerian disk. The dotted line corresponds to a linear relationship between the stresses and the local shear, like the one assumed in the standard model for alpha viscosity. All the quantities in the figure are normalized to unity for a Keplerian profile, i.e., for $q = 3/2$.

corresponding triple-order correlations, energy conservation, and other relevant symmetries.

Ogilvie suggested that the functional form of the equations governing the local, non-linear dynamics of a turbulent MHD flow are strongly constrained by a set of fundamental principles. The model that he developed is given by the following set of equations

$$\begin{aligned}\partial_t \bar{R}_{rr} &= 4\bar{R}_{r\phi} - c_1 \bar{R}^{1/2} \bar{R}_{rr} - c_2 \bar{R}^{1/2} (\bar{R}_{rr} - \bar{R}/3) \\ &\quad + c_3 \bar{M}^{1/2} \bar{M}_{rr} - c_4 \bar{R}^{-1/2} \bar{M} \bar{R}_{rr},\end{aligned}\tag{5.20}$$

$$\begin{aligned}\partial_t \bar{R}_{r\phi} &= (q-2) \bar{R}_{rr} + 2\bar{R}_{\phi\phi} - (c_1 + c_2) \bar{R}^{1/2} \bar{R}_{r\phi} \\ &\quad + c_3 \bar{M}^{1/2} \bar{M}_{r\phi} - c_4 \bar{R}^{-1/2} \bar{M} \bar{R}_{r\phi},\end{aligned}\tag{5.21}$$

$$\begin{aligned}\partial_t \bar{R}_{\phi\phi} &= 2(q-2) \bar{R}_{r\phi} - c_1 \bar{R}^{1/2} \bar{R}_{\phi\phi} - c_2 \bar{R}^{1/2} (\bar{R}_{\phi\phi} - \bar{R}/3) \\ &\quad + c_3 \bar{M}^{1/2} \bar{M}_{\phi\phi} - c_4 \bar{R}^{-1/2} \bar{M} \bar{R}_{\phi\phi},\end{aligned}\tag{5.22}$$

$$\begin{aligned}\partial_t \bar{R}_{zz} &= -c_1 \bar{R}^{1/2} \bar{R}_{zz} - c_2 \bar{R}^{1/2} (\bar{R}_{zz} - \bar{R}/3) \\ &\quad + c_3 \bar{M}^{1/2} \bar{M}_{zz} - c_4 \bar{R}^{-1/2} \bar{M} \bar{R}_{zz},\end{aligned}\tag{5.23}$$

$$\partial_t \bar{M}_{rr} = c_4 \bar{R}^{-1/2} \bar{M} \bar{R}_{rr} - (c_3 + c_5) \bar{M}^{1/2} \bar{M}_{rr},\tag{5.24}$$

$$\partial_t \bar{M}_{r\phi} = -q \bar{M}_{rr} + c_4 \bar{R}^{-1/2} \bar{M} \bar{R}_{r\phi} - (c_3 + c_5) \bar{M}^{1/2} \bar{M}_{r\phi},\tag{5.25}$$

$$\partial_t \bar{M}_{\phi\phi} = -2q \bar{M}_{r\phi} + c_4 \bar{R}^{-1/2} \bar{M} \bar{R}_{\phi\phi} - (c_3 + c_5) \bar{M}^{1/2} \bar{M}_{\phi\phi},\tag{5.26}$$

$$\partial_t \bar{M}_{zz} = c_4 \bar{R}^{-1/2} \bar{M} \bar{R}_{zz} - (c_3 + c_5) \bar{M}^{1/2} \bar{M}_{zz}.\tag{5.27}$$

Here \bar{R} and \bar{M} denote the traces of the Reynolds and Maxwell tensors and we have defined the quantities c_1, \dots, c_5 which are related to the positive dimensionless constants defined by Ogilvie C_1, \dots, C_5 via $C_i = Lc_i$, where L is a vertical characteristic length (e.g., the thickness of the disk). Note that Ogilvie's original equations are written in terms of Oort's first constant $A = q/2$.

The constant c_2 dictates the return to isotropy expected to be exhibited by freely decaying hydrodynamic turbulence. The terms proportional to c_3 and c_4 transfer energy between kinetic and magnetic turbulent fields. The constants c_1 and c_5 are related to the dissipation of turbulent kinetic and magnetic energy, respectively. Note that, in order to obtain the representative behavior of the total turbulent stress as a function of the local shear that is shown Figure 1, we have set $c_1, \dots, c_5 = 1$.

The resulting model describes the development of turbulence in hydrodynamic as well as in magnetized non-rotating flows. An interesting feature is that, depending on the values of some of the model constants, it can develop steady hydrodynamic turbulence in rotating shearing flows. For differentially rotating magnetized flows with no mean magnetic fields, the physical mechanism that allows the stresses to grow algebraically is the shearing of magnetic field lines, as in the case of Kato & Yoshizawa (1995).

The transfer of energy between turbulent kinetic and magnetic field fluctuations is mediated by the tensor $c_3 \bar{M}^{1/2} \bar{M}_{ij} - c_4 \bar{R}^{-1/2} \bar{M} \bar{R}_{ij}$, where \bar{R} and \bar{M} are the traces of the Reynolds and Maxwell stresses, respectively, and c_3 and c_4 are model constants. Note that, in this case, the terms that lead to communication between the different Reynolds and Maxwell stress components are intrinsically non-linear. The terms leading to saturation are associated with the turbulent dissipation of kinetic and magnetic energy and are given by $-c_1 \bar{R}^{1/2} \bar{R}_{ij}$ and $-c_5 \bar{M}^{1/2} \bar{M}_{ij}$, respectively.

The dependence of the total stress on the shear parameter for the model described in Ogilvie (2003) is shown in Figure 5.1. For angular velocity profiles satisfying $0 < q < 2$, the stress behaves as $\bar{T}_{r\phi} \sim q^n$ with n between roughly 2 and 3. Although the functional dependence of the total stress on negative values of

the shear parameter q is different from the one predicted by the model described in Kato & Yoshizawa (1995), this model also generates MHD turbulence characterized by negative stresses for angular velocity profiles increasing outwards.

5.3.3 Pessah, Chan, & Psaltis 2006

Motivated by the similarities exhibited by the linear regime of the MRI and the fully developed turbulent state (Pessah, Chan, & Psaltis, 2006a), we have recently developed a local model for the growth and saturation of the Reynolds and Maxwell stresses in turbulent flows driven by the magnetorotational instability (Pessah, Chan, & Psaltis, 2006b).

Using the fact that the modes with vertical wave-vectors dominate the fast growth driven by the MRI, we obtained a set of equations to describe the exponential growth of the different stress components. By proposing a simple phenomenological model for the triple-order correlations that lead to the saturated turbulent state, we showed that the steady-state limit of the model describes successfully the correlations among stresses found in numerical simulations of shearing boxes (Hawley, Gammie, & Balbus, 1995).

In this model, the Reynolds and Maxwell stresses are not only coupled by the same linear terms that drive the turbulent state in the previous two models but there is also a new tensorial quantity that couples their dynamics further. This new tensor cannot be written in terms of \bar{R}_{ij} or \bar{M}_{ij} , making it necessary to incorporate additional dynamical equations.

The set of equations defining the model is

$$\partial_t \bar{R}_{rr} = 4\bar{R}_{r\phi} + 2\bar{W}_{r\phi} - \sqrt{\frac{\bar{M}}{\bar{M}_0}} \bar{R}_{rr}, \quad (5.28)$$

$$\partial_t \bar{R}_{r\phi} = (q-2)\bar{R}_{rr} + 2\bar{R}_{\phi\phi} - \bar{W}_{rr} + \bar{W}_{\phi\phi} - \sqrt{\frac{\bar{M}}{\bar{M}_0}} \bar{R}_{r\phi}, \quad (5.29)$$

$$\partial_t \bar{R}_{\phi\phi} = 2(q-2)\bar{R}_{r\phi} - 2\bar{W}_{\phi r} - \sqrt{\frac{\bar{M}}{\bar{M}_0}} \bar{R}_{\phi\phi}, \quad (5.30)$$

$$\partial_t \bar{W}_{rr} = q\bar{W}_{r\phi} + 2\bar{W}_{\phi r} + \zeta^2 k_{\max}^2 (\bar{R}_{r\phi} - \bar{M}_{r\phi}) - \sqrt{\frac{\bar{M}}{\bar{M}_0}} \bar{W}_{rr}, \quad (5.31)$$

$$\partial_t \bar{W}_{r\phi} = 2\bar{W}_{\phi\phi} - \zeta^2 k_{\max}^2 (\bar{R}_{rr} - \bar{M}_{rr}) - \sqrt{\frac{\bar{M}}{\bar{M}_0}} \bar{W}_{r\phi}, \quad (5.32)$$

$$\begin{aligned} \partial_t \bar{W}_{\phi r} &= (q-2)\bar{W}_{rr} + q\bar{W}_{\phi\phi} \\ &+ \zeta^2 k_{\max}^2 (\bar{R}_{\phi\phi} - \bar{M}_{\phi\phi}) - \sqrt{\frac{\bar{M}}{\bar{M}_0}} \bar{W}_{\phi r}, \end{aligned} \quad (5.33)$$

$$\partial_t \bar{W}_{\phi\phi} = (q-2)\bar{W}_{r\phi} - \zeta^2 k_{\max}^2 (\bar{R}_{r\phi} - \bar{M}_{r\phi}) - \sqrt{\frac{\bar{M}}{\bar{M}_0}} \bar{W}_{\phi\phi}, \quad (5.34)$$

$$\partial_t \bar{M}_{rr} = -2\bar{W}_{r\phi} - \sqrt{\frac{\bar{M}}{\bar{M}_0}} \bar{M}_{rr}, \quad (5.35)$$

$$\partial_t \bar{M}_{r\phi} = -q\bar{M}_{rr} + \bar{W}_{rr} - \bar{W}_{\phi\phi} - \sqrt{\frac{\bar{M}}{\bar{M}_0}} \bar{M}_{r\phi}, \quad (5.36)$$

$$\partial_t \bar{M}_{\phi\phi} = -2q\bar{M}_{r\phi} + 2\bar{W}_{\phi r} - \sqrt{\frac{\bar{M}}{\bar{M}_0}} \bar{M}_{\phi\phi}, \quad (5.37)$$

where we have defined dimensionless variables using the mean Alfvén speed $\bar{v}_{Az} = \bar{B}_z / \sqrt{4\pi\rho_0}$, with \bar{B}_z the local mean magnetic field in the vertical direction and ρ_0 the local disk density. We have also introduced the tensor $\bar{W}_{ik} = \langle \delta v_i \delta j_k \rangle$, defined in terms of correlated fluctuations in the velocity and current ($\delta \mathbf{j} = \nabla \times \delta \mathbf{B}$) fields. The (dimensionless) wavenumber defined as

$$k_{\max}^2 = q - \frac{q^2}{4} \quad (5.38)$$

corresponds to the scale at which the MRI-driven fluctuations exhibit their maximum growth and

$$\bar{M}_0 \equiv \xi \rho_0 H \Omega_0 \bar{v}_{Az} , \quad (5.39)$$

is a characteristic energy density set by the local disk properties, with H the disk thickness. The parameters $\zeta \simeq 0.3$ and $\xi \simeq 11$ are model constants which are determined by requiring that the Reynolds and Maxwell stresses satisfy the correlations observed in numerical simulations of Keplerian shearing boxes with $q = 3/2$ (Hawley, Gammie, & Balbus, 1995).

In our model, a new set of correlations couple the dynamical evolution of the Reynolds and Maxwell stresses and play a key role in developing and sustaining the magnetorotational turbulence. In contrast to the two previous models, the tensor connecting the dynamics of the Reynolds and Maxwell stresses cannot be written in terms of \bar{R}_{ij} or \bar{M}_{ij} . This makes it necessary to incorporate additional dynamical equations for these new correlations. In agreement with numerical simulations, all the second-order correlations exhibit exponential (as opposed to algebraic) growth for shear parameters $0 < q < 2$. Incidentally, this is the only model in which the shear parameter, q , plays an explicit role in connecting the dynamics of the Reynolds and Maxwell stresses. The terms that lead to non-linear saturation are proportional to $-(\bar{M}/\bar{M}_0)^{1/2}$, where \bar{M} is the trace of the Maxwell stress and \bar{M}_0 is a characteristic energy density set by the local disk properties.

The functional dependence of the total turbulent stress on the shear parameter q for the model developed in Pessah, Chan, & Psaltis (2006b) is shown in Figure 5.1. For angular velocity profiles decreasing outwards, i.e., for $q > 0$, the stress behaves like $\bar{T}_{r\phi} \sim q^n$ with n between roughly 3 and 4. For angular velocity profiles increasing outwards, i.e., for $q < 0$, the stress vanishes identically. Note that this is the only model that is characterized by the absence of transport for all

negative values of the shear parameter q .

Figure 5.1 illustrates the sharp contrast between the functional dependence of the saturated stresses predicted by the MHD models with respect to the standard shear viscous stress defined in equation (5.5). In order to compare the predictions from each model independently of other factors, we normalized all the stresses to unity for a Keplerian shearing profile³. It is remarkable that, despite the fact that the various models differ on their detailed structure, all of them predict a much steeper functional dependence of the stresses on the local shear. Indeed, for angular velocity profiles decreasing outwards, they all imply $\bar{T}_{r\phi} \sim q^n$ with $n \gtrsim 2$. The predictions of the various models differ more significantly for angular velocity profiles increasing outwards. In this case, the models developed in Kato & Yoshizawa (1995) and Ogilvie (2003) lead to negative stresses, while the model developed in Pessah, Chan, & Psaltis (2006b) predicts vanishing stresses.

5.4 Results from Numerical Simulations

There have been only few numerical studies to assess the properties of magnetorotational turbulence for different values of the local shear. Abramowicz, Brandenburg, & Lasota (1996) carried out a series of numerical simulations employing the shearing box approximation to investigate the dependence of turbulent magnetorotational stresses on the shear-to-vorticity ratio. Although the number of angular velocity profiles that they considered was limited, their results suggest that the relationship between the turbulent MHD stresses and the shear is not

³Note that the model described in Pessah, Chan, & Psaltis (2006b) was developed to account for the correlations among stresses and magnetic energy density at saturation when there is a weak mean magnetic field perpendicular to the disk mid-plane. It is known that, for a given initial magnetic energy density, numerical simulations of MHD turbulent Keplerian shearing flows tend to saturate at higher magnetic energy densities when there is a net vertical magnetic flux (Hawley, Gammie, & Balbus, 1996). The normalization chosen in Fig. 5.1 allows to compare the shear-dependence of the various models regardless of their initial field configurations.

linear. Furthermore, Hawley, Balbus, & Winters (1999) carried out a series of shearing box simulations varying the shear parameter from $q = 0.1$ up to $q = 1.9$ in steps of $\Delta q = 0.1$ and reported on the dependence of the Reynolds and Maxwell stresses on the magnitude of the local shear but not on the corresponding dependence of the total stress.

In order to investigate the dependence of MRI-driven turbulent stresses on the sign and magnitude of the local shear, we performed a series of numerical simulations in the shearing box approximation for shear profiles in the range $-1.9 \leq q \leq 1.9$. We used a modified version of the publicly available ZEUS code, which is an explicit finite difference algorithm on a staggered mesh. A detailed description of the ZEUS code can be found in Stone & Norman (1992a,b) and Stone, Mihalas, & Norman (1992).

5.4.1 The Shearing Box Approximation

The shearing box approximation has proven to be fruitful in studying the local characteristics of magnetorotational turbulence from both the theoretical and numerical points of view. The local nature of the MRI allows us to concentrate on scales much smaller than the scale height of the accretion disk, H , and regard the background flow as essentially homogeneous in the vertical direction.

In order to obtain to the equations describing the dynamics of a compressible MHD fluid in the shearing box limit, we consider a small box centered at the radius r_0 and orbiting the central object in corotation with the disk at the local speed $\mathbf{v}_0 = r_0 \Omega_0 \check{\phi}$. The shearing box approximation consists of a first order expansion in $r - r_0$ of all the quantities characterizing the flow. The goal of this expansion is to retain the most important terms governing the dynamics of the MHD fluid in a locally Cartesian coordinate system (see, e.g., Goodman & Xu, 1994; Hawley, Gammie, & Balbus, 1995). This is a good approximation as long as the magnetic

fields involved are subthermal (Pessah & Psaltis, 2005). The resulting set of equations is then given by

$$\frac{\partial \rho}{\partial t} + \nabla \cdot (\rho \mathbf{v}) = 0 \quad (5.40)$$

$$\begin{aligned} \frac{\partial \mathbf{v}}{\partial t} + (\mathbf{v} \cdot \nabla) \mathbf{v} = & -\frac{1}{\rho} \nabla \left(P + \frac{\mathbf{B}^2}{8\pi} \right) + \frac{(\mathbf{B} \cdot \nabla) \mathbf{B}}{4\pi\rho} \\ & - 2\Omega_0 \times \mathbf{v} + q\Omega_0^2 \nabla (r - r_0)^2 \end{aligned} \quad (5.41)$$

$$\frac{\partial \mathbf{B}}{\partial t} = \nabla \times (\mathbf{v} \times \mathbf{B}) \quad (5.42)$$

$$\frac{\partial E}{\partial t} + \nabla \cdot (E \mathbf{v}) = -P \nabla \cdot \mathbf{v} \quad (5.43)$$

where ρ is the density, \mathbf{v} is the velocity, \mathbf{B} is the magnetic field, P is the gas pressure, and E is the internal energy density. In writing this set of equations, we have neglected the vertical component of gravity and defined the local Cartesian differential operator,

$$\nabla \equiv \check{\mathbf{r}} \frac{\partial}{\partial r} + \check{\boldsymbol{\phi}} \frac{\partial}{\partial \phi} + \check{\mathbf{z}} \frac{\partial}{\partial z}, \quad (5.44)$$

where $\check{\mathbf{r}}$, $\check{\boldsymbol{\phi}}$, and $\check{\mathbf{z}}$ are, coordinate-independent, orthonormal basis vectors corotating with the background flow at r_0 . Note that the third and fourth terms on the right hand side of equation (5.41) account for the Coriolis force that is present in the rotating frame and the radial component of the tidal field, respectively. We close the set of equations (5.40)–(5.43) by assuming an ideal gas law with $P = (\gamma - 1) E$, where γ is the ratio of specific heats.

5.4.2 Numerical Set Up

In order to explore a wide range of local shearing profiles, we modified a version of ZEUS-3D to allow for angular velocity profiles that increase with increasing radius and are thus characterized by shear parameters $q < 0$.

We set the radial, azimuthal, and vertical dimensions of the simulation domain to $L_r = 1$, $L_\phi = 6$, and $L_z = 1$. In order to ensure that the numerical

diffusion is the same in all directions, we set the resolution of the simulations to $32 \times 192 \times 32$. We assume an adiabatic equation of state with $\gamma = 5/3$ and set the initial density to $\rho = 1$. The initial velocity field corresponds to the steady state solution $\mathbf{v} = -q\Omega_0(r - r_0)\check{\phi}$ and we choose the value $\Omega_0 = 10^{-3}$ in order to set the time scale in the shearing box. Note that for $q = 3/2$, this velocity field is simply the first order expansion of a steady Keplerian disk around r_0 . We consider the case of zero net magnetic flux through the vertical boundaries by defining the initial magnetic field according to $\mathbf{B} = B_0 \sin[2\pi(r - r_0)/L_r]\check{\mathbf{z}}$. The plasma β in all the simulations that we perform is $\beta = P/(B_0^2/8\pi) = 200$, so the magnetic field is highly subthermal in the initial state.

Keeping all the aforementioned settings unchanged, we perform a series of numerical simulations with different values of the shear parameter q , from $q = -1.9$ up to $q = 1.9$ in steps of $\Delta q = 0.1$. In order to excite the MRI, we introduce random perturbations at the 0.1% level in every grid point over the background internal energy and velocity field. For each value of the shear parameter q , we run the simulation for 100 orbits. We then compute a statistically meaningful value for the saturated stress $\bar{T}_{r\phi}$ by averaging the last 50 orbits in each simulation (Winters, Balbus, & Hawley, 2003; Sano, Inutsuka, Turner, & Stone, 2004).

5.4.3 Results

The results from thirty nine numerical simulations performed with different values of the shear parameter $-1.9 \leq q \leq 1.9$ are shown in Figure 5.1 as filled circles. The vertical bars show the typical spread (roughly 20%) in the total saturated turbulent stress as calculated from ten numerical simulations with a Keplerian profile, i.e., for $q = 3/2$. We have taken this as a representative value for the typical rms spread in runs with different values of the parameter q .

It is evident from Figure 5.1 that the turbulent magnetorotational stresses are

not proportional to the local shear. There is indeed a strong contrast with respect to the standard assumption of a linear relationship between the stresses and the local shear (dotted line in the same figure) for both positive and negative shear profiles. For angular velocity profiles that decrease with increasing radius, i.e., for $q > 0$, all of the turbulent states are characterized by positive mean stresses and thus by outward transport of angular momentum. In these cases, stronger shear results in larger saturated stresses but the functional dependence of the total stress is not linear. For angular velocity profiles that increase with increasing radius, i.e., for $q < 0$, all the numerical simulations reach the same final state regardless of the magnitude of the parameter q . The stresses resulting from the initial seed perturbations (at the 0.1% level) quickly decay to zero. This is in sharp contrast with the large negative stresses that are implied by the standard Newtonian model for the shear viscous stress in equations (5.5) and (5.6).

In order to explore further the decay of MHD turbulence found for angular velocity profiles increasing outwards, we also performed the following numerical experiment. We seeded a run with a shear parameter $q = -3/2$ with perturbations at the 100% level of the background internal energy and velocity field. In this case, the timescale for the decay of the initial turbulent state was longer than the one observed in the corresponding run seeded with perturbations at the 0.1% level. The final outcome was nonetheless the same. After a few orbits, the stresses decayed to zero and remained vanishingly small until the end of the run at 100 orbits. This result highlights the strong stabilizing effects of a positive angular velocity gradient on the dynamical evolution of the turbulent stresses due to tangled magnetic fields. This behavior can be understood in terms of the joint restoring action due to magnetic tension and Coriolis forces acting on fluid elements displaced from their initial orbits.

5.5 Discussion

In this chapter, we investigated the dependence of the turbulent stresses responsible for angular momentum transport in differentially rotating magnetized media on the local shear parameterized by $q = -d \ln \Omega / d \ln r$. The motivation behind this effort lies in understanding whether one of the fundamental assumptions on which much of the standard accretion disk theory rests, i.e., the existence of a linear relationship between these two quantities, holds when the MHD turbulent state is driven by the MRI. We addressed this problem both in the context of current theoretical turbulent stress models as well as using the publicly available three-dimensional numerical code ZEUS.

From the theoretical point of view, we have seen that, despite their different structures, all of the available high-order closure schemes (Kato & Yoshizawa, 1993, 1995; Ogilvie, 2003; Pessah, Chan, & Psaltis, 2006b) predict stresses whose functional dependence on the local shear differ significantly from the standard alpha model. In order to settle this result on firmer grounds, we performed a series of numerical simulations of MRI-driven turbulence in the shearing box approximation for different values of the local shear characterizing the background flow. The main conclusion to be drawn from our study is that turbulent MHD stresses in differentially rotating flows are not linearly proportional to the local background disk shear. This finding challenges the central assumption in the standard accretion disk model, i.e., that the total stress acting on a fluid element in a turbulent magnetized disk can be modeled as a (Newtonian) viscous shear stress.

We find that there is a strong contrast between the stresses produced by MHD turbulence and the viscous shear stresses regardless of whether the disk angular velocity decreases or increases outwards. In the former case, i.e., for $q > 0$ as in

a Keplerian disk, the total turbulent stress generated by tangled magnetic fields is not linearly proportional to the local shear, q , as it is assumed in standard accretion disk theory. On the other hand, for angular velocity profiles increasing outwards, i.e., for $q < 0$ as in the boundary layer close to a slowly rotating accreting stellar object, MHD turbulence driven by the MRI fails to transport angular momentum, while viscous shear stresses lead to enhanced negative stresses.

If magnetorotational turbulence is the main mechanism enabling angular momentum transport in accretion disks then the dependence of the stress on the local shear discussed here has important implications for the global structure and long term evolution of accretion disk around protostars, proto-neutron stars, accreting binaries, and active galactic nuclei.

CHAPTER 6

SUMMARY AND OUTLOOK:

TOWARDS MAGNETOROTATIONAL ACCRETION DISK MODELS

It has long been thought that turbulence provides a natural avenue towards efficient angular momentum transport in accretion disks (Shakura & Sunyaev, 1973). However, for many years, the relevance of magnetic fields as the driving mechanism of the required turbulence remained only a speculation. More than 15 years after Balbus and Hawley realized the relevance of the MRI in the context of astrophysical disks, this powerful instability stands as the most promising mechanism for driving and sustaining the turbulent state in sufficiently ionized disks. Nevertheless, there are currently no accretion disk models that incorporate the MRI in a self-consistent way as the driving mechanism enabling turbulent angular momentum transport. In this dissertation I presented a series of steps towards this end.

6.1 Summary

As a first step towards understanding the stability properties of more realistic accretion flows, I investigated the local linear stability of differentially rotating, magnetized flows and the evolution of the MRI beyond the weak-field limit. I showed that, when superthermal toroidal fields are considered, the effects of both compressibility and magnetic tension forces, which are related to the curvature of toroidal background field lines, should be taken fully into account. The more general framework that I considered allowed me to reconcile seemingly discordant results derived in previous works. I demonstrated that the presence of a strong toroidal magnetic field component plays a non-trivial role not only by modifying

the growth rates of the unstable modes but also by determining which modes are subject to instabilities. For rotating configurations with Keplerian laws, I found that the MRI is stabilized at low wavenumbers for toroidal Alfvén speeds exceeding the geometric mean of the sound speed and the rotational speed. For a broad range of magnetic field strengths, I also found that two additional distinct instabilities are present. I discussed the significance of these findings for the stability of cold, magnetically dominated, rotating fluids and the implications of these results for the validity of the standard shearing box approximation when strong toroidal fields are considered.

It has been suspected for some time that, on top of being able to disrupt the laminar disk flow, the MRI might play a continuous role by influencing the characteristics of the turbulent stresses observed during the saturated state reached by numerical simulations (Winters, Balbus, & Hawley, 2003). In chapter 3, I presented the first formal analytical proof showing that, during the exponential growth of the instability, the mean Reynolds stress is always positive, the mean Maxwell stress is always negative, and hence the mean total stress is positive and leads to a net outward flux of angular momentum. More importantly, I showed that the ratio of the Maxwell to the Reynolds stresses during the late times of the exponential growth of the instability is determined only by the local shear and does not depend on the initial spectrum of perturbations or the strength of the seed magnetic field. Even though I derived these properties of the stress tensors during the exponential growth of the instability in incompressible flows, numerical simulations of shearing boxes show that this characteristic is qualitatively preserved under more general conditions, even during the saturated turbulent state generated by the instability.

The observation that the MHD turbulence in local numerical simulations seems

to be strongly influenced by the MRI itself motivated the development of a local model for angular momentum transport where the turbulent stresses are continuously driven by the instability. In chapter 4, I derived equations that describe the effects of the instability on the growth and pumping of the stresses and then supplemented these equations with a phenomenological description of the triple correlations that lead to saturation. I showed that the steady-state limit of the proposed model describes successfully the correlations among stresses found in numerical simulations of shearing boxes. Furthermore, I highlighted the relevance of a new type of correlation that couples the dynamical evolution of the Reynolds and Maxwell stresses and plays a key role in developing and sustaining the magnetorotational turbulence. Preliminary results suggest that these correlations are dynamically important not only during the initial phase of the instability, but more importantly during the fully developed turbulent state.

Real accretion disks are unlikely to have Keplerian angular velocity profiles at all radii and at all times. Therefore, it is important to understand how the physical characteristics of angular momentum transport are modified when the disk rotational profile is different from Keplerian. In the α -model, the stress responsible for angular momentum transport is linearly proportional to the local disk shear. In chapter 5, I noted that there is no a priori reason to assume that the correlated fluctuations defining the total turbulent stress in MRI-driven turbulence behaves in this way.

I addressed in detail how the transport of angular momentum mediated by MHD turbulence driven by the MRI depends on the magnitude of the local shear. I found that there is a strong contrast between the stresses produced by MHD turbulence and viscous shear stresses regardless of whether the local disk angular velocity decreases or increases outwards. In the former case, which includes Ke-

plerian disks, the total turbulent stress generated by tangled magnetic fields is not linearly proportional to the local shear, as it is assumed in standard accretion disk theory. On the other hand, for angular velocity profiles increasing outwards, like the one expected in a boundary layer close to an accreting star, MHD turbulence driven by the MRI fails to transport angular momentum, while viscous shear stresses lead to enhanced negative stresses. These results suggest that one of the fundamental assumptions in which the standard model for viscous angular momentum transport is based is not appropriate for describing turbulent MRI-driven accretion disks.

6.2 Beyond the Standard Accretion Disk Model

The work presented in this dissertation constitutes the first in a series of steps towards establishing the formalism and methodology needed to move beyond the standard accretion disk model. The next step consist of building the framework to couple the *local* model for angular momentum transport driven by the MRI (chapters 4 and 5) with the equations that describe the *global* disk dynamics (chapter 1).

In order to obtain the global structure of a turbulent magnetized accretion disk, it is necessary to solve the coupled set of equations describing mass conservation, radial momentum conservation, and angular momentum conservation, together with a suitable energy equation. In order for the model to be self-consistent, however, it will be necessary to consider the simultaneous evolution of the turbulent stresses by incorporating the set of equations that describes their dynamics (Pessah, Chan, & Psaltis, 2006b).

A global disk model built in this way will thus constitute a fundamental improvement over the standard α -disk in five crucial respects:

- (i) The stresses will no longer be postulated but will be calculated self-consistently as the result of the joint action of magnetic fields and differential rotation.
- (ii) By construction, in the local limit, the stresses will not be proportional to the local shear (as in the α -disk) but instead will agree with the results from local numerical simulations.
- (iii) Because the model will allow for the different flow variables, including the stresses, to be carried in (advected) with finite propagation speed as matter moves inwards, the stresses will no longer be locally determined but will be affected by the recent history of the flow, in agreement with global numerical simulations (Armitage, 1998; Hawley, 2000, 2001).
- (iv) In the α -disk, defined by parabolic (diffusive) equations, the stresses at the inner disk must be provided as a boundary condition. This value has been a matter of heated debate for several decades. The properties of this new model, defined by hyperbolic (causal) equations, will allow us to calculate the stresses at the inner disk as a function of the global disk properties.
- (v) Finally, in the α -disk, information can propagate across sonic points (where the radial inflow speed of matter equals the local value of the sound speed). This is an unphysical property of viscous α -disks that can only be eliminated by invoking ad hoc prescriptions. The set of equations that I will solve is hyperbolic and, therefore, the disk model that it describes will not suffer from this causality problem.

6.3 A New Era in Accretion Disk Modeling

By contrasting the predictions of this self-consistent model with observations, it will be possible to deepen our fundamental understanding of the formation, evolution, and physical properties of stars and black holes in a way that is unattainable within the framework of the α -disk. I am particularly interested in four outstanding astrophysical problems in which I expect the global structure of an MRI-driven accretion disk to depart significantly from the current standard model.

Origin of millisecond pulsars — Accretion disks have long been thought to be responsible for the spin up of old neutron stars. Recent *Chandra* observations of the extraordinary population of millisecond pulsars in 47 Tuc have provided strong support for their binary origin (Bogdanov, Grindlay, & van den Berg, 2005). Current direct numerical simulations for studying the interaction between a turbulent magnetized accretion disk and a weakly magnetized neutron star can only be evolved for nearly 50 orbits (Steinacker & Papaloizou, 2002). I will use the accretion disk model that I will develop to study the long-term effects of accretion-induced spin up. Initially, the accreting neutron star in the binary must be rotating significantly slower than the Keplerian period at its surface. Thus, in the region known as the boundary layer, the angular velocity profile of the disk must present a maximum and decrease toward smaller radii. Under this condition, standard α -disks are subject to strong negative stresses, while I have shown that MRI turbulence cannot be driven in situ. Therefore, the exerted torques at the inner disk must be determined by the stresses advected from larger radii. The resulting direction and magnitude of angular momentum transfer between the disk and the slowly spinning neutron star will determine how long it takes to significantly spin it up and its limiting spin frequency. By performing a numerical study along the lines of Popham & Narayan (1991), I will then investigate the

long-term effects of the interaction between a turbulent MRI-driven disk and a slowly spinning, weakly magnetized, accreting neutron star. I will determine the conditions, and the implied timescales, that lead to significant neutron star spin up and, possibly, spin-orbit alignment.

Emission spectra of turbulent black hole accretion disks — The wealth of spectroscopic observations obtained with *ASCA*, *BeppoSAX*, *RXTE*, *XMM-Newton*, and *Chandra* has open up the possibility of constraining the spin of galactic black holes via accretion disk spectral modeling (Shafee et al., 2006; Davis, Done, & Blaes, 2006). There are currently a few available models with different degrees of sophistication. In all of them, the emitted spectrum is calculated by adding the contributions from the different disk annuli to obtain the total emitted disk radiation. Even though the various models predict different emerging spectra from a given disk annulus, at present, all of them adopt the standard α -prescription to determine the global structure of the disk. This, in turn, determines the overall shape of the emergent spectrum (e.g., the nature of the color correction is sensitive to the model-dependent disk surface density profile). I will calculate the spectral energy distribution emitted by self-consistent disk models for which angular momentum transport is mediated by turbulent MRI-driven stresses. I will investigate how the emission spectrum of a turbulent magnetized disk depends on the mass, spin, and accretion rate of the central black hole. By comparing the predictions of these models with observations, I will set constraints on the values of these quantities. This study will also provide an explicit way to check the sensitivity of the derived black hole properties to the nature of the mechanisms enabling angular momentum transfer, especially in the inner, potentially non-Keplerian, regions of the accretion flows.

Origin of broad-band black hole variability — It is believed that the X-ray variability observed from black holes of all masses with *RXTE*, *XMM-Newton*, and *Chandra* is produced by global oscillations of the inner accretion disks (Nowak & Wagoner, 1991; Kato, 2001). To date, however, only a few attempts have been made to understand the effects that the magnetic fields (that allegedly allow the accretion process) have on these oscillations and none of them have taken into account the fact that accretion disks are highly turbulent. In order to understand the different ways in which turbulent disks can oscillate, I will perform the first diskoseismic analysis of a geometrically-thin turbulent magnetized disk. By understanding how the mass and the spin of the black hole determine the frequency and amplitude of the oscillations trapped in the deep potential well of a pseudo-relativistic gravitational field, I will seek to constrain these quantities with observations. This study will also provide a solid theoretical basis for the phenomenological work that I have done on mass estimation of supermassive black holes using X-ray binaries (Pessah, 2007; Pessah & Psaltis, 2007). On the other hand, disk instabilities are currently the most promising mechanism accounting for the optical/UV variability observed in AGN (Kawaguchi, Mineshige, Umemura, & Turner, 1998; Hawkins, 2002). The variability properties predicted by these models depend on the various timescales governing the dynamics of the disk. With this in mind, I will construct disk instability models that will incorporate the various timescales relevant to turbulent magnetized disks. I will then investigate the nature of the observed correlations in the broad-band (from the optical to X-rays) variability of accreting black holes. I will also address the role of turbulent transport in variable disk phenomena at lower energies. I will then compare the predictions of these models with the results obtained from AGN light curves in order to infer some of the physical properties of their accretion flows.

Black hole spin and torques at the inner edge — The energetic photons produced in the inner disk regions carry vital information on the physical conditions under which they were emitted. The exquisite spectroscopic information obtained with *Chandra* and *XMM-Newton*, has opened up the possibility of constraining the physical properties of compact objects via the study of the fluorescent broadened Fe K α line (Agol & Krolik, 2000; Wilms, Reynolds, & Begelman, 2001; Reynolds et al., 2004). One fundamental assumption made when modeling the profile of this line is that the stresses vanish at the radius of the innermost stable circular orbit (which depends on the mass and spin of the black hole). However, this assumption has been challenged by recent numerical simulations (Gammie, 1999; Krolik, 1999; Hawley & Krolik, 2001; Krolik & Hawley, 2002; Reynolds & Armitage, 2001). The accretion disk model that I will construct will incorporate the advection of turbulent stresses throughout successive disk radii, leading naturally to non-vanishing stresses inside the marginally stable orbit. I will investigate how these stresses determine the structure of the inner disk and, thus, the profile of the iron line. This will allow me to assess how the standard assumption affects the derivation of reliable physical parameters of accreting black holes. I will also seek to shed light onto the discrepancies in black hole spins obtained from spectral fitting and iron-line modeling (Miller, 2006). I expect that the semi-analytical nature of this treatment will facilitate systematic studies of the degeneracies that affect the profile of the iron line. These types of studies are crucial for understanding the feasibility of unambiguously constraining black hole properties with observations. With a more realistic inner disk model, I will study the conditions for efficient accretion disk-black hole spin-jet alignment that seems to be supported by theoretical work (Volonteri, 2005; Natarajan & Pringle, 1998) and observations of radio-loud early-type galaxies (van Dokkum & Franx, 1995).

APPENDIX A

MRI MODES WITH FINITE k_r/k_z RATIOS

The central dispersion relation derived in chapter 2 , i.e., equation (2.25), was derived considering axisymmetric perturbations in both the vertical and the radial directions. Throughout the majority of our analysis, however, we focused our attention on the modes with vanishingly small ratios k_r/k_z . Particular emphasis has been given to the study of these modes in the literature of weakly magnetized, differentially rotating disks, since these are the modes that exhibit the fastest growth rates (Balbus & Hawley, 1992, 1998; Balbus, 2003). After having analyzed the role played by magnetic tension forces due to the finite curvature of strong toroidal field lines on the stability of these modes, we are in a better position to understand their effects on the modes for which the ratio k_r/k_z is finite.

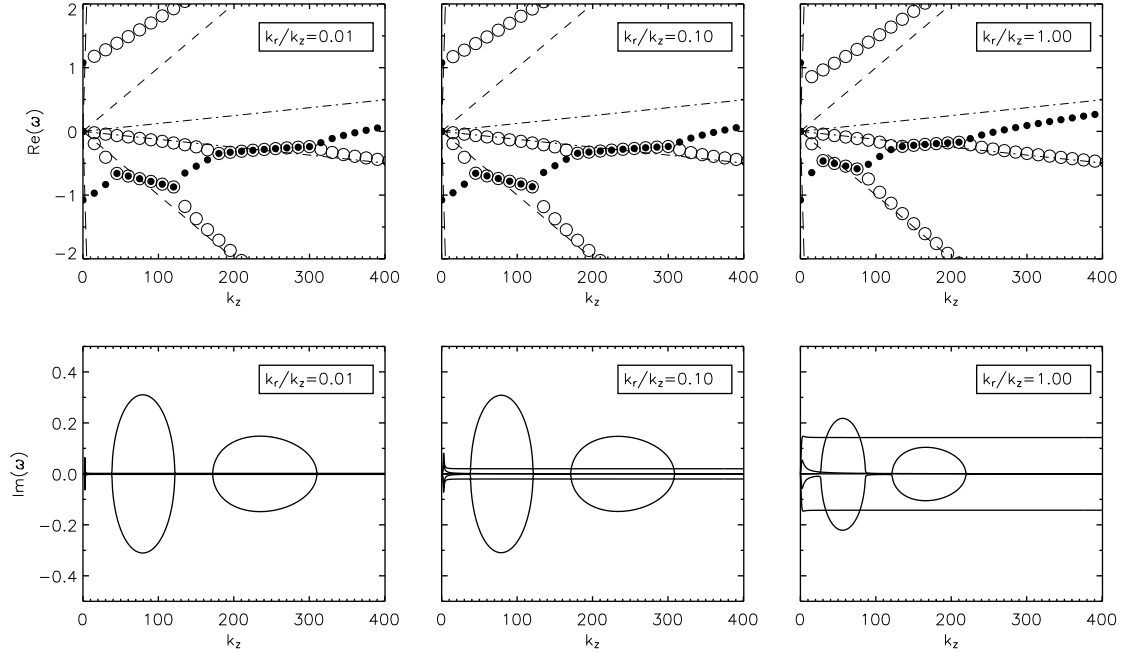
In Figure A.1, we present the solutions to the dispersion relation (2.25) for three different ratios of the radial to the vertical wavenumber, i.e., $k_r/k_z = 0.01$, 0.1, and 1. For the sake of comparison, we have used in this figure the same parameters that we used in obtaining the left panels in Figure 2.4, for which the ratio k_r/k_z was considered to be vanishingly small; we have assumed $c_s = 0.05$, $v_{Az} = 0.01$, $v_{A\phi} = 0.4$ and a Keplerian disk. In all the cases, the same instabilities (II and III) that were present in the case $k_z \gg k_r$ can be clearly identified. Note however, that even for very small ratios k_r/k_z (e.g., left panels in Figure A.1) some of the modes that were stable in the case $k_z \gg k_r$ become unstable, albeit with negligible growth rate, when compared with the other unstable modes. It is also evident that in the limit $k_z \gg k_r$, the mode structure in Figure A.1 tends continuously toward the mode structure in the left panels in Figure 2.4. It is this continuous behavior that ultimately justifies the study of modes with negligible

ratio k_r/k_z in a local stability analysis.

In the case $k_r = k_z$ (right panels in Figure A.1), the value of the critical vertical wavenumbers for the onset of instabilities, i.e., k_z^{c1} and k_z^{c2} in equations (2.52) and (2.53) respectively, are different with respect to the case in which $k_z \gg k_r$ by a factor $\sqrt{2}$. This indicates that k_z and k_r play similar roles in establishing these critical wavenumbers. The growth rates of all these modes are reduced with respect to the case with $k_z \gg k_r$. This behavior is similar to the one observed in the case of weak magnetic fields. It is important to stress that, even for the modes with comparable values of vertical and radial wavenumbers, the general characteristics of the instabilities for strong toroidal fields that we discussed in §2.4.1 are insensitive to the inclusion of a non-negligible k_r .

The completely new feature in Figure A.1 is the appearance of another instability with a growth rate that does not seem to depend on wavenumber; the terms proportional to ik_r in equation (2.25) are crucial for the appearance of this new instability. The mode that is unstable seems to correspond to the mode that becomes the Alfvén mode in the limit of no rotation. With increasing values of the ratio k_r/k_z , the growth rates of the instabilities studied in §2.4.1 go to zero, but the new instability in Figure A.1 persists. Note that for $k_r \simeq k_z$ the growth rates of all the instabilities in Figure A.1 are comparable.

As an aside, we point out that all the terms that are proportional to ik_r , as opposed to k_r^2 , in equation (2.25) are also proportional to some factor ϵ_i with $i = 1, 2, 3, 4$. All of these terms are negligible for sufficiently small ratios k_r/k_z no matter how strong the toroidal field is. Indeed, if we consider perturbations with small enough radial wavelengths, at some point, curvature effects will not be important. However, this is not true in the vertical direction. In that case, we can ignore the curvature terms only when the toroidal field is weak.



APPENDIX B

MRI MODES WITH VANISHING FREQUENCY

In chapter 2, we have seen that the toroidal component of the magnetic field does play a role in determining the stability criteria. In fact, for superthermal fields and quasi toroidal configurations, it dictates the values of some of the critical wavenumbers for the onset of instabilities (see §2.4.2). A particular, simple case, in which the importance of considering both compressibility and magnetic tension terms can be appreciated, is the study of modes with negligible frequency, i.e., with $\omega \ll 1$. We can obtain the wavenumber of these modes by imposing $\omega = 0$ to be a solution of the dispersion relation (2.25). We obtain, in physical dimensions,

$$(k_z^0)^2 = -2 \frac{d \ln \Omega}{d \ln r} \bigg|_0 \left(\frac{\Omega_0 r_0}{v_{Az}} \right)^2 + 2\epsilon_1 \epsilon_3 \left(\frac{v_{A\phi}}{v_{Az}} \right)^2 + \epsilon_2 \epsilon_3 \left(\frac{v_{A\phi}}{v_{Az}} \right)^2 \left(\frac{v_{A\phi}}{c_s} \right)^2. \quad (\text{B.1})$$

In what follows, let us consider a rotationally supported disk whose rotational profile is not too steep (i.e., $|d \ln \Omega / d \ln r|$ is of order unity). The Alfvén speed v_{Az} appears in all three terms on the right hand side of equation (B.1) and therefore it does not play a role in determining the relative magnitudes between them. Unlike the second term, the third term is not necessarily small with respect to the first one, when superthermal fields are considered. In this case, it seems again (see §2.4.2) safe to neglect the curvature term proportional to $\epsilon_1 \delta v_{A\phi}$ in equation (2.17). However, had we neglected the curvature term proportional to $\epsilon_2 \delta \rho$ in equation (2.17) or the one proportional to $\epsilon_3 \delta v_{Ar}$ in equation (2.18), we would have missed the important impact that the third term in equation (B.1) has on the stability of modes with $\omega \rightarrow 0$, in the limit of strong toroidal fields (see Fig. 2.3). This is somewhat counterintuitive because there does not seem to be any *a priori*

indication about which of the magnetic tension terms (related to the curvature of the toroidal field component) is less relevant in the original set of equations (2.16)-(2.22) for the perturbations. This particular example illustrates the risks associated with neglecting terms that are not strictly 2nd order in the perturbed quantities but rather address the geometrical characteristics of the background in which the (local) analysis is being carried out.

From equation (B.1) it is also straightforward to see under which circumstances it is safe to neglect the curvature terms. For subthermal fields, k_z^0 will not differ significantly from k_{BH} (eq. [2.32]) regardless of the geometry of the field configuration. This is because, if the field is weak enough ($v_A \ll c_s$), no matter how strong of a (subthermal) B_ϕ component we consider, the second and third term are negligible with respect to the first one. We conclude this short analysis by commenting that, while a strong vertical field plays a stabilizing role, in the sense that it drives k_z^0 toward small values leaving all modes with shorter wavelengths stable, the consequences of considering strong toroidal fields is a little more subtle as can be seen in the evolution of the structure of the modes in Figure 2.1.

REFERENCES

- Abramowicz, M., Brandenburg, A., & Lasota, J. P., 1996, MNRAS, 281, L21
- Afshordi, N., Mukhopadhyay, B., & Narayan, R., 2005, ApJ, 629, 373
- Agol, E. & Krolik, J. H., 2000, ApJ, 528, 161
- Armitage, P. J., 1998, ApJ, 501, L189
- Balbus, S. A., 2003, ARA & A, 41, 555
- Balbus, S. A. & Hawley, J. F., 1991, ApJ, 376, 214
- Balbus, S. A. & Hawley, J. F., 1992, ApJ, 392, 662
- Balbus, S. A., Hawley, J. F., & Stone, J. M., 1996, ApJ, 467, 76
- Balbus, S. A. & Hawley, J. F., 1997, ASPC, 121, 90
- Balbus, S. A. & Hawley, J. F., 1998, Rev. Mod. Phys., 70, 1
- Balbus, S. A. & Hawley, J. F., 2002, ApJ, 573, 749
- Balbus, S. A. & Hawley, J. F., 2006, ApJ, 652, 1020
- Balbus, S. A. & Papaloizou, J. C. B., 1999, ApJ, 521, 650
- Bhattacharya, D. & van den Heuvel, E. P. J., 1991, PhR, 203, 1
- Blackman, E. G., 2001, MNRAS, 323, 497
- Blackman, E. G. & Field, G. B., 2002, Phys. Rev. Lett., 89, 265007
- Blaes, O. M. & Balbus, S. A., 1994, ApJ, 421, 163

- Blaes, O. M. & Socrates, A., 2001, *ApJ*, 553, 987
- Blaes, O., 2004, in *Accretion Disks, Jets, and High Energy Phenomena in Astrophysics*, Les Houches Lect. Notes 78, 137-185
- Bourke, T. L., & Goodman, A. A., 2003, In *Star Formation at High Angular Resolution*, ASP Conf. Ser., Vol. S-221, eds. M. G. Burton, R. Jayawardhana, and T. L. Bourke (astro-ph/0401281)
- Bogdanov, S., Grindlay, J.E., & van den Berg, M., 2005, *ApJ*, 630, 1029
- Brandenburg, A., 1998, in *Theory of Black Hole Accretion Discs*, Abramowicz M. A., Björnsson G., Pringle J. E., eds., Cambridge University Press, Cambridge
- Brandenburg, A., 2001, *ApJ*, 550, 824
- Brandenburg, A., 2005, *Astron. Nachr.*, 326, 787
- Brandenburg, A. & Subramanian, K., 2005, *Phys. Rep.*, 417, 1
- Brandenburg, A., Nordlund A., Stein R. F., & Torkelsson, U., 1995, *ApJ*, 446, 741
- Brandenburg, A., & Campbell, C., *Accretion Disks - New Aspects*, Proceedings of the EARA Workshop Held in Garching, Germany, 21-23 October 1996, XIII. Springer-Verlag, Berlin
- Bonnell, I. A., Clarke, C. J., Bate, M. R., & Pringle, J. E., 2001, *MNRAS*, 324, 573
- Chandrasekhar, S., 1960, *Proc. Natl. Acad. Sci. U.S.A.* 46, 253
- Chen, K., Halpern, J. P., & Filippenko, A. V., 1989, *ApJ*, 339, 742
- Curry, C. & Pudritz, R. E., 1995, *ApJ*, 453, 697
- Davis, S. W., Done, C., & Blaes, O. M., 2006, *ApJ*, 647, 525

- Dubrulle, B. & Knobloch, E., 1993, *A&A*, 274, 667
- Eracleous, M. & Halpern, J. P., 1994, *ApJS*, 90, 1
- Fleming, T. & Stone, J. M., 2003, *ApJ*, 585, 908
- Frank, J., King, A., & Raine, D.J., 2002, *Accretion Power in Astrophysics*, 3rd edn. Cambridge University Press, Cambridge
- Ford, H. C., Harms, R. J., Tsvetanov, Z. I., et al., 1994, *ApJ*, 435, L27
- Gammie, C. F. & Balbus, S. A., 1994, *MNRAS*, 270, 138
- Gammie, C. F., 1998, in *Accretion Processes in Astrophysical Systems: Some Like it Hot!*, S. S., Holt, T. R. Kallman, AIPC 431, 99
- Gammie, C. F., 1999, *ApJ*, 522, L57
- Gardiner, T. & Stone, J. M., 2005, in *Magnetic Fields in the Universe*, AIP Conf. Proc., 784, 475
- Goodman, J. & Xu, G., 1994, *ApJ*, 432, 213
- Hawkins, M., 2002, *A&A*, 329, 76
- Hawley, J. F., 2000, *ApJ*, 528, 462
- Hawley, J. F., 2001, *ApJ*, 554, 534
- Hawley, J. F., Balbus S. A., & Winters W. F., 1999, *ApJ*, 518, 394
- Hawley, J. F., Gammie, C. F., & Balbus, S. A., 1994, in *ASP Conf. Ser. 54, The First Stromlo Symposium: The Physics of Active Galaxies*. ed. G. V. Bicknell, M. A. Dopita, & P.J. Quinn (San Francisco:ASP), 53

- Hawley, J. F., Gammie, C. F., & Balbus, S. A., 1995, *ApJ*, 440, 742
- Hawley, J. F., Gammie, C. F., & Balbus, S. A., 1996, *ApJ*, 464, 690
- Hawley, J. F. & Krolik J. H., 2001, *ApJ*, 548, 348
- Hoffman, K. M. & Kunze, R., 1971, *Linear Algebra*, 2nd ed. Prentice Hall, N.J.
- Horne, K., 1985, *MNRAS*, 213, 129
- Jaffe, W., Ford, H. C., Ferrarese, L., van den Bosch, F., & O'Connell, R. W., 1993, *Nature*, 364, 213
- Ji, H., Burin, M., Scharfman, E., & Goodman, J., 2006, *Nature*, 444, 343
- Kato, S. 2001, *PASJ*, 53, 1
- Kato, S., Fukue J., & Mineshige S., 1998, *Black-Hole Accretion Disks*. Kyoto University Press, Kyoto
- Kato, S. & Yoshizawa, A., 1993, *Publ. Astron. Soc. Jap.*, 45, 103
- Kato, S. & Yoshizawa, A., 1995, *Publ. Astron. Soc. Jap.*, 47, 629
- Kawaguchi, T., Mineshige, S., Umemura, M., & Turner, E., 1998, *ApJ*, 504, 671
- Kim, W. T. & Ostriker, E. C., 2000, *ApJ*, 540, 372
- Knobloch, E., 1992, *MNRAS*, 255, 25
- Krause, F. & Rädler, K. H., 1980, *Mean-Field Magnetohydrodynamics and Dynamo Theory*, Pergamon Press, Oxford
- Krolik, J. H., 1999, *ApJ*, 515, L73
- Krolik, J. H. & Hawley, J. F., 2002, *ApJ*, 573, 754

- Kudoh, T., Matsumoto, R., & Shibata, K., 2002, PASJ, 54, 121
- Landau, L.D. & Lifshitz, E. M., 1959, Fluid Mechanics. Pergamon Press. Oxford
- Lynden-Bell, D. & Pringle, J. E., 1974, MNRAS, 168, 603
- MacFadyen, A. I., Woosley, S. E., & Heger, A., 2001, ApJ, 550, 410
- Machida, M., Hayashi, M. R., & Matsumoto, R., 2000, ApJ, 532, L67
- Marsh, T. R. & Horne, K., 1988, MNRAS, 224, 269
- Mauche, C. W., 2002, ApJ, 580, 423
- Miller, K. A., & Stone, J. M., 2000, ApJ, 534, 398
- Miller, J. M., 2006, Variable and Broad Iron Lines Around Black Holes, eds. A. C. Fabian & N. Schartel, Madrid, Spain
- Miyoshi, M., Moran, J., Herrnstein, J., Greenhill, L., Nakai, N., Diamond, P., & Inoue, M., 1995, Nature, 373, 127
- Mukhopadhyay, B., Afshordi, N., & Narayan, R., 2005, ApJ, 629, 383
- Myers, P. C. & Goodman, A. A., 1988, ApJ, 326, L27
- Nakao, Y., 1997, Publ. Astron. Soc. Jap., 49, 659
- Narayan, R., Quataert, E., Igumenshchev, I. V., & Abramowicz, M. A., 2002, ApJ, 577, 295
- Natarajan, P. & Pringle, J. E., 1998, ApJ, 506, L97
- Nowak, M. A. & Wagoner, R. V., 1991, ApJ, 378, 656
- Ogilvie, G. I., 2003, MNRAS, 340, 969

- Ostriker, E. C., Stone, J. M., & Gammie, C. F., 2001, *ApJ*, 577, 524
- Padmanabhan, T., 2001, *Theoretical astrophysics. Volume II: Stars and stellar systems*. Cambridge University Press, Cambridge
- Papaloizou, J. E. & Szuszkiewicz, E., 1992, *Geophys. Astrophys. Fluid Dyn.*, 66, 223
- Pariev, V. I., Blackman, E. G., & Boldyrev, S. A., 2003, *A&A*, 407, 403
- Pessah, M. E. & Psaltis, D., 2005, *ApJ*, 628, 879
- Pessah, M. E., Chan, C. K., & Psaltis D., 2006a, *MNRAS*, 372, 183P
- Pessah, M. E., Chan, C. K., & Psaltis, D., 2006b, *Phys. Rev. Lett.*, 97, 221103
- Pessah, M. E., Chan, C. K., & Psaltis, D., 2007, *MNRAS*, submitted [astroph/0612404]
- Pessah, M. E., 2007, *ApJ*, 655, 66
- Pessah, M. E. & Psaltis, D., 2007, *ApJ*, in preparation
- Popham, R. & Narayan, R., 1991, *ApJ*, 370, 604
- Press, W. H., Flannery, B. P., Teukolsky, S. A., & Vetterling, W. T., 1992, *Numerical Recipes*, Cambridge University Press, Cambridge
- Pringle, J. E., 1989, *MNRAS*, 236, 107
- Quataert, E., Dorland, W., & Hammett, G. W., 2002, *ApJ*, 577, 524
- Rees, M. J., 1984, *ARA&A*, 22, 471
- Reynolds, C. S. & Armitage, P. J., 2001, *ApJ*, 561, L81

- Reynolds, C. S., Brenneman, L. W., Wilms, J., & Kaiser, M. E., 2004, *MNRAS*, 352, 205
- Ryu, D. & Goodman, J., 1992, *ApJ*, 388, 438
- Sano, T., Inutsuka, S., Turner, N. J., & Stone J. M., 2004, *ApJ*, 605, 321
- Sano, T. & Miyama, S. M., 1999, *ApJ*, 515, 776
- Shafee, R., McClintock, J. E., Narayan, R., Davis, S. W., Li, L. X., & Remillard, R. A., 2006, *ApJ*, 636, L113
- Shakura, N. I. & Sunyaev, R. A., 1973, *A&A*, 24, 337
- Shilov, G.E. & Silverman, R.A., 1973, *Mathematical Analysis*. MIT Press, Cambridge
- Steinacker, A. & Papaloizou, J. C. B., 2002, *ApJ*, 571, 413
- Stone, J. M. & Norman, M. L., 1992a, *ApJS*, 80, 753
- Stone, J. M. & Norman, M. L., 1992b, *ApJS*, 80, 791
- Stone, J. M., Mihalas, D., & Norman, M. L., 1992, *ApJS*, 80, 819
- Stone, J. M. & Balbus, S. A., 1996, *ApJ*, 464, 364
- Stone, J. M. & Pringle, J. E., 2001, *MNRAS*, 322, 461
- Stone, J. M., Hawley J. F., Gammie, C. F., & Balbus, S. A., 1996, *ApJ*, 463, 656
- Tanaka, Y., Nandra, K., Fabian, A. C., et al., 1995, *Nature*, 375 ,659
- Thompson, T. A., Quataert, E., & Burrows, A., 2005, *ApJ*, 620, 861

- van der Klis, M., 2005, in *Compact stellar X-ray sources*, eds. W. H. G. Lewin, & M. van der Klis, Cambridge University Press, Cambridge
- van Dokkum, P. G. & Franx, M., 1995, *AJ*, 110, 2027
- Velikhov, V. P., 1959, *Sov. Phys. JETP* 36, 995
- Vishniac, E. T. & Brandenburg, A., 1997, *ApJ*, 475, 263
- Volonteri, M., Madau, P., Quataert, E., & Rees, M. J., 2005, *ApJ*, 620, 69
- Warner, B., 1995, *Cataclysmic Variables*, Cambridge University Press, Cambridge
- Wheeler, J. C., 1993, *Accretion Disks in Compact Stellar Systems*, World Scientific, Singapore
- Wilms, J., Reynolds, C. S., & Begelman, M. C., et al., 2001, *MNRAS*, 328, L27
- Winters, W. F., Balbus, S. A., & Hawley, J. F., 2003, *MNRAS*, 340, 519
- Yoshizawa, A., 1985, *Phys. Fluids*, 28, 3313
- Yoshizawa, A., Itoh, S. I., & Itoh, K., 2003, *Plasma and Fluid Turbulence: Theory and Modelling*. Institute of Physics, London